Study on Thin Film Growth of Organic Semiconductor Molecules with Enhanced Intermolecular Interaction

Chunyang Zhang

July 2019

Study on Thin Film Growth of Organic Semiconductor Molecules with Enhanced Intermolecular Interaction

Chunyang Zhang

Doctoral Program in Applied Physics

Submitted to the Graduate School of

Pure and Applied Sciences

In Partial Fulfillment of Requirements

for the Degree of Doctor of Philosophy in

Engineering

at the

University of Tsukuba

Abstract

It is generally known that the precise control of molecular packing, crystal structure, film morphology and the electronic structure of organic semiconductors (OSCs) is the pre-condition for obtaining excellent charge-transport properties in organic electronics. However, the methods of controlling the structure of organic thin films have not been well established, and the fabrication of highly ordered thin films remains a challenge. In this thesis, we expect that OSCs with enhanced intermolecular interaction, such as picene, DNTT and sumanene, are more applicable for the realization of high-quality and controllable thin films. Therefore, the purpose of this thesis is to examine the fabrication of high-quality thin films of these three promising molecules by utilizing their stronger intermolecular interaction at highly ordered interfaces on noble metal surface, which is expected to construct reliable models for high-performance organic electronics.

In the study on the fabrication of highly oriented multilayer films of picene and DNTT on their bulklilke monolayer, by means of slow deposition of the multilayer on the bulklike monolayer, large-scale crystalline islands having lengths of several hundred micrometers were obtained, especially in the case of picene. XRD measurement revealed that picene crystals consist of planes of $(20\bar{1})$ and $(21\bar{1})$, clearly suggesting that the film consists of the parallel molecules which may be stabilized by the peculiar structure of the monolayer.

From the study of morphology and electronic structure of peculiar sumanene monolayers and fabrication of sumanene thin films, the highly-ordered bowl-stacking arrangement of sumanene molecules was first realized on Cu(111) surface in this work. The two kinds of peculiar sumanene monolayers which shows bowl-stacking molecular arrangement on Cu(111) and bowl-up and bowl-down molecular arrangement on Ag(111) and Au(111), respectively, were characterized by UPS, XPS and ARPES. The superior electronic structure along the bowl-stacking direction of sumanene monolayer on Cu(111) was indicated. In addition, the superior growth of sumanene thin film with tilted molecular arrangement on Cu(111) was found, which may stabilized by the well-ordered monolayer with stronger intermolecular interaction along the bowl-stacking direction.

In addition, by comparing the thin film morphology and the calculated force constant of intermolecular van der Waals force of picene, DNTT and sumanene, extremely long islands of picene thin film and larger force constant of intermolecular van der Waals force of picene strongly indicate that the strong intermolecular interaction is beneficial for the fabrication of high quality organic thin films.

The manipulation of the film morphology by the regulation of intermolecular interaction at highly ordered interfaces on noble metal surface is expected to construct reliable models for high-performance organic electronics.

Contents

Chapter 1

Introduction

1.1 Research Background

1.1.1 Organic Electronics

Since the late 1990s and early 2000s, the research of organic semiconductors (OSCs), which has been extensively researched as nest-generation electronic devices, has gained enormous world-wide effort in related fields. The studies of OSCs has been dramatically improved the fabrication level of organic devices. Advantages of OSCs compared with typical inorganic semiconductors are low cost, light weight, simple preparation process, good environmental stability and large area flexible devices can be made, et.al.. The deposition of organic films on a wide variety of substrates has led to plastic solar cells, flexible displays and printable circuits[1,2]. The features that can be designed extremely small and lightweight and to meet the needs of human body, making the organic electronics become indispensable to the development of the field of electronic technology. However, the disadvantage of organic electronics is the relatively low charge transport ability than inorganic elections. Most of the OSCs have a carrier mobility, which is the most important figure of merit in field effect transistors of any kind, in the range of $10^{-6}\sim10^{-4}$ $cm^2V^{-1}s^{-13}$. To improve the application of OSCs, various OSCs has been studied to search for materials with higher carrier mobility. Such as the most popular OSCs, pentacene, was reported to be a good candidate for a p-type semiconductor that attracted great interest due to its high hole mobility. Pentacene-based organic devices with a mobility of approximately 1×1.0 $cm^2V^{-1}s^{-1}$, which is comparable to or exceeding those of amorphous silicon, was reported in 1992. What's more, the amorphous silicon with the carrier mobility of 0.5-1.0 $cm^2V^{-1}s^{-1}$, which is most used in thin-film devices nowadays, requires a very complicated process at high temperature (360°) under plasma influence. Therefore, one of the goals in the field of OSCs is to seek materials that can replace amorphous silicon. Therefore, most of the current researches are focused on how to improve the charge carrier transport ability of organic electronics, which can make organic electronics widely applied in the commercial field.

The charge transport mechanism of OSCs is as follows. Conjugated molecules of OSCs contain arrays of carbon p orbitals that overlap within the molecule to give rise to π orbitals. The filled π orbitals form the valence states, the empty π^* antibonding orbitals form the conduction states. The π orbitals are substantially delocalized over the molecule. In organic solids, the π bonding and antibonding orbitals overlap to form the valence and conduction bands respectively and defined by the highest occupied molecular orbital (HOMO) and the lowest unoccupied molecular orbital (LUMO). OSCs is well known to transport holes and electrons

via HOMO and LUMO of closely packed and highly conjugated aromatic molecules. However, the intermolecular interactions of OSCs are due to van der Waals force, which can be easily disrupted by disorder. Therefore, charge carrier transport of organic electronics depends on not only the electronic structure of the molecules, but also how the molecules are packed together, i.e. the thin film morphology.

1.1.2 Organic Thin Film Growth

In the field of organic electronics, it always optimizing the performance of devices by determining the structure-property relations between organic films and resulting electronic properties. In particular films composed of small organic molecules like acenes grow in a crystalline fashion. However, the charge transport ability of OSC thin films is generally worse than that of single crystal. According to recent reports, the molecular arrangement of thin films is influenced by the interaction between the molecules and the substrate[4], and the electronic structure of thin films is significantly different from that of a single crystal. In another word, the charge transport ability of OSCs is affected by the molecular arrangement. Therefore, the precisely control of the structure of thin film at an atomic level, and the understanding of structural and electronic properties are crucial to improve their charge transport ability.

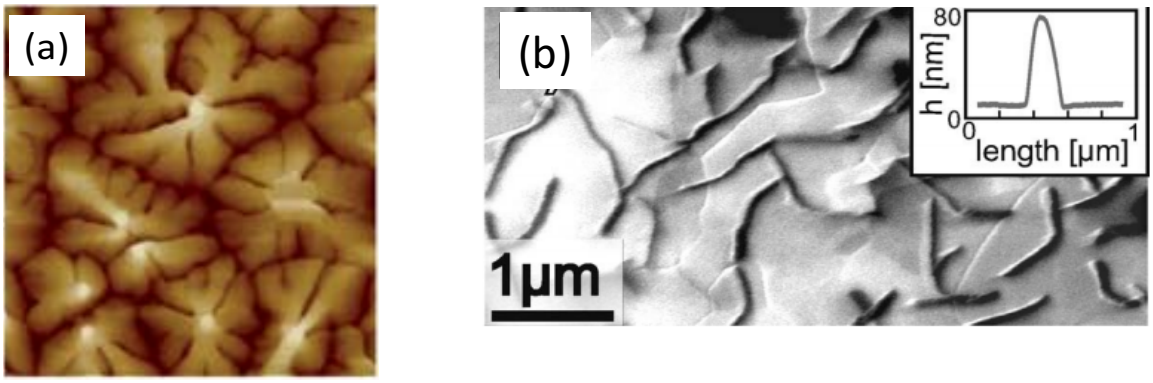

Figure 1.1 (a)[5]Dendritic growth of pentacene; (b)[6]Nano-fiber structure of pentecene thin film.

For the common growth feature of thin films of OSCs, the monolayer of these molecules on the flat substrates usually take a "flat-lying" or "face-on" conformation due to significant coupling between π orbital of molecules and the surface electronic states. Such as pentacene, the growth of thin film starts with monolayer with “face-on” adsorbed molecules. The flat initial layer serves as a wetting layer for additional growth upon further adsorption, which always shows the significant different molecular arrangement with the monolayer, i.e. the second layer does not usually follow the configuration of the monolayer and tend to "stand up". This mechanism usually leads to a dendritic growth of the multilayer with a complicated morphology and small domain sizes with lots of grain boundaries (as shown in Figure 1.1(a)), which can limit the charge transport ability of the thin film[6]. Besides, for their application in OFETs and OLEDs, some small organic molecules are also well known to form highly anisotropic crystal shapes which are always called nano-fibers or nano-needles as shown in Figure 1.1 (b)[6–9]. The well oriented chains of crystallites forming on a wetting layer are obey

Stranski-Krastanov growth modes. These films with big crystalline island with less grain boundaries are expected to be more promising to get high transport ability which can approach to the value of single crystal. However, only a limiting case of highly anisotropic needle-like nanofibers were generated. The formation of such kind of highly ordered thin film crucially depends on the molecular symmetry, organic crystal unit cell, molecular adsorption geometry, contact plane and molecular packing which are hardly controllable until now.

1.1.3 Organic Molecules with Enhanced Intermolecular Interaction

The application of prominent organic semiconductors, such as pentacene, for OFETs in 1992 is a great breakthrough for the application of OSCs, because it can realize a high field-effect mobility value of approximately 1 $cm^2V^{-1}s^{-1}$. The hole mobility of pentacene single crystal was reported up to 35 $cm^2V^{-1}s^{-1}$[10]. Unfortunately, pentacene is very unstable in the air condition (Figure 1.2), which can reduce the hole mobility and conductivity[11]. Because the overlap of HOMO of pentacene molecules is reduced by the substituted oxygen atoms. Therefore, alternative OSCs with high hole mobility and stability should be found. Since the electronic properties of OSCs also strongly depend on their molecular structure, the synthetic chemistry based on this kind of molecules has attracted continuous attentions, and diverse organic molecules with enhanced intermolecular interaction have been widely synthesized and evaluated as organic semiconductors for OFET applications. In this work, we focused on three organic molecules with enhanced intermolecular interaction, picene, DNTT and sumanene. The details of molecular structure of these three molecules are introduced as follows.

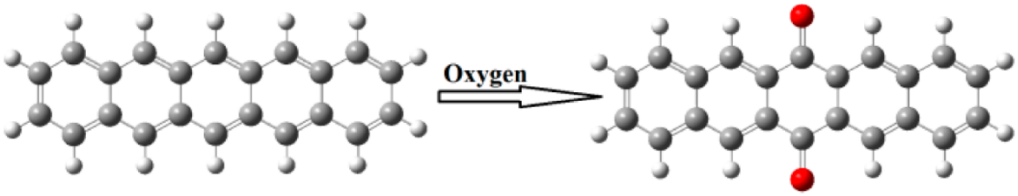

Figure 1.2 Diagram of oxygen substitution in pentacene molecule at air condition, which will dramatically reduce the hole mobility of pentacene.

- **Picene**

Picene, an isomer of pentacene with linear backbone framework, has been known as a stable compound in which the benzene rings are fused in a zigzag phenacene structure as shown in the Figure 1.3. Picene has been attracted great interest because of not only the good hole mobility, which shows the value at about 0.6 $cm^2V^{-1}s^{-1}$, but the high air stability. The higher stability[13], even against O_2 [13]and H_2O[14] of picene than pentacene has been reported. That is because the characteristics of the frontier orbitals significantly depend on the edge structure of aromatic hydrocarbons. In the acene-edge structure, the frontier orbitals are localized at the edges, because the vertical cross-link bonding between two zigzag edges caused out-of phase atomic-orbital combination that tend to disperse frontier spin-orbitals. Whereas in the phenancene-edge structure, the frontier orbitals are distributed evenly over the carbon structure, because the interaction between armchair

edges takes place through inner ca. 120° angle-oriented cross-linkage of in-phase character, resulting in spin-orbitals that bear close proximity or even accidental degeneracy[15,16]. The difference of their molecular structure cause the low HOMO level and large ionization potential energy of picene over pentacene. On the other hand, picene have recently reported to show superconductivity by incorporating alkali-metal atoms in to solids picene (Figure 1.3(b)). Therefore, picene is a kind of very promising OSCs for the application in organic electronics[17].

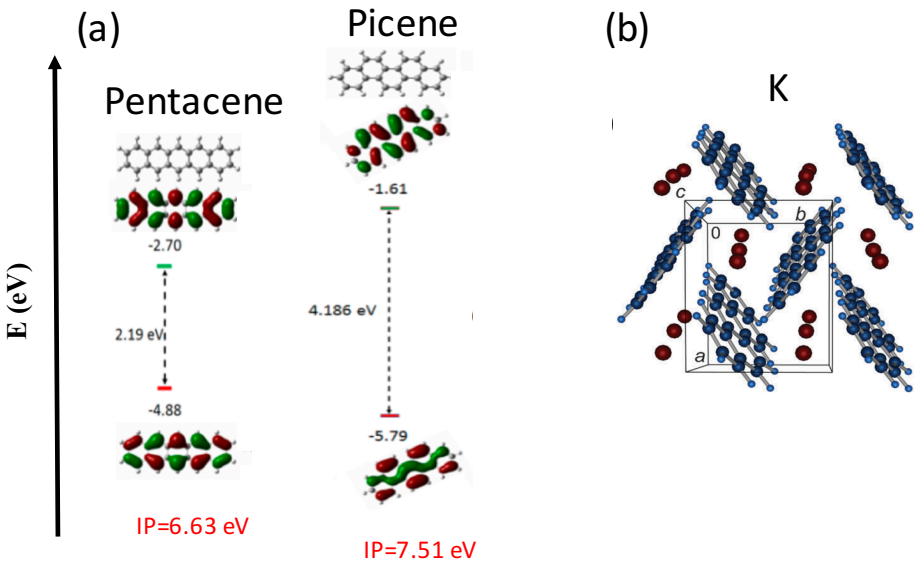

Figure 1.3 (a) Differecne of electronic structure between picene and pentacene molecules; (b) Diagram of alkali-metal doped picene, which shows the superconductivity at 18 K.

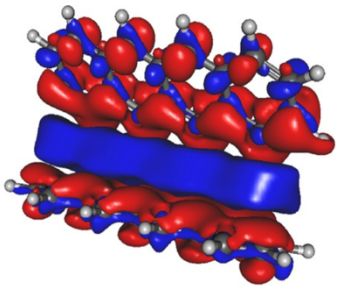

Figure 1.4 Diagram of CH-π interaction

The reported crystalline structures of picene and pentacene both show the typical herringbone structure within the ab plane. This kind of herringbone packing is a pervasive structural motive found in most molecular crystals involving aromatic compounds. The herringbone arrangement is characterized by tilted edge-to-face C-H$\cdots\pi$ interactions as shown in Figure 1.4. It has reported that the C-H$\cdots\pi$ bonding show the major contribution to the lattice energy in linear polycyclic aromatic hydrocarbons[18]. The hole mobility of picene and pentacene single crystals are calculated to be highest in the ab plane[19]. The highest charge transfer integral in the pentacene crystal is along the herringbone arrangement. The highest hole mobility is observed along $\pi-\pi$ stacking direction, i.e. the b* axis, for picene crystal, indicating a strong $\pi-\pi$ overlap as compared

with pentacene crystal. Therefore, it should be a good strategy to produce a high charge transport for picene crystal with the $\pi - \pi$ stacking structure where the overlap of two adjacent monomers would be enhanced. Thus, the precisely control of molecular packing of picene molecules in thin films is very important.

- **DNTT**

One molecular design strategy to improve its chemical stability is to replace the highly reactive central benzene ring with heterole rings of pentacene. DNTT is such a kind of air-stable OSCs, which can be regarded as the combination of acene and oligo/polythiophene. The structure of DNTT molecule is shown in Figure 1.5(a). Since electronegative substituents open up the possibilities of modifying the crystal packing of pentacene by replacing the edge-to-face C-H$\cdots\pi$ interactions with other intermolecular interactions that could enhance the overlap between molecular wave functions. Many substitution schemes have been investigated, such as heteroatom substitution. Oligo/polythiophenes was regarded as a key ingredient in the development of π-extended opto-electronic materials. Thienoacenes is a kind of molecules putting thiophene rings into the acene structures to result in ladder-type thiophene-containing π-conjugated molecules with high chemical stabilities. This new structure of the molecule causes the different geometry (distribution of electron density) of the HOMO as shown in Figure 1.5 (b). HOMOs of single molecules affect the ability of the intermolecular orbital overlap. It was shown that, the large electron densities on the sulfur atoms can serve as an effective overlap between the HOMOs of adjacent molecules in the solid state[20], causing a high air-stable hole mobility of 8.3 $cm^2V^{-1}s^{-1}$ of DNTT single crystal organic field effect transistor[21]. The highest hole mobility with a large transfer integral value in DNTT crystal shows also along the direction with herringbone-like intermolecular interaction[22,23].

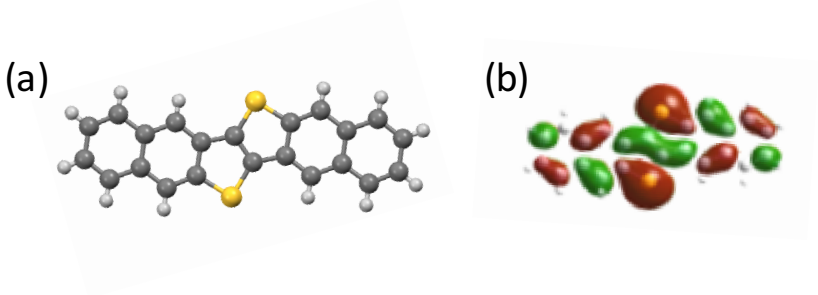

Figure 1.5 (a)Structure of DNTT molecule. (b) HOMO structure of DNTT.

- **Sumanene**

Sumanene is a bowl-shaped molecule, which can be regarded as a fragment of fullerene, consisting of three benzenes and three cyclopentadiene rings alternatively fused together forming a central six-membered ring (Figure 1.6(a))[24].It is well known as the buckybowl or π-bowl together with corannulene as the smallest non-planar organic molecules. The curvature of the bowl-shaped molecule resulting from π-conjugation causes two distinct faces. Thus, the orbital structure and electron density of these two faces are different, inducing a large dipole moment of 1.939 D of sumanene in perpendicular axis[25].

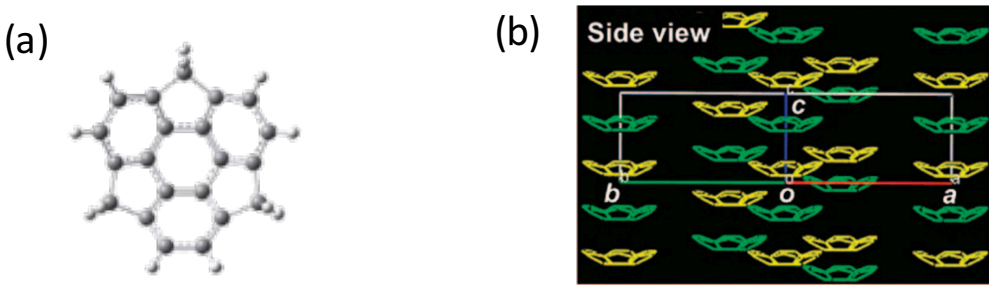

Figure 1.6(a) Sumanene molecule. (b) Side view of sumanene single crystal.

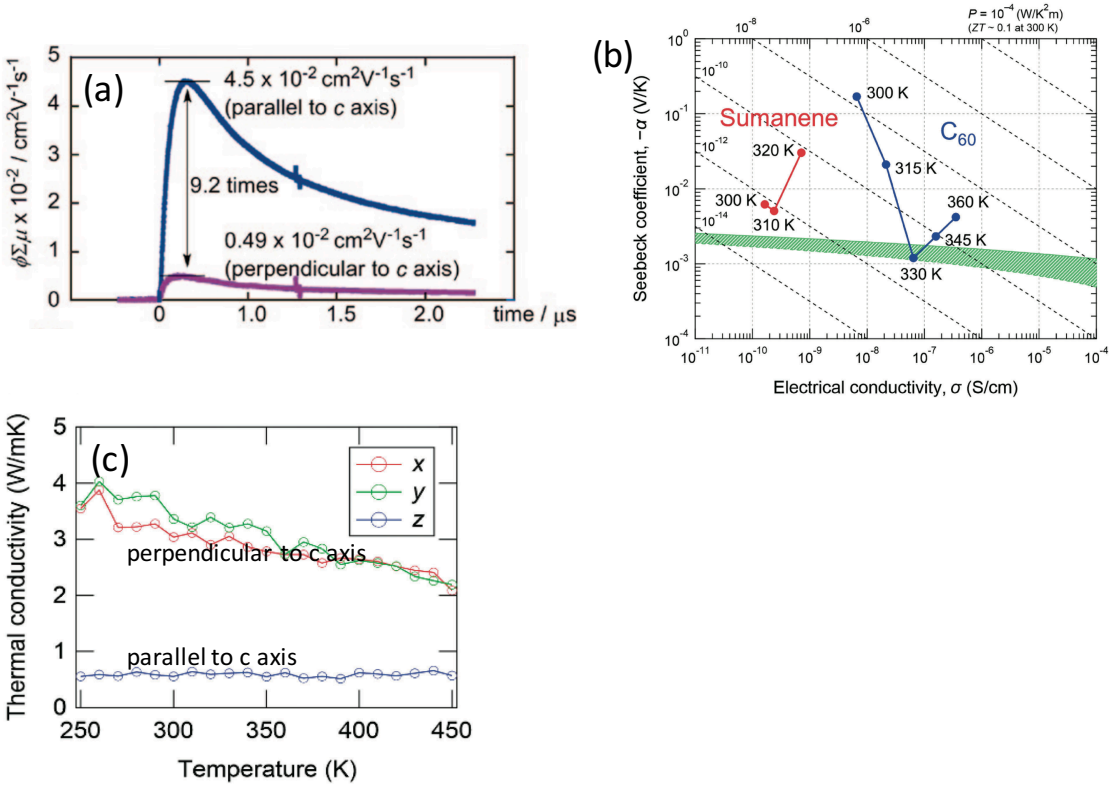

Figure 1.7 (a)High carrier mobility along bowl stacking direction in sumanene single crystal, which is 9.2 times larger than that along perpendicular direction. (b)Large Seebeck coefficient of sumanene. (c) Thermal conductivity in sumanene single crystal.

Unlike flat- π-conjugated compounds favors herringbone packing in a crystal, curved surfaces favor the bowl-bowl stacking compensate for the overlap. The most representative example is the crystal packing of sumanene with perpendicular ordered columnar packing, where each column faces the same direction[26](as shown in Figure 1.6(b)). The minimum estimate of the intra-columnar electron mobility of sumanene single crystal along the bowl-stacking direction was calculated to be 0.75 $cm^2V^{-1}s^{-1}$[27], which is comparable to a C_{60} single crystal (0.5 $cm^2V^{-1}s^{-1}$)[28]. A much smaller conductivity was exhibited along the perpendicular direction to the bowl-stacking axis in sumanene single crystal by TRMC (time-resolved microwave conductivity) method[27] (as shown in Figure 1.5(a)). Recently, sumanene have been reported to exhibit thermoelectric properties. According to the dimensionless figure of merit, $ZT=\alpha^2\sigma T/\kappa$ (α: Seebeck coefficient, σ:

electrical conductivity, κ: thermal conductivity, T: temperature). A large α and small κ alone bowl-stacking direction of sumanene, as shown in Figure 1.5(b) and (c). Side-by-side intermolecular interaction of sumanene in the single crystal is proved to exhibits an excellent thermal conduction than those in the bowl-stacking direction, which is in contrast to the electrical conduction[29]. Therefore, precisely control of molecular arrangement of sumanene molecules is important for the application in the field of organic electronics.

1.2 Purpose of The Present Studies

Since the crystalline morphology and molecular orientation of thin films have a great impact on their electronic properties, precisely controlled film structure is very important for the application in the field of organic electronics. As mentioned above, OSCs, such as picene, DNTT and sumanene, with enhanced intermolecular interactions, are expected to show superior electronic properties or thermal transport properties because of their special molecular structure, making them a promising candidate for industrial use. Therefore, the highly ordered thin film characterization with a molecular level control for these kinds of OSCs is very important for the development and production of devices. Therefore, the purpose of this work is to examine the fabrication of high-quality thin film of OSCs with enhanced intermolecular interactions. Based on this motivation, we utilized picene, DNTT and sumanene to illustrate the growth procedure from their initial monolayer to multilayer film at an atomic level. The highly defined systems of these three molecules in this work provided by the controlling of the molecular structures and interfaces allows the study of the basic physics and to find the important parameters necessary to improve organic devices.

1.3 Organization of The Thesis

This thesis is organized as follows.

After this introduction, Chapter 2 give the principles of apparatus for the studies presented here. The principles of the morphology characterization method including Scanning Tunneling Microscopy (STM), Atomic force microscopy (AFM), Optical Microscopy (OM). The principle of X-ray diffraction (XRD) is then discussed. Finally, the principles of Photoemission Spectroscopy (PES) including Ultraviolet photoelectron spectroscopy (UPS), X-ray photoelectron spectroscopy (XPS) and Angle resolved photoemission spectroscopy (ARPES) are introduced.

In the Chapter 3 we will describe the experimental systems used in this work. The home-made vacuum chamber equipped with STM system, Ar^+ sputtering system and molecule evaporation system are introduced.

In the Chapter 4, the results of the study of fabrication of highly oriented multilayer films of picene and DNTT on their bulklike monolayer is presented. We first fabricated and characterized the monolayer of picene and DNTT. Then, we fabricated well-defined crystalline films of picene and DNTT on their well-ordered monolayers with a bulklike molecular arrangement. We will emphasize that much better crystalline films have been realized using picenes in comparison with DNTT. The superior growth found in picene films may be

attributed to the stronger intermolecular force constant, as suggested from the analysis of the normal vibrational modes of the single- crystalline structure of these molecules.

In the Chapter 5, the study on the morphology and electronic structure of peculiar sumanene monolayers and fabrication of sumanene thin films are presented. First, we have realized the bowl-stacking of sumanene monolayer on Cu(111). Then, we characterized the electronic structure of two kinds of peculiar sumanene monolayers which shows bowl-stacking molecular arrangement and bowl-up and bowl-down molecular arrangement, respectively, by UPS, XPS and ARPES. We also calculated the force constant of intermolecular van der Waals force of sumanene. Finally, the fabrication of superior sumanene thin films on Cu(111) suggested that the stronger intermolecular interaction along the bowl-stacking direction in monolayer can stabilize the further stacking molecules.

In the Chapter 6, the conclusion of the entire thesis is presented.

Chapter 2

Principles

2.1 Scanning Tunneling Microscopy (STM)

Since the scanning tunneling microscope (STM) was developed in the early 1980s by Gerd Binning and Heinrich Rohrer, who were awarded the Noble Prize in Physics in 1986 for this invention, it was widely used in the field of surface science. STM can investigate the structures and properties of surface in atomic resolution. With this resolution, individual atoms on the surface of materials can be routinely imaged and manipulated. The STM can be used not only in ultra-high vacuum condition but also in air, water, and gas ambient, and at wide temperature ranging. In this section, the theory and principle of STM operations are reviewed.

2.1.1 Theory of The STM

- **Bardeen's theory**

STM is based on the concept of quantum tunneling[30–33]. It is operated by probing the tunneling current between the STM tip and sample when the STM tip is very close to the surface with applied potential difference between them. We considered two electrodes a and b, they have independent potentials with Hamiltonian H_a and H_b (Figure 2.1). Electrons in these electrodes have wave function φ_a and φ_b. Eigenstates of each Hamiltonian

$$\mathrm{H}_a\,\varphi_a = E_a\varphi_a \ , \ \mathrm{H}_b\varphi_b = E_b\varphi_b \quad (2.1)$$

$$\mathrm{H}_a\,\varphi_b = 0 \ , \ \mathrm{H}_b\,\varphi_a = 0 \quad (2.2)$$

where E_a and E_b are intrinsic energy.

The total Hamiltonian of the entire system is

$$\mathrm{H} = \mathrm{H}_a + \mathrm{H}_b + \mathrm{H}^T \quad (2.3)$$

Where H^T is regarded as driving electron transitions from one side to the other.

At the initial time t=0, the state φ_a of an electron is

$$\psi_{t=0} = \varphi_a \quad (2.4)$$

Then, after the time interval t, the wave function is

$$\psi(t) = \alpha(t)\varphi_a \exp\left(-\frac{iE_a t}{\hbar}\right) + \beta(t)\varphi_b \exp\left(-\frac{iE_b t}{\hbar}\right) \quad (2.5)$$

Schrodinger's time-dependent equation

$$\mathrm{H}\psi = i\hbar\frac{\partial}{\partial t}\psi \quad (2.6)$$

$|\beta(t)|^2$ is the probability to find electron in state b. Substituting (2.5) into the Schrodinger's time-dependent equation

$$\frac{|\beta(t)|^2}{t} \approx \frac{2\pi}{\hbar}|M_{ba}|^2\rho(E_b)\delta(E_b - E_a) \quad (2.7)$$

where M_{ba} called the matrix element for transition from state a to state b.

$$M_{ba} = \int \varphi_b{}^*|\mathrm{H}^T|\,\varphi_a d\tau \quad (2.8)$$

According to Bardeen's theory

$$M_{ba} = \frac{\hbar^2}{2m}\int(\varphi_b{}^*\vec{\nabla}\varphi_a - \varphi_a\vec{\nabla}\varphi_b{}^*)d\vec{S} \quad (2.9)$$

and the tunneling current is given by

$$I_t = \frac{2\pi e}{\hbar}\sum_{b,a} f(E_b)\{1 - f(E_a + eV)\}\delta|M_{ba}|^2(E_b - E_a) \quad (2.10)$$

where $f(E)$ is the Fermi-Dirac distribution of eletrons at energy E, V is the bias voltage between two electrodes.

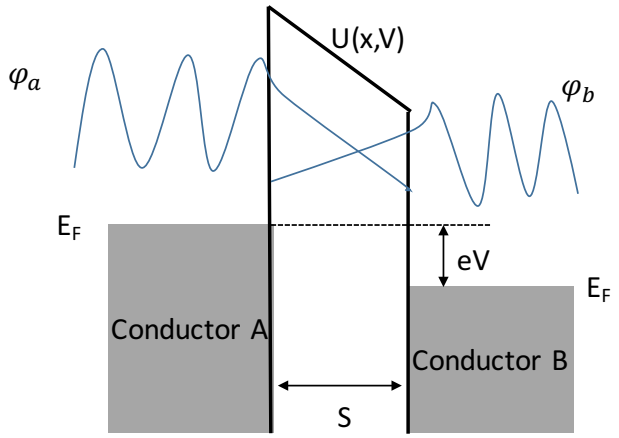

Figure 2.1 Diagram of initial and final states in the tunneling Hamiltonian picture.

- **Tersoff-Harmman's theory**

Figure 2.2 shows the diagram of the tip of Tersoff-Hamman's theory[34]. Simply assuming the wave function of the tip is a spherical wave, the wave function of the sample is a plane wave. Then, at low temperature and small bias voltage V, the tunneling current becomes

$$I_t = \frac{2\pi e}{\hbar}V\sum_{b,a}|M_{ba}|^2\delta(E_b - E_F)\,\delta(E_a - E_F) \quad (2.11)$$

where E_F is the Fermi energy. The finally tunneling current of can be obtained after the s-wave approximation for the tip

$$I_t \propto V \cdot n_t(E_f)\exp(2\kappa R)\sum_a|\varphi_a(r_0)|^2\,\delta(E_a - E_F) \quad (2.12)$$

where κ is the decay rate, $n_t(E_f)$ is the density states at the Fermi level of the tip, R is the effective tip radius and r_0 is the center of the curvature of the tip as shown in Figure 2.2.

$$2\kappa = 2\sqrt{\frac{2m\phi_{LBH}}{\hbar^2}} \quad (2.13)$$

where ϕ_{LBH} is the local tunneling barrier height. The important part is

$$n_x(E_F, r_0) = \sum_a |\varphi_a(r_0)|^2 \, \delta(E_a - E_F) \quad (2.14)$$

which is the surface local density of state (LDOS) at the Fermi level E_F. The tunneling current can be expressed as

$$I_t \propto n_x(E_F, r_0) \quad (2.15)$$

Since

$$|\varphi_a(r_0)|^2 \propto \exp\left[-2\kappa(s+R)\right] \quad (2.16)$$

Therefore, the tunneling current is dependent on the distance s between the tip and sample surface. Thus, the STM image can reflect the morphology of the sample surface.

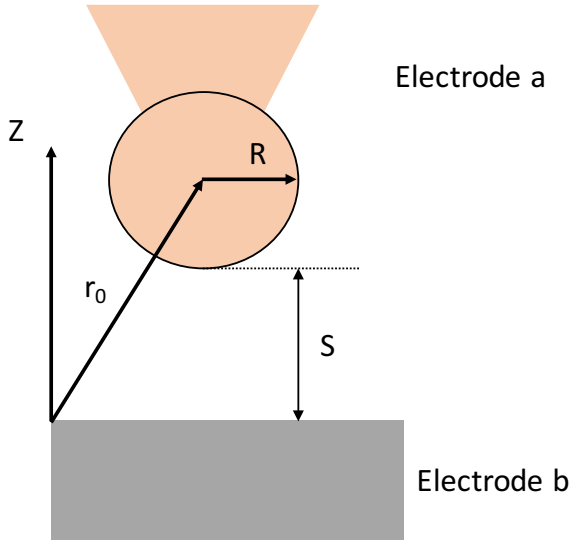

Figure 2.2 Diagram of STM tip.

2.1.2 Principle of Operation

The tunneling current between the sample and the STM tip can be detected after approaching the STM tip to the sample surface with applied potential difference of about tens mV to volts between them. By scanning the tip along the surface, the pattern of the surface topography can be obtained. There are five main variable parameters in STM operation system, the lateral coordinates x and y, the height z, the bias voltage V, and the tunneling current I. Different scanning modes of STM operation are defined depending on the manner in which these five parameters are varied. In this sub-section, two most widely used modes of STM operations, constant-current and constant-height modes are discussed.

- **Constant-Current Mode (CC)**

In this mode, tunneling current I and bias voltage V are kept constant when the tip is scanned across the surface as shown in Figure 2.3. Since the tunneling current is deeply depending on the distance between the probe and sample surface, to maintain the tunneling current at a present value, an adjustment of the vertical height of the tip from the sample surface by variation of the feedback voltage V_z on the z-piezoelectric driver was deduced. While the lateral coordinates x and y are determined by the corresponding voltage V_x and V_y

applied to the x and y piezoelectric drives. Therefore, the feedback signal $V_z(V_x , V_y)$ is acquired as a information that can be translated into the surface features of the surface topography.

As the most widely used technique for acquiring STM images, CC has no great requirement for the flatness of the sample surface, even though the probing surface is not atomically flat. Because this mode shows the advantages of the ability to determine the surface height and sensitivity of the piezoelectric driver. However, a significant drawback of CC lies in a finite response time of the feedback loop. In order to make these precise measurements without delay, the scanning speed is limited.

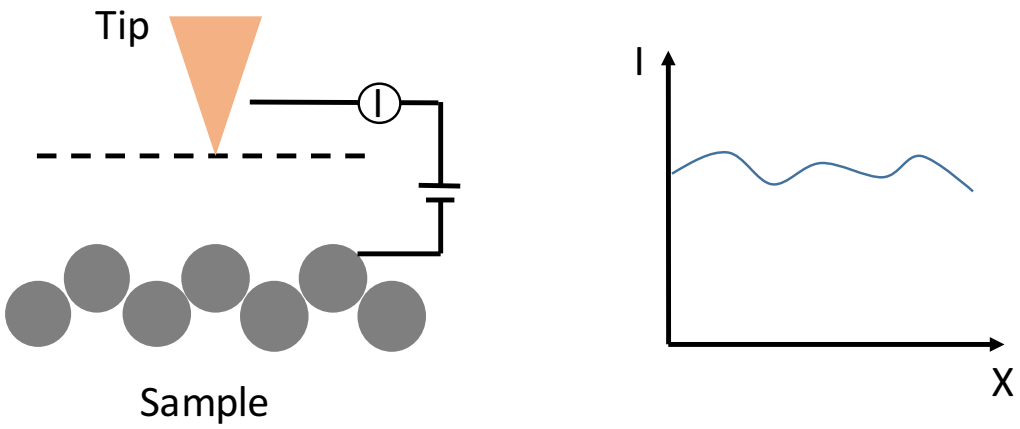

Figure 2.3 Diagram of Constant-Current Mode.

- **Constant-Height Mode (CH)**

Constant-height mode, which is also called current imaging. Unlike CC, in simple terms, the tip height z and the bias voltage V are kept constant during scanning in CH as shown in Figure 2.4. The atomic-scale topography can be reflected by the variations of tunneling current which are recorded as function of a tip position.

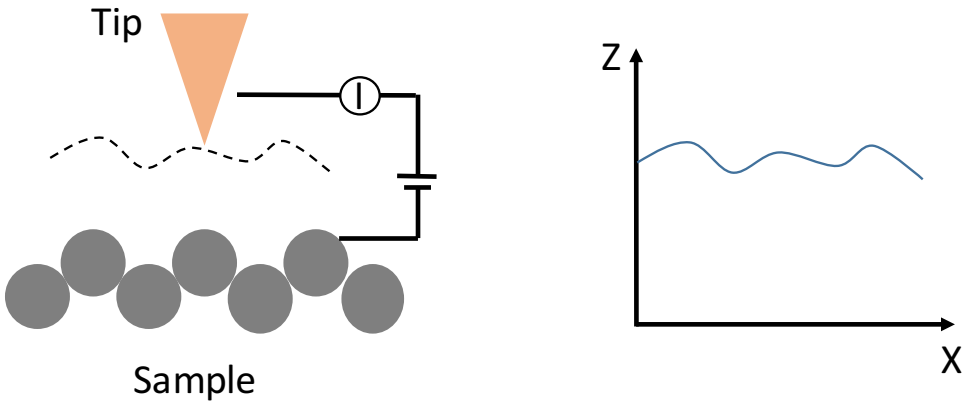

Figure 2.4 Diagram of Constant-Height Mode.

Since the speed of rastering the tip in CH can be done greater than in CC, the CH mode is faster than CC mode. This shows the ability of CH for studying real-time dynamic process at atomic scale at surface, such as

surface diffusion. However, the CH also shows the disadvantages, such as the application only for relatively flat surfaces; and it is difficult to estimate the topographic heights quantitatively from variation of tunneling current. Therefore, the CC mode is usually used to get topographic STM data on a large scale. Whereas, the CH mode can be used at smaller scanning area with sufficient flatness.

2.2 Atomic Force Microscopy (AFM)

After the successful achievement of the scanning tunneling microscopy (STM), the development of a set of novel scanning probe microscopy methods has been inspired. The atomic force microscope (AFM) was invented by Binning, Quate and Gerber in 1986. It is well known for measurement and surface manipulation of sample in nanometer scale.

2.2.1 Working Principle

The principle of AFM operation is illustrated in Figure 2.5. An AFM typically consist of the following components:

A sharp tip located at the free end of the cantilever.

A way of sensing the deflection of cantilever (photo-diode plus laser). Several techniques are in use for detection of the small displacements of the cantilever.

A feedback control system to monitor and control the cantilever deflection.

A mechanical scanning system. A piezoelectric actuator is used to move the sample respect to the scanning tip.

A display system that can converts the acquired data into an 3D image.

During the AFM measurement, the interaction forces between the tip and the sample surface cause the cantilever to deflect. The displacement of the cantilever will be detected by a deflection sensor.

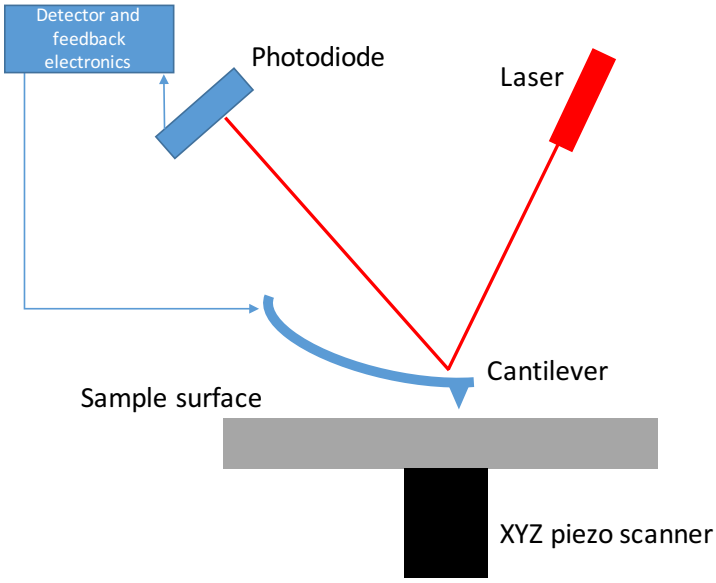

Figure 2.5 Diagram of the set up of an AFM.

Considering the interaction of tip and sample as shown in Figure 2.6, when the distance between the tip and sample is relatively large, the cantilever is weakly attracted to the sample surface. There is no deflection on the cantilever. After the tip is pulled toward the surface, it comes to the attractive regime. When the distance decreasing, the attractive force between tip and sample will increase until the repulsive force becomes small enough that the electron clouds of the tip and sample atoms begin to repel each other, then comes to the repulsive regime, where the tip is hard contact with the surface. The range of the separation between the tip and sample used for AFM imaging defines the operation modes.

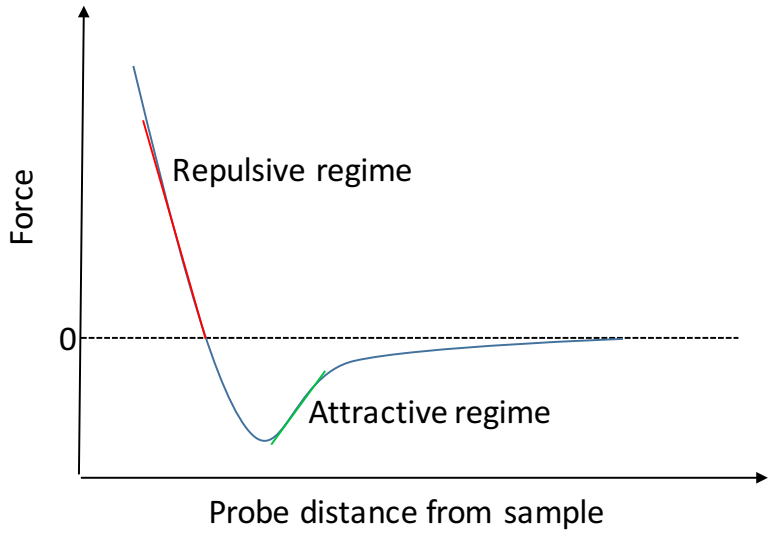

Figure 2.6 Van der Waals force and distance curve.

2.2.2 Operation Mode of AFM Measurement

- **Tapping mode**

The AFM can be operated in various modes, such as contact mode, non-contact mode and tapping mode, but tapping mode is the most widely used operating mode for topography imaging. This mode is similar to non-contact mode, the distance between the tip and sample is conventionally on the order of tens to hundreds of Å with the relatively weak interactions. During the scanning, the cantilever is kept vibrating near its resonance frequency ahout 100 to 400 kHz with the typical amplitude of a few tens of Å. After interacting with the sample, the cantilever resonance frequency f_1 changes

$$f_1 \propto \sqrt{c - F} \quad (2.17)$$

where c is the cantilever spring constant and F is the force gradient. Tapping mode does not provide atomic resolution but appears to be advantageous for imaging rough surfaces with high topographical corrugation.

2.3 X-ray Diffraction (XRD)

2.3.1 Principles of XRD

XRD is a technique used for determining the atomic and molecular structure of a crystal. X-rays can be considered waves of electromagnetic radiation. When a propagating X-ray wave encounters some regularly spaced particles, where the wavelength is in the same order of magnitude as the spacing between the particles, then diffraction occurs as shown in Figure 2.7. Bragg's law gives a condition for the intensity fo the diffracted beam related to the angle between the diffracted beam and solid.

- **Bragg's law**

Assume the parallel planes A and B of a crystal as shown in Figure 2.8. The spacing between the planes is given by d_{hkl}, where h, k and l are the miller indices of the plane. A beam of X-ray with wavelength λ approach the plane under an angle θ. Constructive interference occurs when the diffracted waves have the same phase. The Bragg's law

$$n\lambda = 2d_{hkl}\sin(\theta) \qquad (2.18)$$

relates the diffraction angle to the inter planar spacing d_{hkl}.

$$d_{hkl} = \frac{1}{\sqrt{(\frac{k^2}{a^2}+\frac{h^2}{b^2}+\frac{l^2}{c^2})}} \qquad (2.19)$$

where a, b and c show the lattice parameters. Then, the miller indices h, k and l can be used to present by the diffraction angle of XRD spectrum.

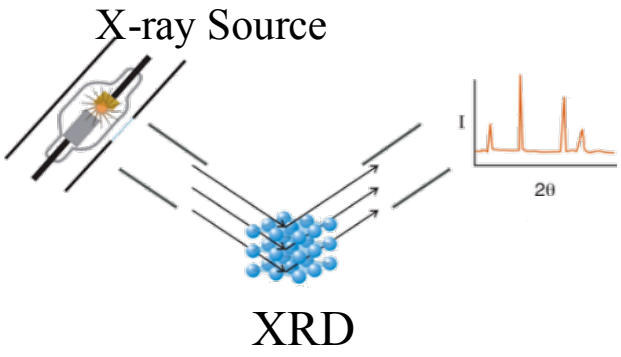

Figure 2.7 Diagram of XRD system.

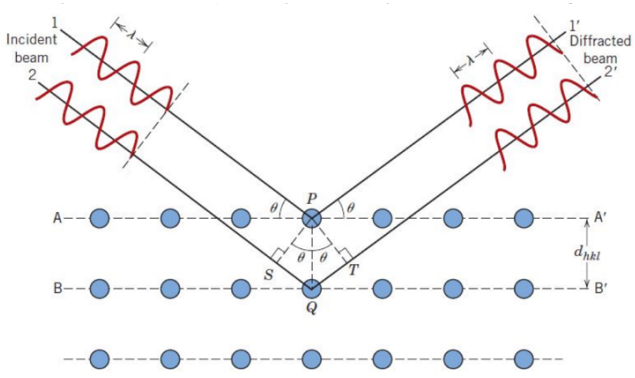

Figure 2.8 Diagram of Bragg's law.

2.3.2 Diffraction Pattern

- **Powder diffraction**

For powder crystals, it is stress-free and all crystals are randomly orientated. By using powdered crystals, all reflections of the crystallographic planes should be visible in the diffraction pattern. The relative intensities of the reflections should be similar, since at every angle the reflection of all planes is measured due to the

randomness in the powder. The powder spectrum is very useful when we want to identify the different components structure in a material. Therefore, some theoretical powder
diffraction patterns with the planes corresponding to their Bragg peaks. The width and the absolute height and the relative intensity of the individual peaks of these calculated Bragg peaks are not representative for real powder diffraction patterns, but they are just randomly chosen.

- **Thin film recrystallization**

Thin film measurements are more difficult to analyze, because not all reflections of crystallographic planes might be visible in the diffraction pattern. Crystals can grow in a specific orientation that results in a preferred orientation. Therefore, one particular plane is much more common than another plane, which is not the case in a powder. This affects the relative intensities of the reflections. When there is a very strong preferred orientation, then it might be possible that only at one specific angle the reflection of a crystal is visible and that all the other reflections have disappeared. Therefore, analysis of a thin film's diffraction is always along with the comparison with the powder pattern.

2.4 Photoemission Spectroscopy (PES)

Photoelectron spectra show the information about the density of states, the type of atoms, the presence ratio, and the state of chemical bonding by breaking down the energy distribution of photoelectrons. According to the energy of light classified as X-ray photoelectron spectrum (XPS) and Ultraviolet Photoelectron Spectroscopy (UPS). XPS was used to study the energy levels of atomic core level electronics. UPS is used to study valence energy levels and chemical bonding, especially the bonding character of molecular orbitals.

2.4.1 Principle of PES

The PES technique is an application of the photoelectric effect. As shown in the diagram of Figure 2.9. When the sample was exposed to the UV or XUV with the energy of $E = h\nu$, photoelectric ionization occurred. The photoelectrons that actually escaped into the vacuum are collected and energy resolved. The kinetic energy of the photoelectrons E_{kin} is

$$E_{kin} = h\nu - E_B - \phi_s \quad (3.1)$$

where E_B is binding energy, ϕ_s is the work function. Therefore, the energies of the continuous emitted photoelectrons are characteristic of their original electronic states as shown in the spectrum.

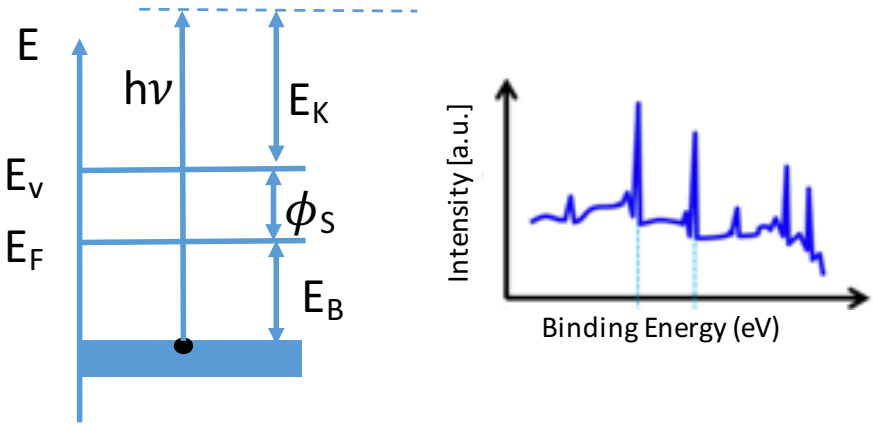

Figure 2.9 (Left)Diagram of the energy level of photoemission experiment showing the initial state energy, the Fermi level, the vacuum level and the final state energy; (Right)A model of XPS spectrum showing the distribution of the intensity of photoelectrons respect to the binding energy.

2.4.2 ARPES

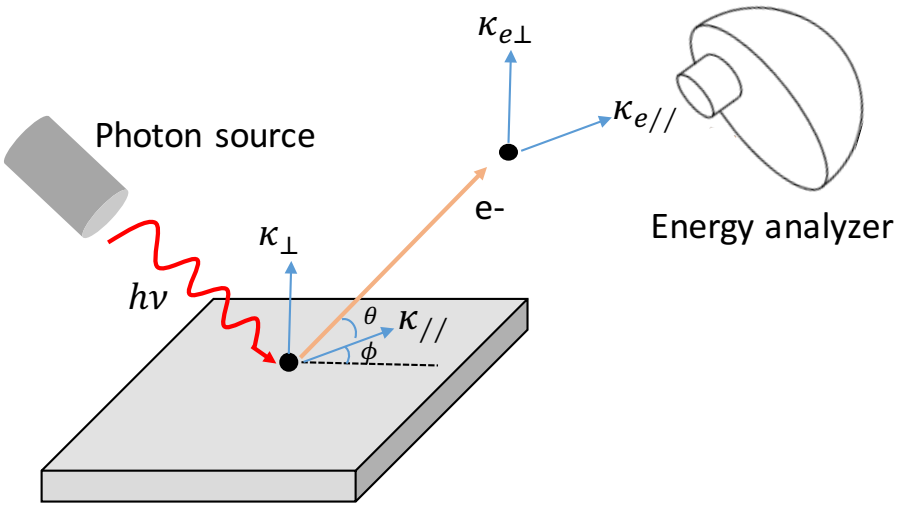

Figure 2.10 An experimental setup of ARPES. An incident photon with energy $h\nu$ excites an electron from initial state characterized by the momentum vector $\kappa_{//}$ to the final state characterized by the momentum vector $\kappa_{e//}$. The polar angle θ and azimuthal angle ϕ define the direction of the photoemitted electron.

In ARPES, the angle of emission of an electron is introduced to the PES shown in figure 2.10. The energy analyzer allows simultaneous collection of photoelectrons over a polar angle θ range of 180° in the specular plane. Azimuthal scans are then made by rotating the sample around the surface normal in 1° steps of azimuthal angle ϕ. The energy and momentum parallel to the surface are conserved during the photoemission process, the detection of energy and momentum of the emitted electrons probes the band structure of the sample. The translational symmetry requires that the component of electron momentum in the plane of the sample be conserved, therefore,

$$\hbar\kappa_{e//} = \hbar\kappa_{//} = \sqrt{2mE}sin\theta \quad (3.2)$$

where $\kappa_{e//}$ is the momentum of the outgoing electron, $\kappa_{//}$ is the initial momentum of the electron, E is the detected kinetic energy of the the photoelectrons. Therefore, we can realize the electron distribution by measuring the emission angle and corresponding energy of the photoelectrons. ARPES provides the information of the absolute location of energy bands at different points relative to the Fermi level in k-space.

Chapter 3

Experimental Systems

In this chapter, the experimental apparatus used in this work is introduced. The ultra-high vacuum chamber equipped with substrate cleaning system, molecule evaporation system and measurement system of STM, was used to fabricate and keep the samples. In addition, PES was performed at UVSOR BL-2B and KEK BL-13B.

3.1 Vacuum Chambers

The characterization of a solid surface on an atomic level needs an unchanged surface composition over the duration of an experiment. This requires that the rate of arrival of reaction species from the gas environment should be low, i.e. vacuum environment.

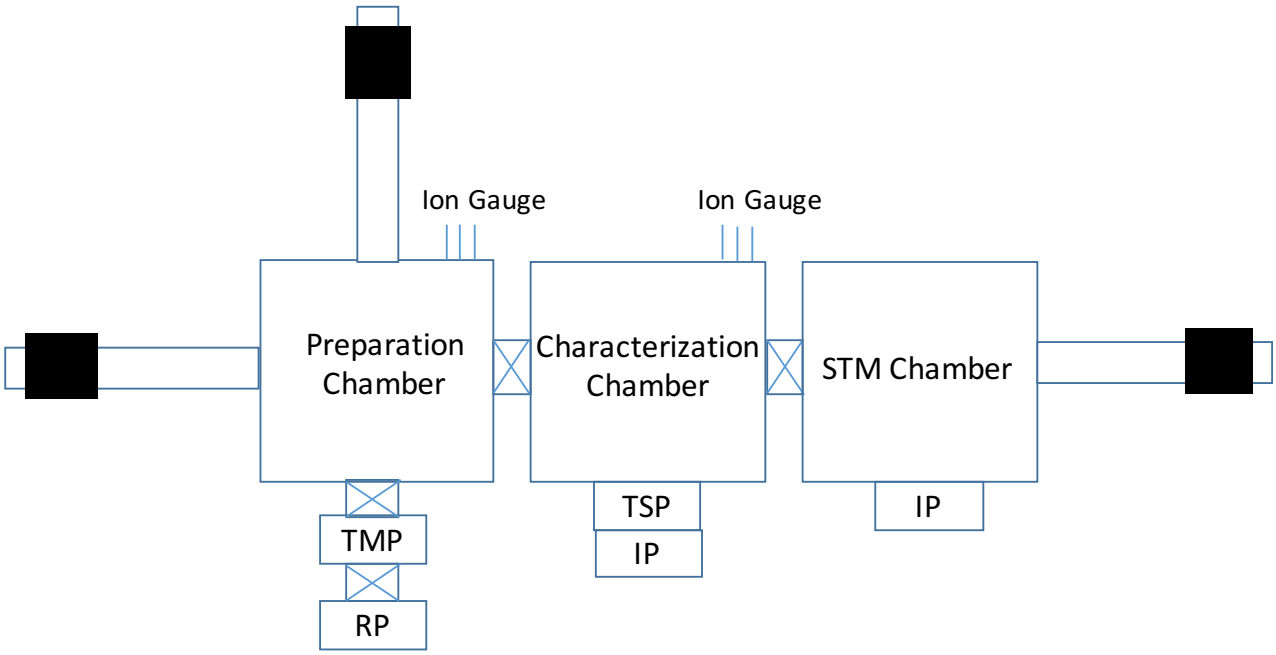

Figure 3.1 Schematic diagram of the experimental apparatus.

All the experiments in this thesis were performed in an ultrahigh vacuum environment with the vacuum pressure of about 1×10^{-9} Torr at room temperature. The UHV in the chamber is mainly produced by a combination of a pumping system with a rotary pump (RP), an ion pump (IP) and a turbo molecular pump (TMP). The pressure in the chamber is monitored by an ionization gauge. The pumps and gauges connected by tubes to the chamber and to each other comprise the pumping system. The whole equipment consists with preparation chamber, characterization chamber and STM measurement chamber, which are connected together. Every chamber in the vacuum system is isolated and can separated by a gate value. Samples can be transferred

between each chamber by means of magnetic-drive linear transfer rods. The schematic diagram of the experimental apparatus of this work is shown in Figure 3.1.

Introduction of samples and STM tips to the UHV system was done after introducing clean N_2 gas through the equipped leak value of the chambers, which can bring up the chamber to atmospheric pressure.

3.2 Substrate Cleaning System

We start with the experiment in the vacuum system once the UHV condition are ensured. Usually, the first thing needs to be done is the preparation of the clean sample surface. Because we need an atomically clean well-ordered surface which can been conducted only in situ in the UHV chamber. The main techniques for cleaning the samples in situ in UHV chamber are cleavage; heating; chemical processing and ion sputtering. In the works of this thesis, we use the method of the combination of Ar^+ sputtering and annealing by filament to clean the metal substrates.

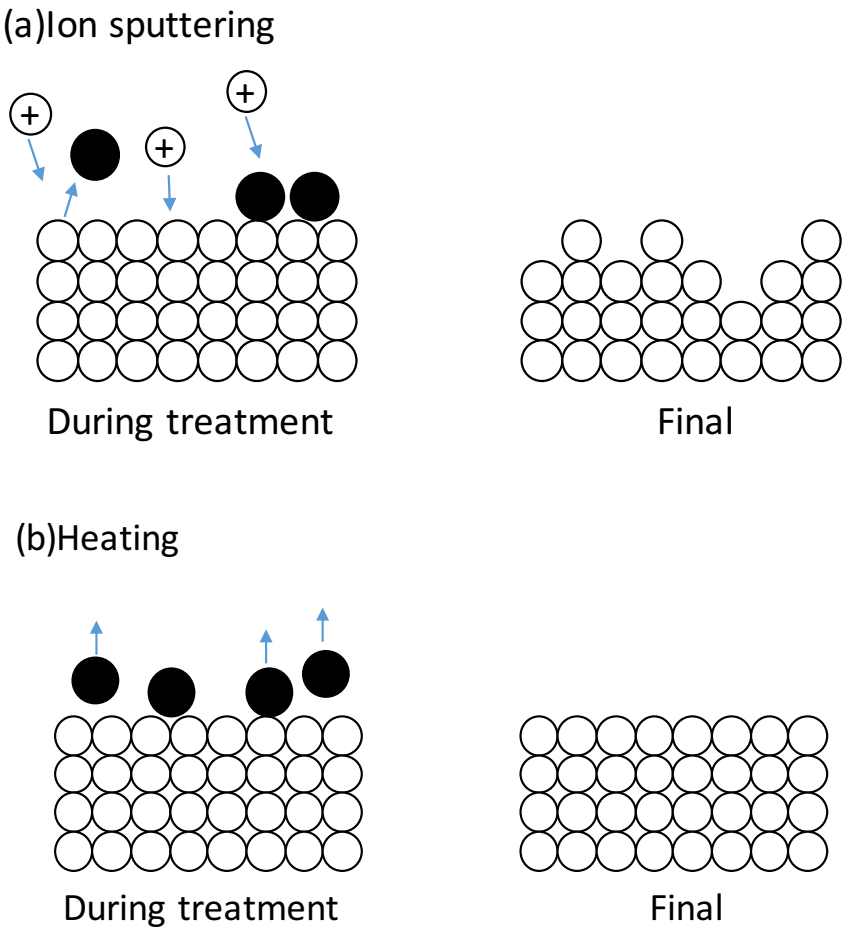

Figure 3.2 Schematic diagram illustrating the techniques for cleaning the samples in situ in UHV chamber. (a) Ion sputtering; (b) Heating.

The Ar^+ ion beam is carried out using UNISOKU's sputter ion gun (IB-102). Firstly, to produce an ion beam, Ar gas is introduced through a leak valve directly into the ionization chamber. At the same time, current is added to the filament to generate hot electrons, and a high electric field added to the filament accelerate the electrons. Therefore. the accelerating electrons can collide with Ar gas, leaving Ar in an ionized state. Then, the electrode in front of the ionization chamber accelerates the Ar^+ ion beam to the substrate surface. Thus, impurities on the substrate surface can be removed. We should note here, we always connect the substrate to earth during the sputtering, because this reaction can prevent the sample from charging up. Ion sputtering is a very effective cleaning technique. However, the ion bombardment can cause a degradation of the surface structure. Therefore, subsequent annealing is required to restore the crystallography of sample surface at an atomic level, which can also remove the embedded and adsorbed Ar atoms. We always heating the sample by the filaments installed on the sample holder. The schematic diagram illustrating the heating and ion bombardment techniques is shown in Figure 3.2. In practice, several ion sputtering and heating cycles are required to obtain a well-ordered atomically clean surface.

3.3 Molecule Deposition System

3.3.1 Deposition Source

Most UHV deposition technologies employ thermal evaporation or sublimation of materials. In this thesis, thermal evaporation of molecules was employed to prepare well-ordered adlayers on metal surface in UHV condition. The home-made deposition source with simple design, which was made of Ta material, is used in this thesis. The deposition procedure was carried out by heating the evaporator with adding current to it. This kind of evaporator can be made easily with any shape and size, which is benefit for different requirements of the experimental design.

3.3.2 Deposition Monitor

A quartz crystal thickness monitor is mainly used for measuring the deposition rate and final film thickness, which are the most parameters for the deposition process. The relationship between the fundamental vibration frequency $\boldsymbol{f_0}$ of quartz crystal and the crystal thickness $\boldsymbol{d_q}$ is

$$\boldsymbol{f_0} = \frac{N}{\boldsymbol{d_q}} \quad (3.3)$$

where $N = 1.67\times10^6\ Hz \cdot mm$. When the molecules come to the surface of the crystal, it will cause a mass increase by Δm and lower its frequency by Δf

$$\Delta f = \frac{\boldsymbol{f_0}^2 \Delta m}{\rho_q N A} = \frac{N \Delta m}{\rho_q A \boldsymbol{d_q}^2} \quad (3.4)$$

where $\rho_q = 2.65\ g/cm^3$ is the density of the quartz; A is the area of the crystal.

3.4 STM System

The STM machine used in this experiment is the commercial STM made by UNISOKU. As shown in Figure 3.3, the system is mainly composed of a STM microscope unit, a STM control unit and a data manipulation unit.

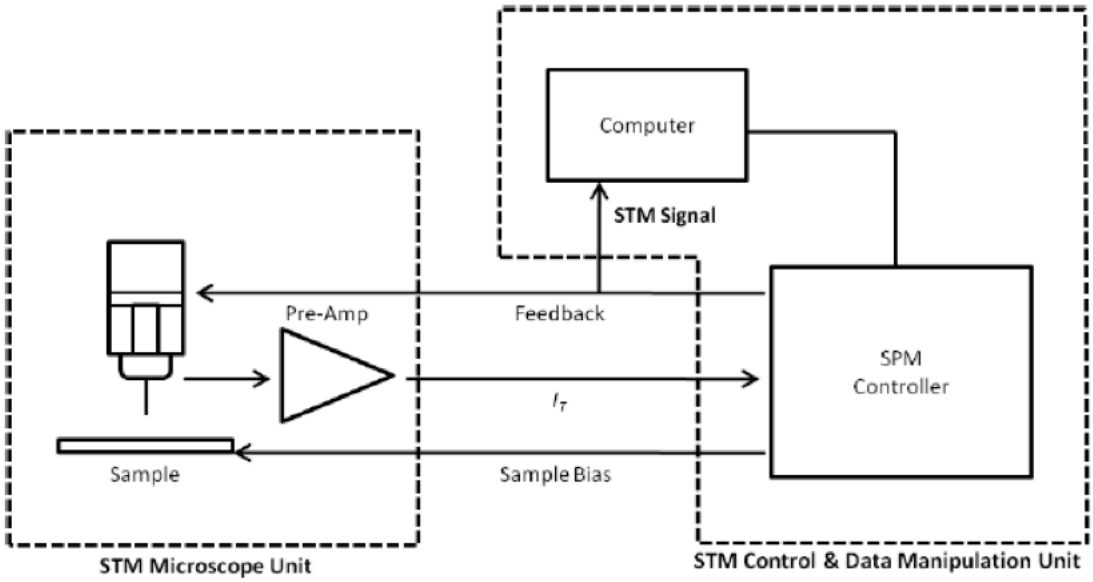

Figure 3.3 Schematic illustration of the STM set-up.

In the microscope unit, the sample is fixed on the sample holder which is installed on the system. A coarse positioning system can bring the tip to within the tunneling distance of the sample and, when required, to retract it back to a sufficient distance.

The control unit of STM is consist with an SPM controller of model system40 made by UNISOKU with a computer-automated system. The control method used for the controller is based on the proportional integral diffraction feedback method.

The data manipulation unit is consisting with data acquisition, analysis, processing and visualization.

3.5 Synchrotron

In this work, UPS and ARPES measurements were deduced in the beam line of BL-2B of UVSOR synchrotron facility of the Institute for Molecular Science. A hemispherical electron analyzer (R3000, Sienta VG) is equipped with a custom-built apparatus with the high resolution of $\frac{E}{\Delta E} = 2000 - 8000$.

XPS measurement was done in the beam line of BL-13B of KEK. Vacuum ultraviolet and soft X-ray undulator beamlines, BL-13B are mainly dedicated to the study of surface chemistry, using angle-resolved

photoelectron spectroscopy (ARPES), X-ray photoelectron spectroscopy (XPS), and X-ray absorption spectroscopy (XAS). The available photon energy region is 30 - 1600 eV and the typical photon intensity is 1012～108 photons/s.

All the beam lines are equipped with UHV chambers with substrate cleaning systems, molecule deposition systems, which can realize the in-situ detection measurement after the fabrication of the samples.

Chapter 4

Fabrication of Highly Oriented Multilayer Films of Picene and DNTT on Their Bulklike Monolayer

4.1 Introduction

Small organic semiconductors with enhanced intermolecular interaction, such as phenacenes and thienoacenes, have been attracting attention because high-quality single crystals or thin films are expected. In this study, we focused on picene and Dinaphtho[2,3-b:2',3'-f]thieno[3,2-b]thiophene (DNTT), as model molecules of phenacenes and thienoacenes, respectively. Indeed, the single crystalline picene shows the significant dispersion of the highest occupied molecular orbital (HOMO)[35,36], and organic field-effect transistors (OFETs) utilizing the single crystalline picene exhibit high carrier mobility of more than 1 $cm^2V^{-1}s^{-1}$ [37]. Theoretical calculations have suggested that the single crystalline picene can exhibit a maximum mobility up to 2.6 $cm^2V^{-1}s^{-1}$ along the π–π stacking direction[38]. OFETs based on single crystalline DNTT, on the other hand, have shown the mobility as high as 10 $cm^2V^{-1}s^{-1}$ [39]. However, OFETs utilizing the thin films of these molecules have exhibited much lower hole mobility, such as 0.1–0.3 $cm^2V^{-1}s^{-1}$ for picene[40] and 2.9 $cm^2V^{-1}s^{-1}$ for DNTT [41]. These facts suggest that further optimization of the thin film structure of these organic semiconductors is required.

There have been common problems in the growth of the multilayer film of these π-conjugated planar molecules; the monolayer of these molecules on the flat substrates usually take a "flat-lying" or "face-on" conformation due to significant coupling between π orbital of molecules and the surface electronic states, while the second layer does not usually follow the configuration of the monolayer and tend to "stand up". This mechanism usually leads to a dendritic growth of the multilayer with a complicated morphology and small domain sizes [42–45]. Even in the case of a carefully optimized deposition utilizing the supersonic molecular beam deposition of picene, the reported grain size of the film is in the range of several micrometers [46]. The morphology of the monolayer is shown to be one of the key for the structure of multilayer film of organic semiconductors [6]. We have recently reported that the careful deposition of picene and DNTT on the flat surfaces can form a corrugated monolayer in which half of the molecules take a "side-on" geometry [14]. The same growth feature can also be seen in other phenacenes [15]. The molecular ordering of the monolayer resembles the (110) plane of the bulk crystal, although they are not identical, which is distinct from the case of the similar π-conjugated molecules such as pentacene, and this phenomenon should reflect the strong intermolecular interaction of these molecules. The bulk-like monolayers could be useful for further stacking of flat-laying molecules on it, which can potentially yield a high-quality multilayer film.

Therefore, in this work, we have tried to grow the multilayer picene and DNTT on their peculiar monolayer. We indeed demonstrated here that the careful fabrication of the bulk-like monolayers and further slow deposition of molecules resulted in formation of extremely long (more than 100 μm in the case of picene) and unidirectional islands consisting of flat-lying molecules. We will emphasize that much better crystalline film has been realized using picene in comparison with DNTT. The superior growth found in picene film may be attributable to the stronger intermolecular force constant, as deduced from the analysis of the potential energy curves of the molecule dimers and normal vibrational modes of the single crystalline structure of these molecules. The growth of the flat-lying molecules, which is particularly efficient for small molecules with enhanced intermolecular interaction such as phenacenes, will be beneficial not only in for the applications in the organic electronics devices, but also in the basic researches of the structure-function relationship of organic semiconductors.

4.2 Substrate Materials and Experiment

4.2.1 Substrate Material and Cleaning Method

Single crystalline Au(111) was used as a substrate in this work. Solid gold is one of the most chemically inert substances where organic molecules adhere primarily through noncovalent van der Waals interactions. Au(111) has technical advantages in that it is relatively easy to obtain a clean atomically flat surface. It has been characterized to be the only face-centered-cubic metal that exhibits a reconstruction of the close-packed (111) surface, which shows both hexagonal-close packed and face-centered-cubic sites in the surface layer[49,50]. A large number of molecular assembly studies have been performed on this surface already.

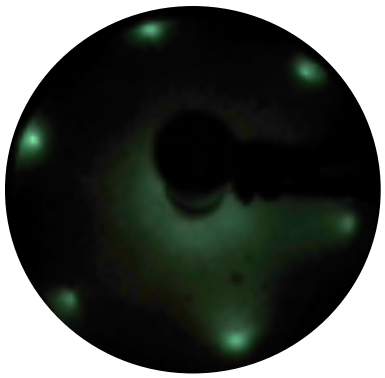

Figure 4.1 LEED spectrum of clean Au(111).

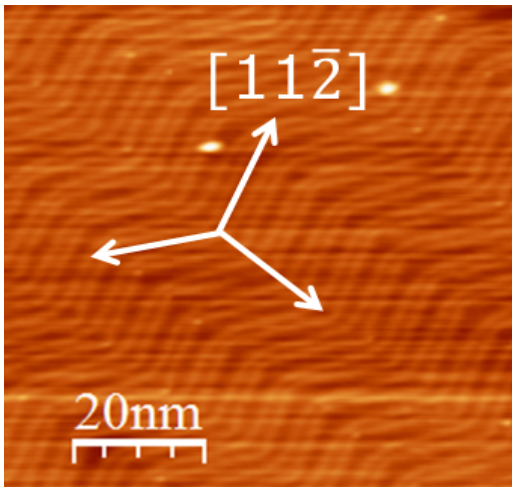

Figure 4.2 STM image of clean Au(111) with herringbone structure.

After introducing to the high vacuum system, the Au(111) substrate was cleaned by several cycles of Ar+ ion sputtering (pressure: 1.0×10^{-5} Torr, accelerating voltage: 1.5 KeV) followed by annealing at approximately 400 °C. The cleanliness of the substrate was examined by low-energy electron diffraction (LEED) as shown in Figure 4.1. The electron diffraction pattern was interpreted in terms of a superstructure with a local, twofold symmetry, which due to the higher, threefold symmetry of the face-centered-cubic (111) surface exists in three rotational domains. We also check the substrate surface by scanning tunneling microscopy (STM) with constant current mode. Herringbone reconstruction structure [17] of the Au(111) substrate was clearly observed by STM images as shown in Figure 4.2.

4.2.2 Fabrication and Characterization Method of Monolayer and Thin Film

The deposition of picene and DNTT molecules on the clean Au(111) substrate was performed in an ultra-high vacuum (UHV) environment about 1×10^{10} Torr with a homemade Knudsen cell which allow a slow deposition rate of approximately 1ML/1000s in order to ensure good crystallinity of the resultant film. The deposition was carried out at the substrate temperature of room temperature (300 K) by heating the molecule evaporator carefully degassed. The deposition rate was monitored by a quartz crystal microbalance equipped in the UHV chamber. The distance from the molecule evaporator to Au(111) substrate was 35 cm. The formation of monolayers of picene and DNTT was confirmed by LEED and STM observation. After that, the multilayer of picene and DNTT was deposited on the well-ordered monolayer at the same rate in UHV. Structural measurements of the multilayer were performed *ex situ* at room temperature. Morphology of the multilayer was observed by atomic force microscopy (AFM) conducted in the tapping mode under atmospheric pressure and optical microscope (OM). Crystallographic phase and molecular orientation in the film were characterized by XRD measurement, which was performed by a Cu Kα source X-ray of λ=0.15406 nm.

4.2.3 Calculation Method

For the calculation of force constant of intermolecular van der Walls force between molecules, firstly, one simplified calculation of potential energy curve of intermolecular van der Walls force are calculated with respect to dimer separation with the PM6-D3 method in this work. Here, the optimization of molecular structure of picene and DNTT molecules were performed by Density functional theory (DFT) calculations with Gaussian code using the B3LYP functional with the DFT/6-311+G basis set. All the orientation and structure of molecule dimers were established based on the settings of experimental structure. The dimer separation procedure was obtained with varying intermolecular distance. The distance denotes spacing of a pair of atoms between the two monomers, and the variation process the orientation and structure of the monomers keep fixed.

In order to prove the credibility of this simplified calculation results, another more precise calculation of the normal vibrational modes of crystal are obtained from the dynamical matrix constructed by the force field MMFF94s[52] using CONFLEX code[19]. Here, the optimization process starts with the experimental structure and the atomic positions are optimized at fixed lattice constants.

4.3. Picene and DNTT Monolayers on Au(111)

4.3.1 Morphology of Picene and DNTT monolayers

Firstly, we confirmed the formation of the a characteristic corrugated monolayers of picene and DNTT on a clean Au(111) substrate. It was seen that the picene and DNTT molecules adsorb in the flat-lying geometry at loose coverage, while the geometry transforms into a corrugated arrangement near the monolayer coverage[14].

- **Monolayers with loose phase**

Figure 4.3(a) shows the picene monolayers with loose phase. The direction of molecular rows respect to the substrate can be easily defined to be [11$\bar{2}$] according to the herringbone reconstruction structure of Au(111) substrate. As shown in the magnified picene monolayer STM image (Figure 4.3(b)), each oval structure represents a picene molecule. We can easily recognize the short edge and long edge along the molecular axis of each picene molecule according to the shape of the molecule in the STM image, indicating the "face-on" adsorption of picene molecules with the unit cell of 0.8×1.5 nm^2. Thus, the STM measurement shows that picene molecules prefers an adsorption model with short edge next to long edge along the molecular row. This kind of preferable arrangement has also been observed on Ag(100)[53] (Figure 4.4(a)). In addition, it has been reported recently that, picene monolayer with loose coverage on Ag(111) shows the preferable adsorption model with short edge next to short edge, long edge next to long edge. The DFT calculation result is shown in structure model (Figure 4.4(b)). These two calculation results may be caused by the different interaction between molecule and substrate.

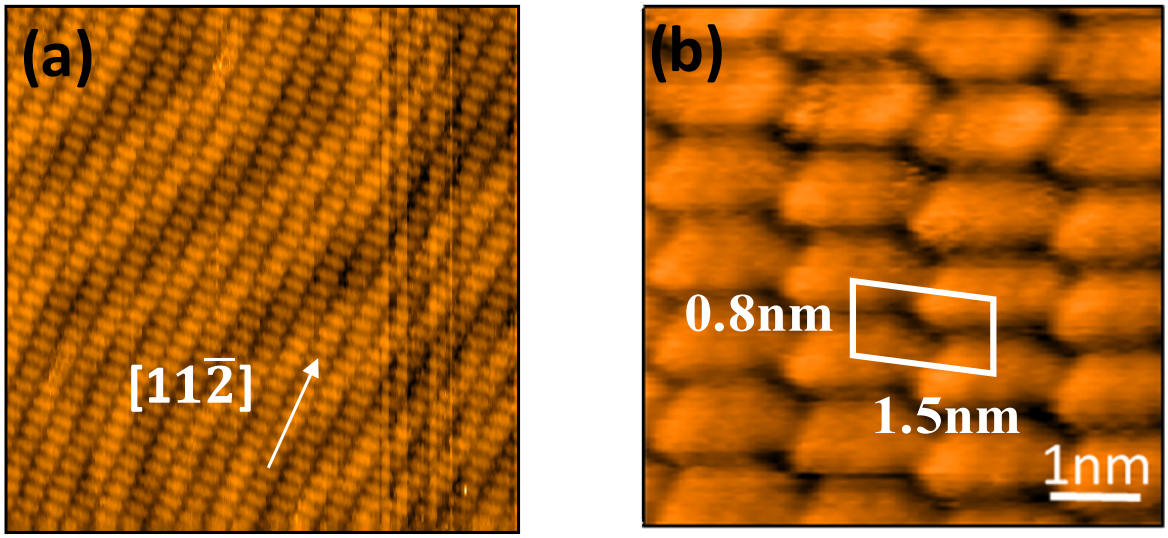

Figure 4.3 (a) STM image of picene monolayers with loose coverage. The direction of the molecular packing row is marked by white arrow. (b) Magnified picene monolayer STM image. The unit cell of molecular arrangement is also marked on the STM image.

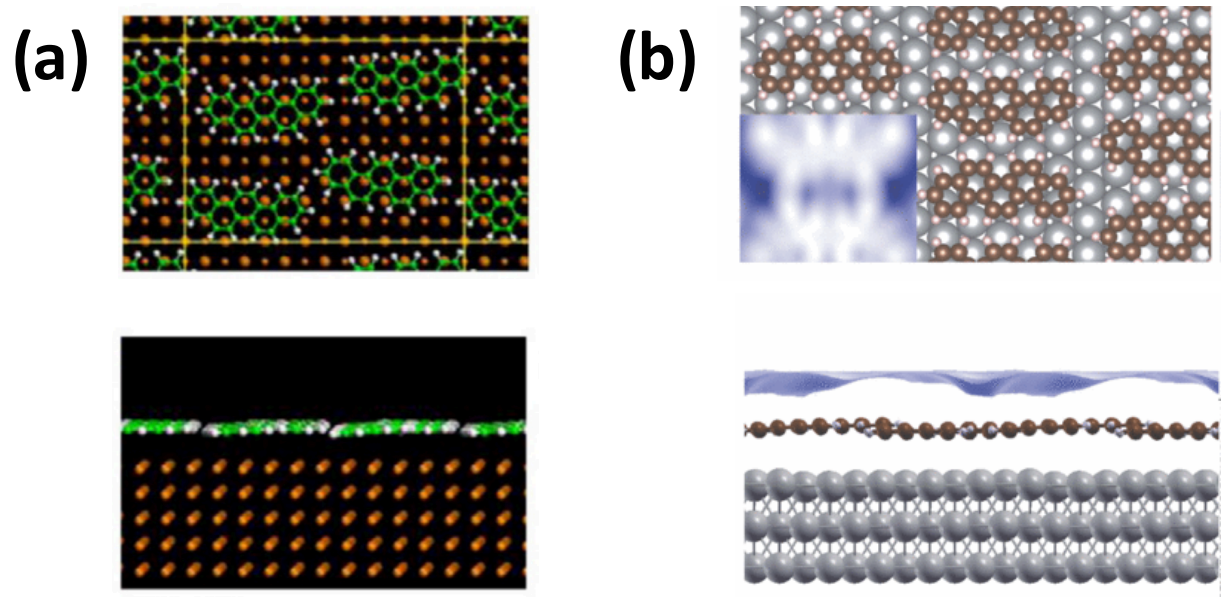

Figure 4.4 (a)[53]Adsorption configuration of Picene monolayer on Ag(100) at 0.5ML; (b)[54] Structure model of picene monolayer with loose coverage on Ag(111) by the DFT calculation.

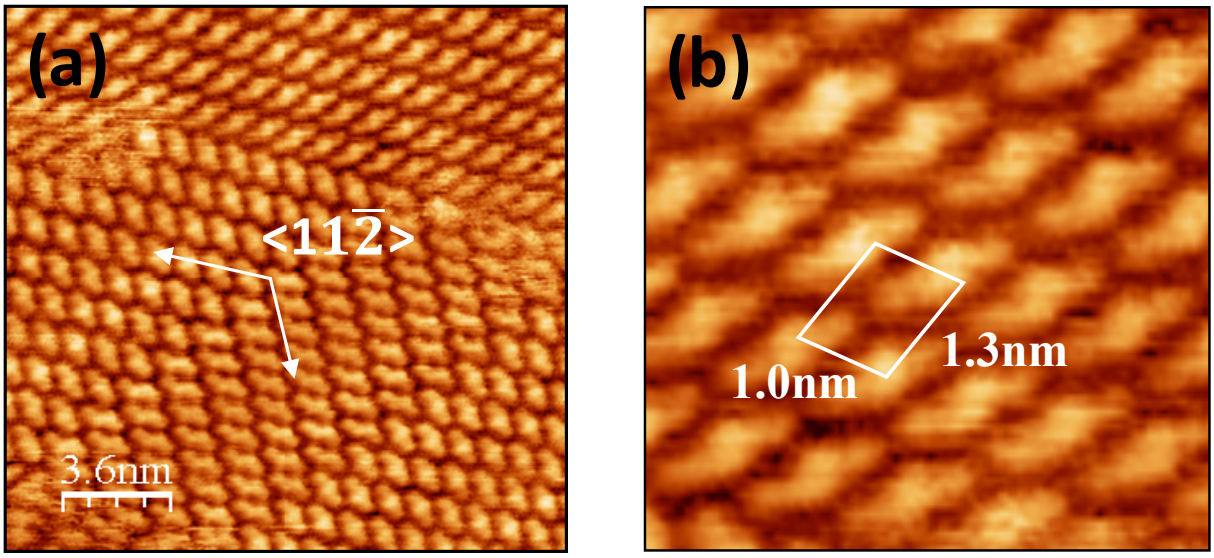

Figure 4.5 (a) STM image of DNTT monolayer with loose coverage; (b) Magnified STM image.

STM image of DNTT monolayer with loose coverage is shown in Figure 4.5. N shaped individual molecule, which corresponding to one DNTT molecule, can be observed. This phenomenon clearly indicates the "face-on" adsorption of DNTT molecules on the surface. Since the herringbone structure of Au(111) still can be recognized on the STM image, the molecular row direction can be defined to be [11$\bar{2}$]. The unit cell of this planar monolayer is shown to be 1.0×1.3 nm^2 (Figure 4.5(b)).

- **Monolayers with dense coverage**

With further deposition of picene and DNTT molecules, Figure 4.6(a) and 4.7(a) shows the dense monolayer structure of picene and DNTT on Au(111). As seen in the magnified STM image in Figure 4.6(b) and 4.7(b), the molecules in the monolayer show corrugated arrangements with the unit cell size of 1.1×1.4 nm^2 for picene and 1.1×1.6 nm^2 for DNTT. This corrugated arrangement may be caused by different adsorption angle of the molecules, i.e. half of the molecules take the tiled arrangement, the other half of the molecules take the "face-on" arrangement. Similar corrugated arrangement of picene on Ag(111) and Ag(100) was also observed. The diagram of molecular arrangement is shown in Figure 4.8.

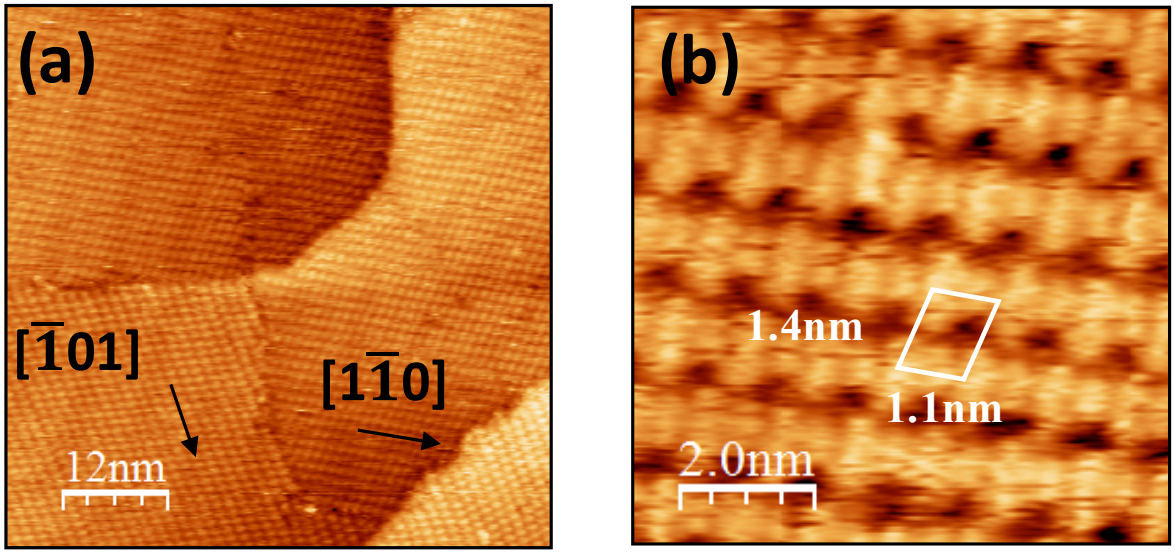

Figure 4.6 (a) STM image of picene monolayer with dense coverage; (b) Magnified STM image.

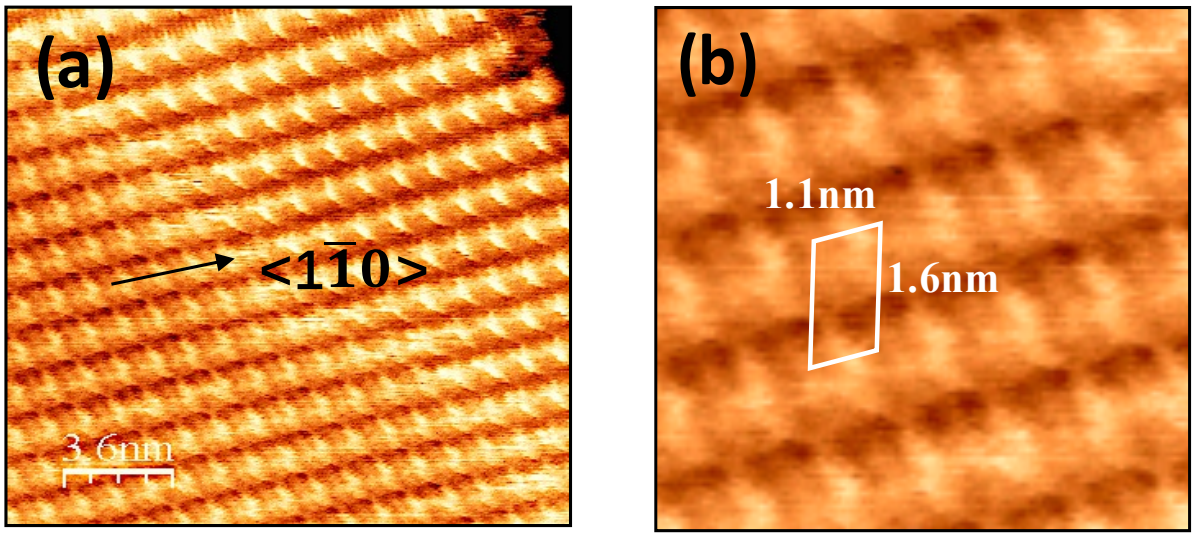

Figure 4.7(a) STM image of DNTT monolayer with dense coverage; (b) Magnified STM image.

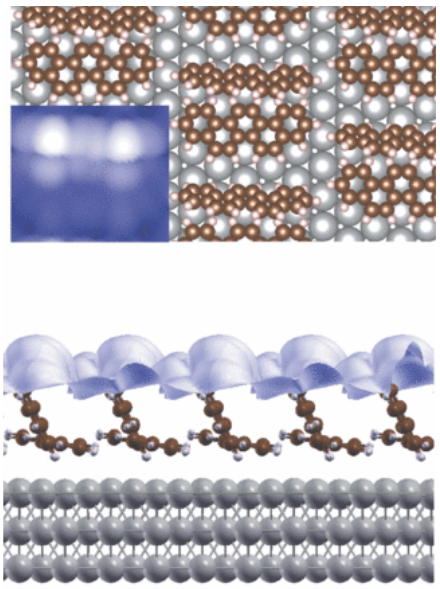

Figure 4.8[54] Diagram of picene monolayer on Ag(111) with dense coverage by the DFT calculation.

Both phases of picene and DNTT do not appear to strongly interact with the substrate because the herringbone reconstruction structure of the Au(111) surface underneath the monolayer is still visible as shown in the STM images. Thus, it was found that the molecular rows (as defined with black arrows in the STM images) of the dense phase were aligned along the symmetric <1$\bar{1}$0> direction of the substrate, which were also determined by the herringbone structure of the Au(111). There were three rotational domains, which were rotated by 120° from each other. The molecular arrangements and the sizes of the unit cells of the dense phases of picene and DNTT are apparently similar to the (110) planes of their single crystals (as illustrated in Figure 4.9(a) and (b), respectively), although they are not identical. We should note here, this kind of bulklike monolayer has not been observed in other kind of small organic semiconductors, such as pentacene, to our knowledge. The formation of this type of characteristic monolayer seems to be common for phenacene or thienoacene, with enhanced intermolecular interaction[55,56].

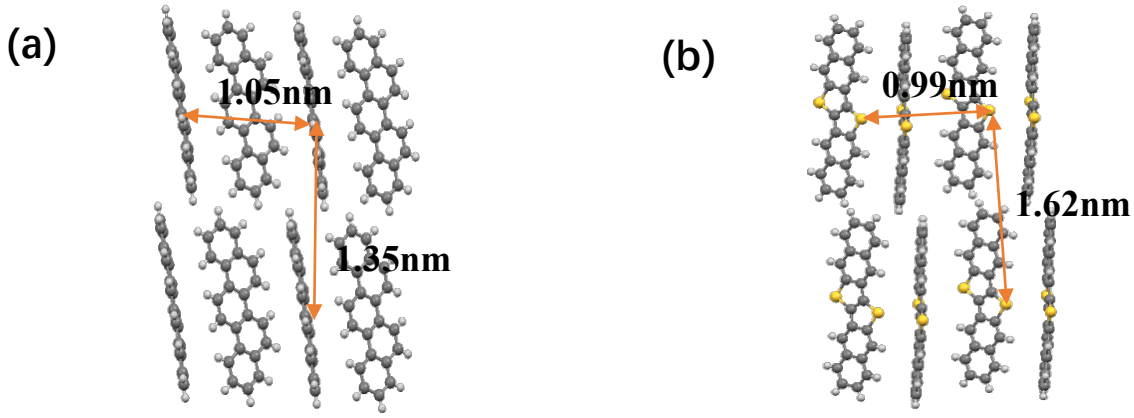

Figure 4.9 (a) (b) (110) planes of picene and DNTT single crystals, respectively. Their unit cell was also shown in the images.

4.3.2 Electronic Structure of Picene and DNTT Monolayers

Upon the phase transition from loose coverage to dense coverage, the evolution of valence band was checked by UPS (Figure 4.10)[14]. The x-axis shows the binding energy; the y-axis shows the density of the photoelectrons. Blue curves represent the UPS spectra of loose phase with loose coverage, which shows the HOMO position at 1.8 eV for picene and 1.9 eV for DNTT as marked by short black line in the images. Then, the HOMO peak of these two molecules splits into more features at the dense phase with bulklike molecular arrangement as observed by the red curves in the UPS spectra. The splitting of HOMO level is very sensitive to slight changes in the molecular packing, or the $\pi - \pi$ stacking distance[57]. This splitting reaction of HOMO peak has not been seen in the polycrystalline film, but it is similar to that expected for single crystal. Therefore, this kind of well-ordered bulk like monolayer is suggested to have a stronger intermolecular interaction with a substantial overlap of the HOMO.

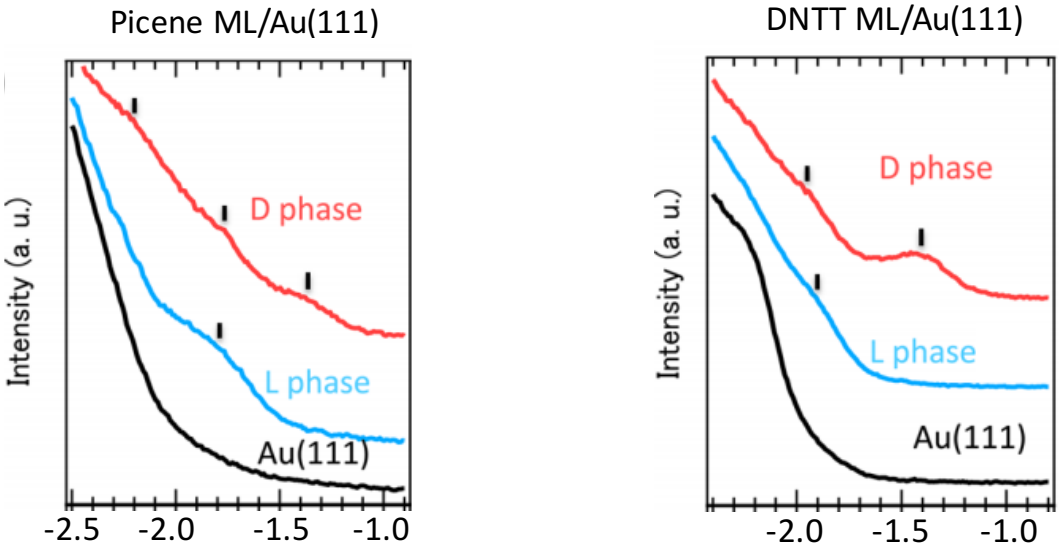

Figure 4.10. UPS spectra of picene and DNTT monolayers with loose phase (L phase) and dense phase (D phase).

4.4 Picene and DNTT Thin Films on Au(111)

4.4.1 Morphology of Picene and DNTT Thin Films

The dense monolayers of picene and DNTT with bulk-like molecular arrangement as discussed above are promising for enhanced stacking of further molecules in a similar fashion. Therefore, we further deposited the multilayer of picene onto the dense monolayer and observed an abrupt growth of large and straight islands of the multilayer. These islands became so large that they could be clearly seen even with an optical microscope (OM). The OM images of the surface with loose and dense coverage of the picene islands prepared with the slow deposition of approximately 20 and 70 ML of picene molecules on the dense monolayer, are shown in Figure 4.11(a) and (b), respectively. In the image of the 20 ML coverage, Figure 4.11(a), the formation of the

rod-like picene crystalline islands with sharp edges are seen. The typical length, width and height of the rod are approximately 30 μm, 0.5 μm and 150 nm, respectively. It was clearly observed that the rods tend to align along three particular directions. The three directions, marked with arrows in Figure 4.11(a), were found to correspond to the three domains of molecular rows of the monolayer on the Au (111) substrate, i.e., the $<1\bar{1}0>$ direction. With increasing the coverage of molecules, as shown in Figure 4.11(b), large-scale crystalline islands with a length of much more than 100 μm were obtained. At the same time, the domain with the aligned islands became as large as 0.5 mm.

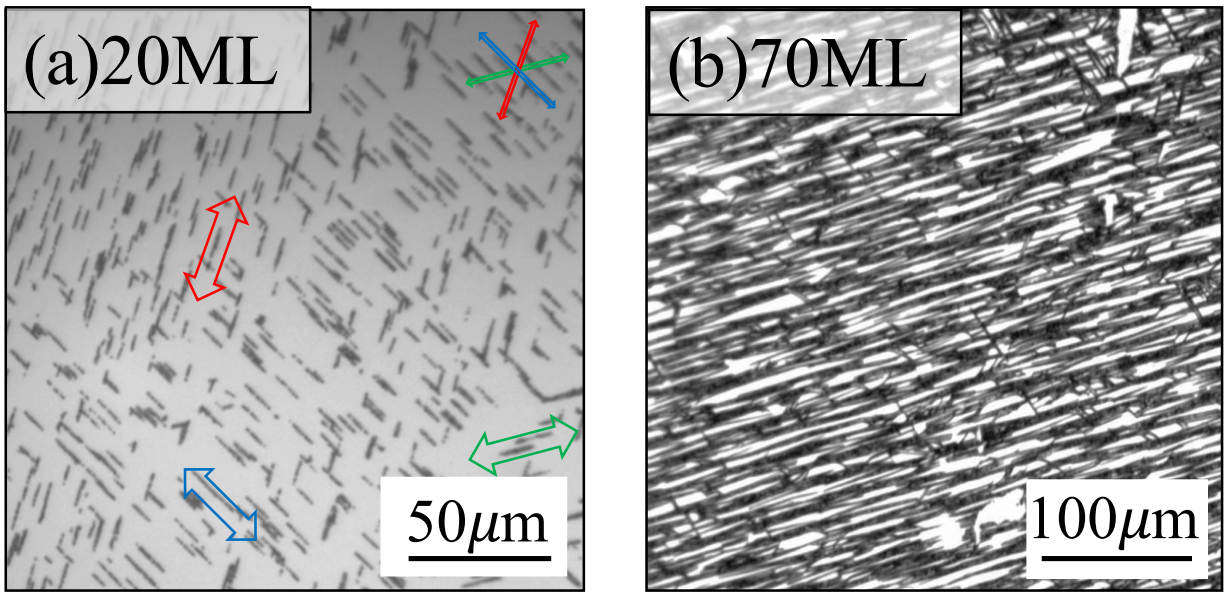

Figure 4.11 (a) Optical microscopy image of picene thin film with the coverage of 20ML; (b) Optical microscopy image of picene thin film with the coverage of 70ML.

Figure 4.12(a) shows the topography of picene crystal island of 70 ML. The width and height of the straight island are approximately 0.5 μm and 300 nm as indicated by Figure 4.12(b). Figure 4.13(a) shows the AFM topography of the top surface of the crystalline picene island, where a step-terrace-like structure was observed. However, most of the steps were with a height of more than 5 nm, as shown in the line scan A in Figure 4.13(b), much larger than a single molecular step, possibly due to bunching of the steps. In addition, the terrace morphology was found to be corrugated with amplitude of several nm as shown in the line scan B in Figure 4.13(b). It is noted that the AFM measurements were conducted after taking the sample out to the atmospheric environment from a UHV, therefore, some distortion of the crystal surface, such as dewetting or disordering due to water coadsorption, may have occurred in this process. We note here that the structure of the monolayer was not changed with increasing the coverage of the molecule. Therefore, crystalline islands seem to form directly on the monolayer without wetting layer.

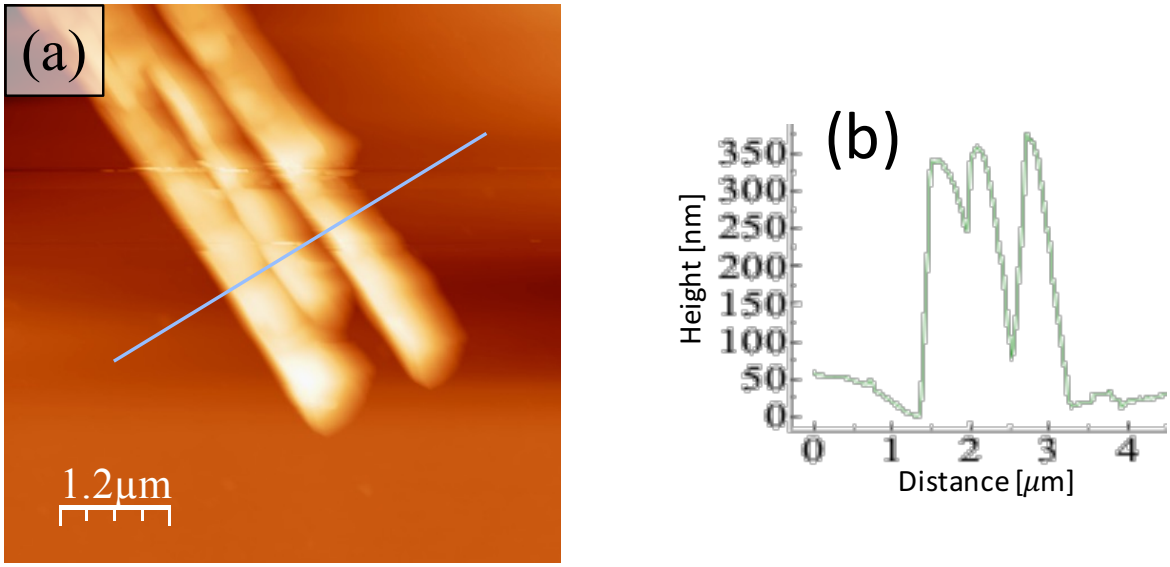

Figure 4.12 (a) AFM image of morphology of picene crystalline island; (b) Height profile corresponding to the scanning line in the AFM image.

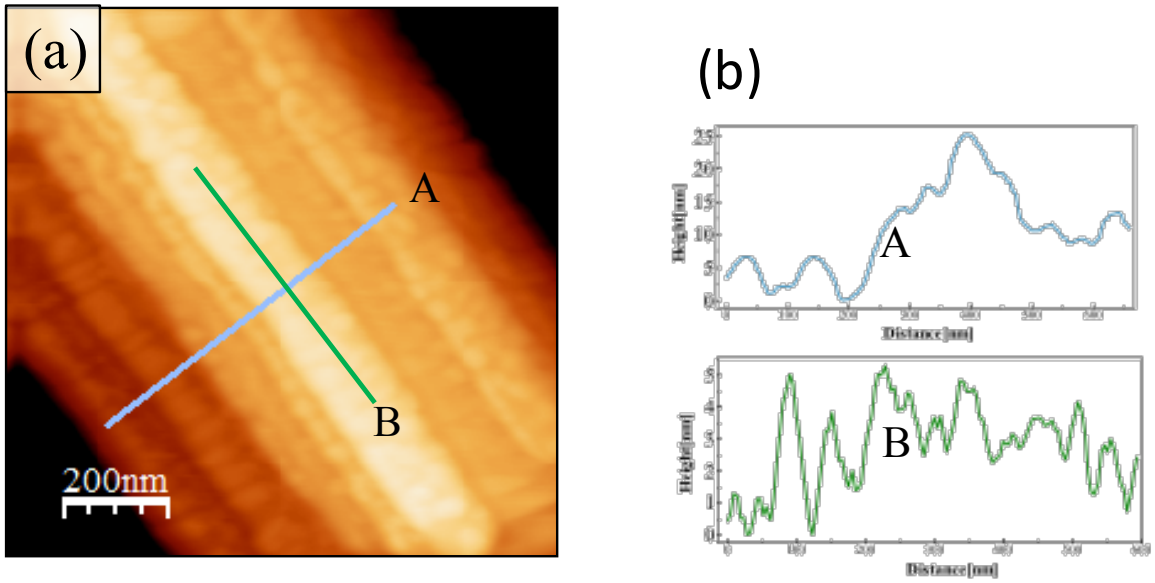

Figure 4.13 (a) AFM image of topography of top surface of picene crystalline island; (b) Height profiles corresponding to the scanning lines in the AFM image.

We also examined the thicker film of DNTT on its bulk-like monolayer. Figure 4.14(a) shows the OM image of DNTT thin film with the molecular coverage of 30 ML. Although we observed formation of the similar islands with the height of 130 nm (as shown in the line scan in Figure 4.15 (a) and (b)) as in the case of picene, the size of them were relatively smaller and the tendency of the alignment of the islands with respect

to the substrate was also weaker. In the higher coverage of 70 ML, as shown in Figure 4.14(b), we found a network structure of the island with typical length of several μm, which was distinct from the case of the high-coverage picene (Figure 4.11(b)). From the AFM image shown in Figure 4.15(a), the surface of DNTT crystal island is rather rough. These results are consistent with the recent work of Dreher et al[16].

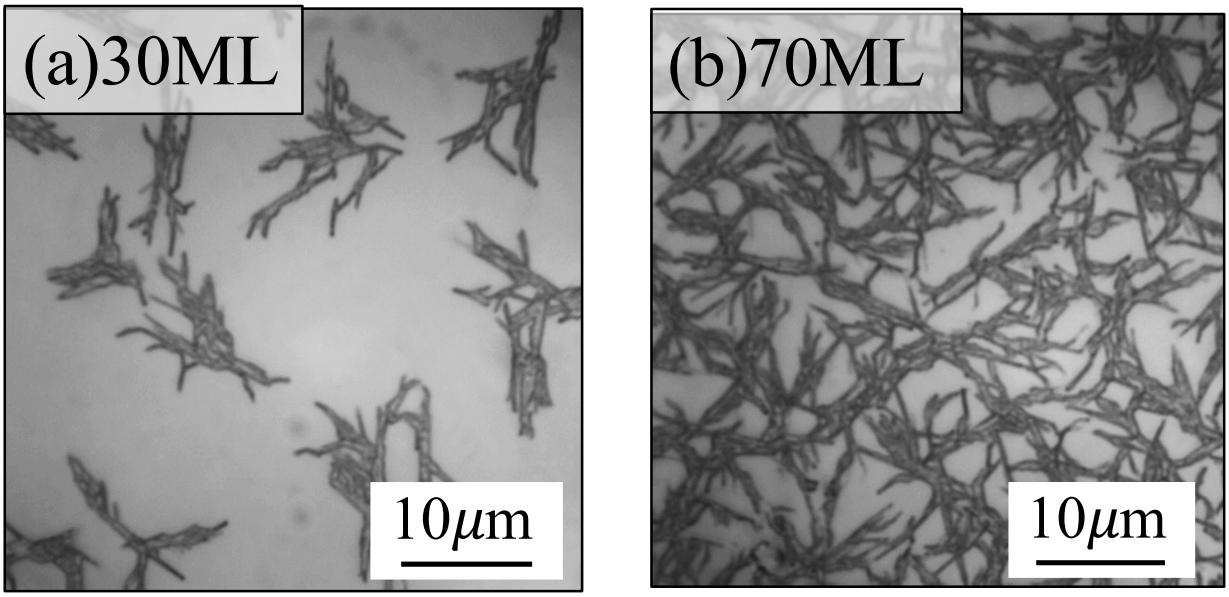

Figure 4.14 (a) Optical microscopy image of DNTT thin film with the coverage of 30ML; (b) Optical microscopy image of DNTT thin film with the coverage of 70ML.

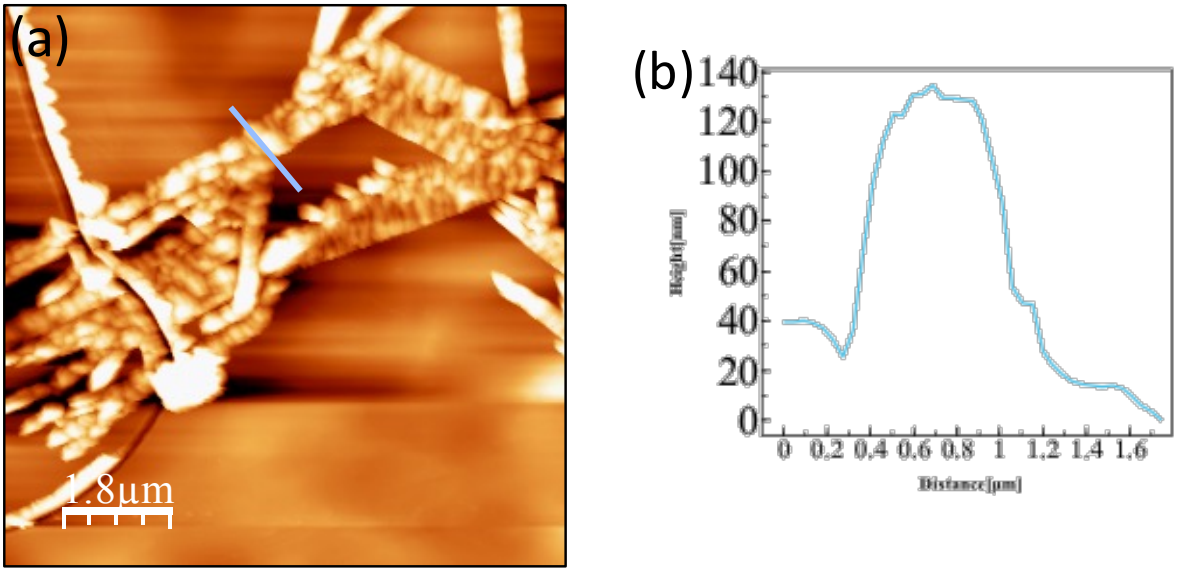

Figure 4.15 (a) AFM image of morphology of DNTT crystalline island; (b) Height profile corresponding to the scanning line in the AFM image.

4.4.2 Molecular Arrangement of Picene and DNTT Thin Tilms

We then analyzed the molecular orientation of crystalline picene film by means of XRD measurements. Figure 4.16(a) displays the spectrum of the θ/2θ-scan without subtraction of the background signal of an Au substrate. Within the analyzed angular range of 5–30°, two obvious diffraction peaks were observed at 2θ=22.1°and 2θ=26.4°. These peaks are assigned to be due to $(20\bar{1})$ and $(21\bar{1})$ planes, respectively, by comparison with the powder spectra (Figure 4.16(b)).

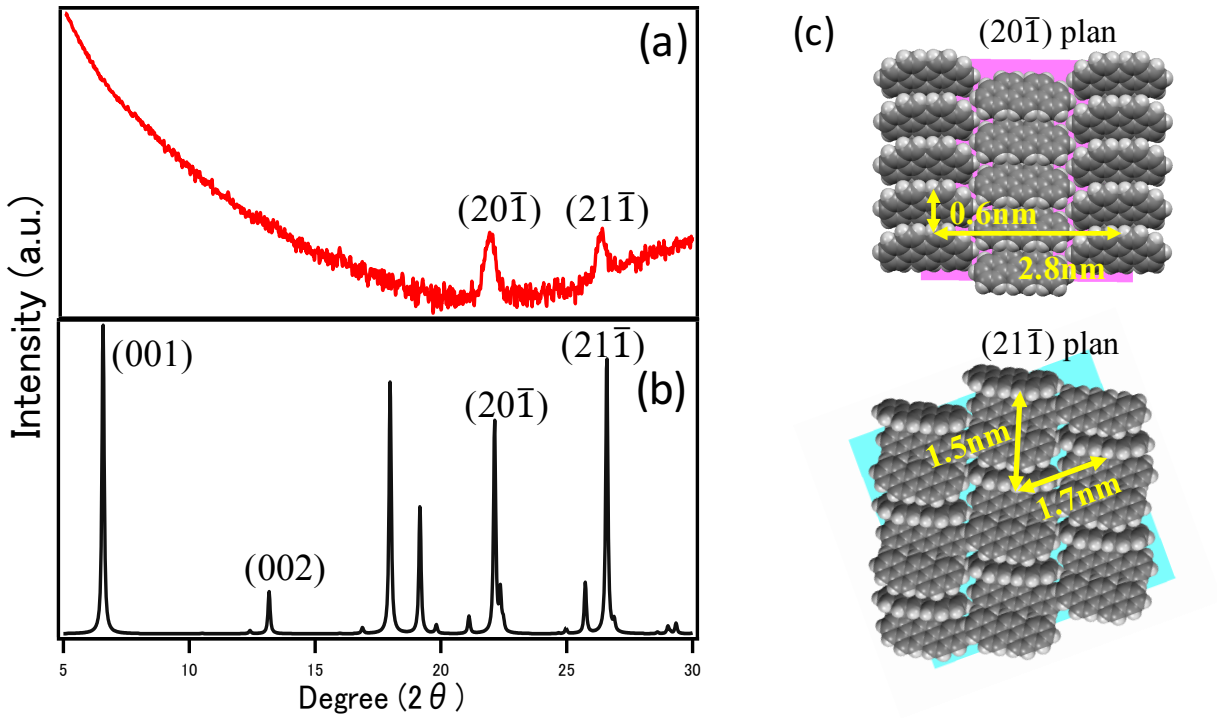

Figure 4.16 (a) XRD spectrum of the picene thin film on Au(111). (b) Calculated spectrum of the picene powder performed by the CCSD software package. (c) Model of molecular arrangements of the $(20\bar{1})$ and $(21\bar{1})$ planes of the bulk picene crystal.

The schematic images of molecular arrangements of the $(20\bar{1})$ and $(21\bar{1})$ planes are illustrated in Figure 4.16(c), which reveals a characteristic orientation of molecules with the long axes parallel to the surface (parallel molecule). Therefore, the monolayer acts as a prestage of the further film growth, resulting in picene crystallites with the $(20\bar{1})$ and $(21\bar{1})$ planes being parallel to the Au(111) surface. Note that the molecular arrangements in the $(20\bar{1})$ and $(21\bar{1})$ planes are not identical to the monolayer as indicate in Figure 4.17. The formation and stabilization of the first monolayer are dominantly driven by a competition between molecule-molecule and molecule-substrate interaction. If the monolayer is well established, molecules have to form a second layer on the top of the organic template provided by the first monolayer. In further consequence, molecule-molecule interactions become more and more dominant, whereas molecule-substrate interactions play a minor role. This implies that, although the bulk-like monolayer can facilitate the further stacking of the

parallel molecules, template effect of the monolayer is not strong enough to realize epitaxial growth of the over layer. In the case of DNTT, as revealed by the work of Dreher et al., DNTT island showed a $(12\bar{1})$ plane in XRD spectrum, which also shows the similar but distinct molecular arrangement from its monolayer. About the clear growth mode of this work, we should note that the details mechanism of the growth has not been yet clarified, we would not discuss here. More researches for this matter are surely required.

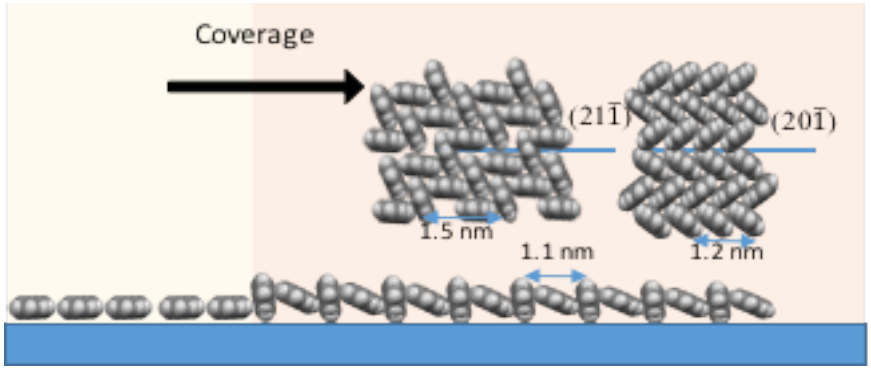

Figure 4.17 Graphical summary of picene thin film formation.

4.5 Calculation of The Force Constant of Intermolecular Van der Waals Force

Although we demonstrated that both picene and DNTT can form the crystalline islands with parallel molecules, that of picene showed higher degree of homogeneity of each island, strict orientation with respect to the substrate and tendency to form larger domain with single orientation of crystalline islands. Although a microscopic understanding of crystallization mechanism is still difficult issue, the different behavior between two molecules may be attributable to the difference in the intermolecular interactions. Therefore, we calculated the force constant of the intermolecular van der Waals force of picene and DNTT.

4.5.1 Calculation by Means of Potential Energy Curve

The intermolecular interaction between picene molecules and DNTT molecules, respectively, were evaluated by means of their potential energy curves. As a most simple model of the molecular configuration, the pair of molecules with the face-to-edge arrangement as shown in Figure 4.18(a) and Figure 4.19(a) were used as picene dimer and DNTT dimer, which are installed with the parameters corresponding to the molecular arrangement in (110) plane of their single crystal. It is noted that the STM images cannot give a detailed molecular arrangement in the bulklike monolayer. Figure 4.18(b) and Figure 4.19(b) show the potential energy curves of picene dimer and DNTT dimer, respectively, versus the center-to-center distance relative to the equilibrium between the monomers. The potential energy curves are obtained by calculating the interaction energy of dimers at different points as one molecule of the dimer moves in the direction of the (110) plan

surface at PM6-D3 method, which is always used for the calculation of molecular weak interactions, by Gaussian 03 program. When the intermolecular distance is less than that of the equilibrium position, the potential energy decreases with increasing the distance between the molecules. After reaching the equilibrium position, the potential energy increases as the distance between molecules increases until the totally separation of the two molecules. Set the potential energy 0 eV at the translation distance of infinity. It should be noted here that the intermolecular distance between two molecules in these two simple models at the equilibrium position were shown to be slightly smaller than that in the single crystals, because there is no interaction with other molecules during the calculation, whereas intermolecular distance of two adjacent molecules in the single crystals is contributed by the interaction with all the surrounding molecules.

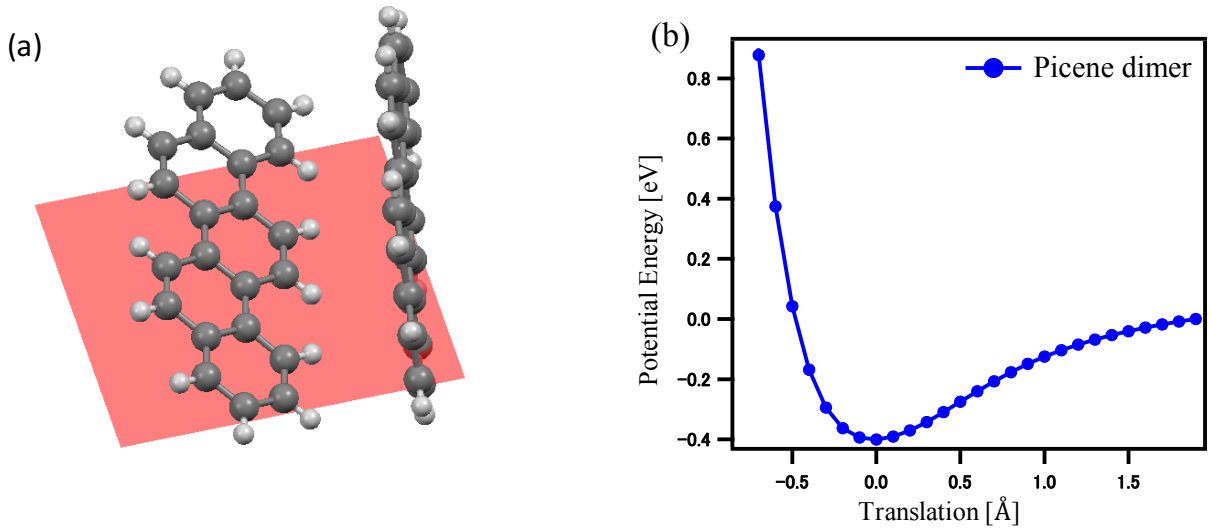

Figure 4.18 (a) The arrangement of picene dimer in the single crystal. The red face indicates the (110) plane picene single crystal. Some parameters about the angles between two monomers of the dimer and the distances between atoms of each monomer were shown in the diagram. (b) Potential energy curve for picene dimer versus the center to center distance between the monomers. Potential energies and translation distance relative to the equilibrium are shown.

It is simply assumed that the simple harmonic oscillation at the position with minimum potential energy. Set the position with minimum potential energy as equilibrium for both the picene dimer and DNTT dimer as shown in Figure 4.20, considering the potential energy for elastic formula

$$U=\frac{1}{2}kx^2 \quad (4.9)$$

where U is potential energy of a spring at a certain position; k is the spring constant; x is distance from equilibrium when the spring is stretched or compressed.

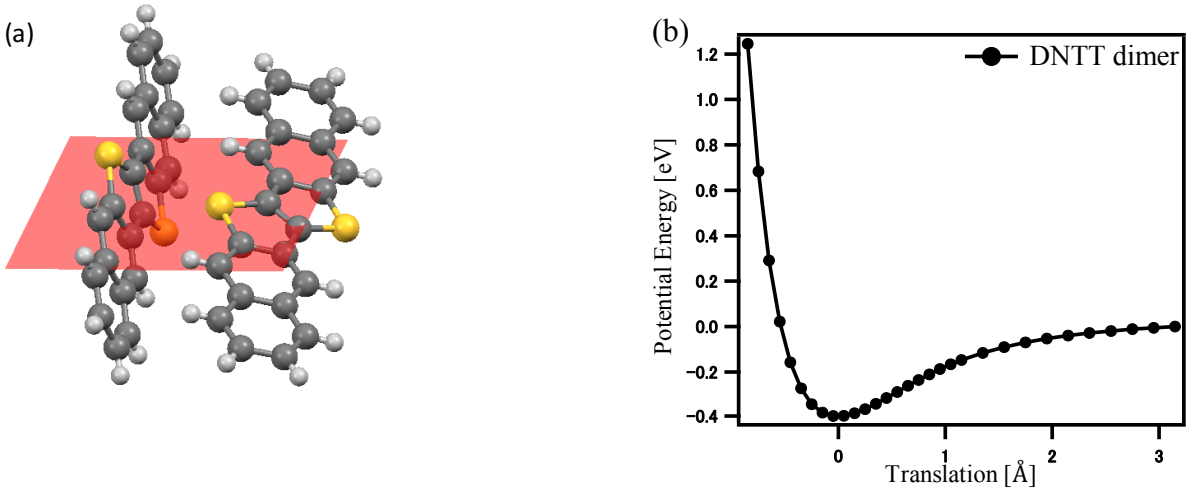

Figure 4.19 (a) The diagram of DNTT dimer in the single crystal. The red face indicates the (110) plane DNTT single crystal. Some parameters about the angles between two monomers of the dimer and the distances between atoms of each monomer were shown. (b) Potential energy curves for DNTT dimer versus the center to center distance between the monomers. Potential energies and translation distance relative to the equilibrium are shown.

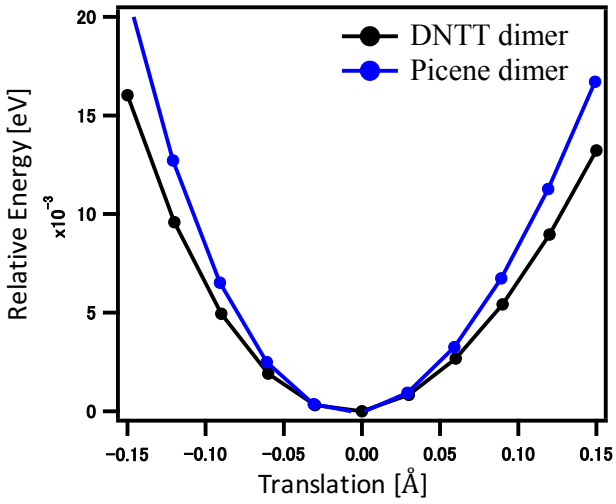

Figure 4.20 Zoom area of the equilibrium position with minimum binding energy of the potential energy curves for both the picene dimer and DNTT dimer. Set the relative energy at the equilibrium position with 0 eV.

After fitting equations near the equilibrium for potential energy curves of picene and DNTT in Figure 4.20, we can simply deduce the force constant of the intermolecular van der Waals bonding along the π-stacking direction of two adjacent molecules in the (110) plane of the single crystal of 26.27 kg/s^2 for picene and 21.64 kg/s^2 for DNTT. Thus, the π-π interaction in picene is found to be stronger than that of DNTT,

possibly resulting in the better crystalline morphology of the multilayer. However, since the molecular growth can depend on many other parameters, further detailed examination will be required.

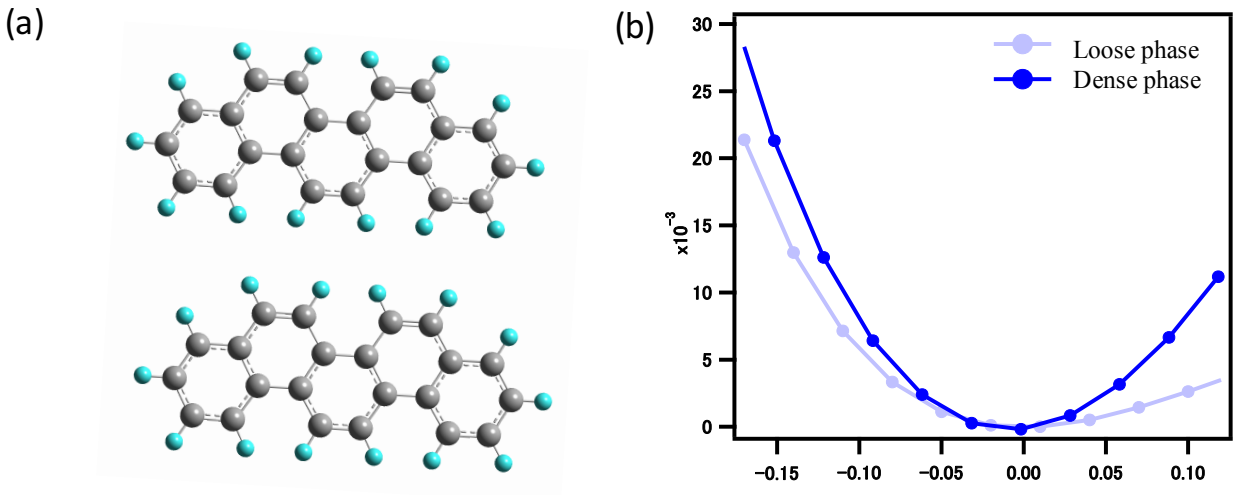

Figure 4.21 (a) The diagram of picene dimer with flat-lying configuration in the loose phase of picene monolayer; (b) Zoom area of the equilibrium position with minimum binding energy of the potential energy curves for picene dimer with the flat-lying configuration in loose phase of monolayer and picene dimer with bulklike configuration in dense phase of monolayer, respectively.

The intermolecular interaction between picene molecules and DNTT molecules in the loose phase monolayer, which shows the “flat-lying” configuration as discussed in section 4.3.1, were also evaluated using the same method. Figure 4.22(a) shows the simple model of the molecular configuration of picene dimer in the loose phase of monolayer, which shows the flat-lying and parallel molecular arrangement. After fitting equation for the potential energy curve of picene dimer in loose phase (Figure 4.21(b)), deducing the force constant of the intermolecular van der Waals force of 10.27 kg/s^2, which is smaller than that of picene dimer in dense phase as discussed above (26.27 kg/s^2) as shown in Table 4.1. As for the case of DNTT, Figure 4.23(a) shows the diagram of DNTT dimer in the loose phase of monolayer. From the fitting equation for the potential energy curve of DNTT dimer in loose phase (Figure 4.22(b)), the force constant of the intermolecular van der Waals force can be get easily to be the value of 1.7 kg/s^2, which is also smaller than that of DNTT dimer in dense phase as discussed above (21.64 kg/s^2). And the minimum potential energy of bulk dimer of both picene and DNTT shows the smaller value than that of flat-lying dimers as summarized in Table 4.1. Therefore, this phenomenon can also indicate the stronger intermolecular interaction of peculiar bulklike monolayer than the normal monolayer consists of only “flat-lying” molecules. It is noted that, the similar straight island structure of pentacene and quaterphenyl thin films were previously found on the metal substrate[17,24]. However, the size of the islands is much smaller than the case of picene or DNTT. This difference is attributable to the difference in the structure of the monolayer, i.e., monolayer of pentacene consists of "flat-lying" molecules, in contrast

to the case of molecules examined in the present study. The characteristic shape of monolayer with a bulk-like molecular arrangement can therefore considered to stabilize the upper layer with the parallel molecules.

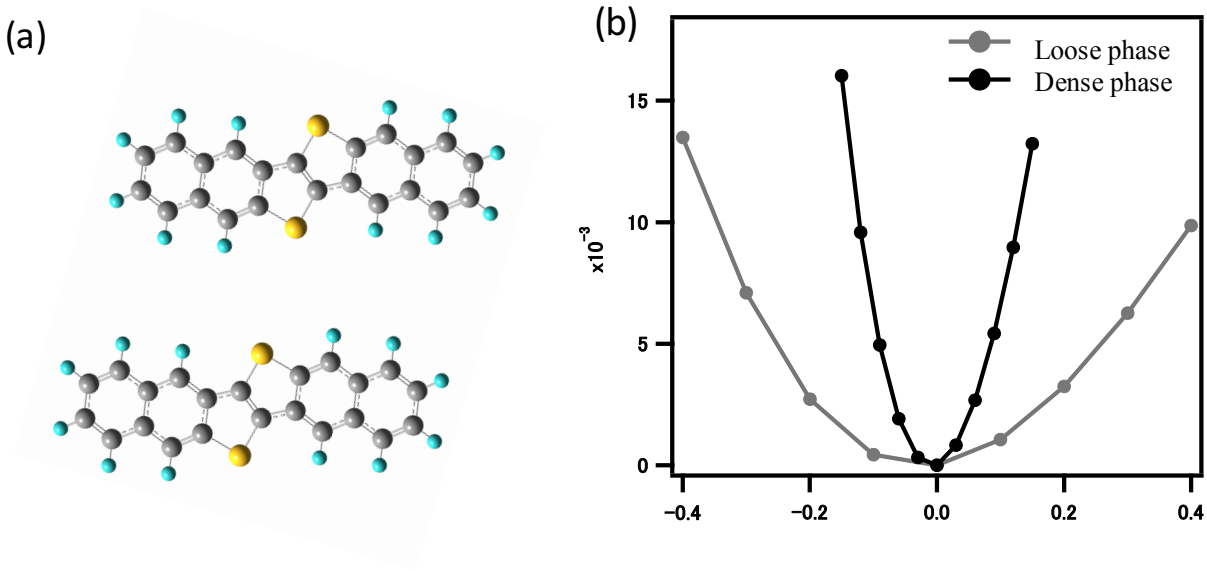

Figure 4.22 (a) The diagram of DNTT dimer with flat-lying configuration in the loose phase of monolayer; (b) Zoom area of the equilibrium position with minimum binding energy of the potential energy curves for DNTT dimer with flat-lying configuration in loose phase of monolayer and DNTT dimer with bulklike configuration in dense phase of monolayer, respectively.

Table 4.1 Calculated results of picene and DNTT dimers

	Picene		DNTT	
	Bulk dimer	Flat-lying dimer	Bulk dimer	Flat-lying dimer
	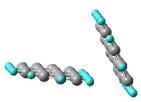	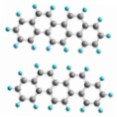	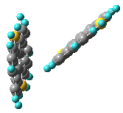	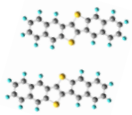
Minimum potential energy (eV)	-0.4	-0.1	-0.39	-0.08
Force constant ($kg/s^{2)}$	26.27	10.27	21.64	1.7

4.5.2 Calculation by Means of Vibration Energy

As the measure of the intermolecular force constant, we also examined the vibrational energy of the translational modes with the molecular displacement in the direction of the van der Waals bonding, in the case of the single crystalline picene and DNTT. The normal vibrational modes were calculated from the dynamical

matrix constructed by the force field MMFF94s using CONFLEX [22]. Figure 4.23 shows translational optic phonon modes at the Γ point, in which the displacements of atoms (indicated by red arrows) are mainly along the π-stacking direction of two adjacent molecules in the a-b plane of the single crystal. The vibrational energies of such modes in the case of picene and DNTT were found to be 10.61 meV and 8.638 meV, respectively, as indicated in the figure.

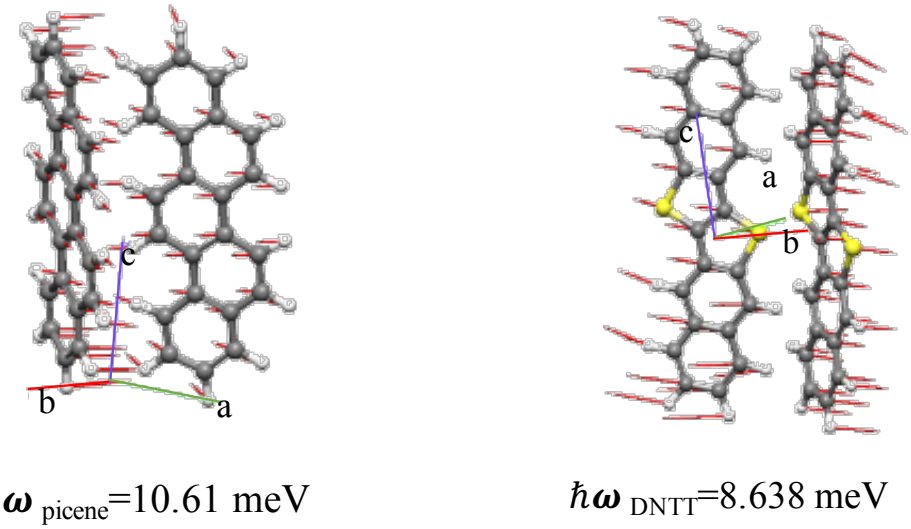

Figure 4.23 (a) Molecular vibration modes in the parallel ab plane of the picene dimer of its bulk phase unit cell. (b) Molecular vibration modes in the parallel ab plane of the DNTT dimer of its bulk phase unit cell. The parameters below the figures indicate their corresponding vibrational energy.

Since we have two molecules in each unit cell, now we consider a lattice vibration with one-dimensional chain where two different atoms with masses M and m alternate, which are interacting with their nearest neighbors via a potential V (x), which has a minimum at the equilibrium position. We consider a dynamical behavior for small displacements $na+u_n$ of the individual atoms, where a is the distance between two atoms, the period of the diatomic system is 2a. The position of two atoms which is labeled by index n are given by $x_n^1=2na+u_{2n}$ for atom 1 and $x_n^2=2na+a+u_{2n+1}$ for atom 2. Therefore, only considering the elastic interaction between nearest neighbor atoms, motion equation of the n diatoms is

$$M\frac{d^2u_{2n}}{d_{t^2}}=k(u_{2n+1}+u_{2n-1}-2u_{2n}) \quad (4.1)$$

$$m\frac{d^2u_{2n+1}}{d_{t^2}}=k(u_{2n}+u_{2n+2}-2u_{2n+1}) \quad (4.2)$$

where k is the force constant.

The Ansatz

$$u_{2n}=Ae^{i(\omega t-2naq)} \text{ and } u_{2n+1}=Be^{i[\omega t-(2n+1)aq)} \quad (4.3)$$

provides a matrix equation

$$-\omega^2 \begin{pmatrix} M & 0 \\ 0 & m \end{pmatrix} \begin{pmatrix} A \\ B \end{pmatrix} = k \begin{pmatrix} -2 & 2\cos(aq) \\ 2\cos(aq) & -2 \end{pmatrix} \begin{pmatrix} A \\ B \end{pmatrix} \quad (4.4)$$

The existence of nontrivial solutions provides the condition

$$\begin{vmatrix} M\omega^2 - 2k & 2kcos(aq) \\ 2kcos(aq) & m\omega^2 - 2k \end{vmatrix} = 0 \quad (4.5)$$

with the solutions

$$\omega_{\pm}^2 = \frac{k}{Mm}\left[(M+m) \pm \sqrt{(M+m)^2 - 4Mmsin^2aq}\right] = \frac{k(M+m)}{Mm}\left(1 \pm \sqrt{1 - \frac{4Mm}{(M+m)^2}sin^2aq}\right) \quad (4.6)$$

These are plotted in Figure 4.24, which displays two branches.

For the lower branch (acoustic branch) we have $\omega = 0$ at the Γ point and A=B, indicating both atoms within the unit cell moves in the same direction. For the upper branch (optical branch), we got

$$\omega = \sqrt{2k\frac{M+m}{Mm}} \quad (4.7)$$

and

$$M \cdot A = -m \cdot B \quad (4.8)$$

which indicating the two atoms in each unit cell move against each other. The difference between the two patterns is that the optical branch is written in the original cell tracing the vibration model of relative movement between two atoms. Therefore, in our case, from the energy of the vibrational modes and masses of the molecule (picene: 2.78 $\times 10^{-1}$ kg /mol, DNTT:3.40$\times 10^{-1}$ kg /mol), we estimated the force constant of the intermolecular van der Waals bonding, simply assuming the harmonic oscillation using the optical branch, deducing 30.1 kg/s^2 for picene and 24.3 kg/s^2 for DNTT along parallel ab plane, which is consistent with the result calculated from potential energy curves. This shows that the simplified method as we discussed in section 4.5.1 in this work is feasible for the evaluation of the intermolecular interaction. Even though the force constants of the intermolecular van der Waals force obtained from the calculation by means of potential energy curves for picene and DNTT dimers are slightly smaller than the values obtained from the vibration energy of the translational modes of two molecules in the single crystal along the same binding direction. This can be explained by the fact that the latter results include the interactions with other molecules in the crystal. Whereas, in the former simplified case, we only considered the interactions of the two molecules within the dimers.

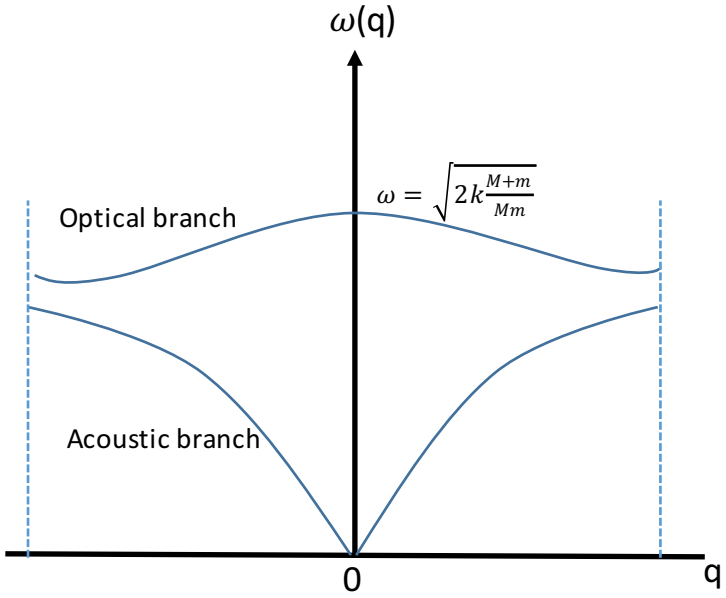

Figure 4.24 Vibrational spectrum for the diatomic chain with the masses M and m.

4.6 Summary

Well-defined crystalline films of picene and DNTT on their well-ordered monolayers with a bulklike molecular arrangement were fabricated. By means of slow deposition of the multilayer on the bulklike monolayer, large-scale crystalline islands having lengths of several hundred micrometers were obtained, especially in the case of picene. XRD measurement revealed that picene crystals consist of planes of $(20\bar{1})$ and $(21\bar{1})$, clearly suggesting that the film consists of the parallel molecules which may be stabilized by the peculiar structure of the monolayer. The force constant of van der Walls force of picene and DNTT were also calculated by means of a kind of simplified calculation methods, which can examine the intermolecular interaction of picene than DNTT. The superior growth in picene films may be attributed to the stronger intermolecular force constant.

Chapter 5

Morphology and Electronic Structure of Peculiar Sumanene Monolayers and Fabrication of Sumanene Thin Films

5.1 Introduction

Modification of surfaces with bowl-shaped hydrocarbons, which is always called buckybowls, have attracted much interest because their pronounced difference of chemical ability between the concave side and convex side, large dipole moment and shape complementarity[60]. Two-dimensional self-assembly of buckybowls at surfaces have shown some peculiar phenomenon like bowl-in-bowl complexation[61,62] and pentagonal molecular tiling[63–67]. However, no well-defined periodic bowl-in-bowl stacking molecular arrangement, which is expected to have efficient intermolecular interaction, has been realized until now.

Sumanene, a kind of buckybowl that exhibits a concave-convex geometry, is characterized by a C_{3v}-symmetric fragment of C_{60} fullerenes. Following the successful synthesis of sumanene by Sakurai et al. in 2003 [68], the characteristic and structural features of sumanene have already been reported[26,29,69,70]. Studies have shown that the bowl shaped geometry of sumanene can enhances the adsorption of molecules such as, CO, CO_2 and NH_3[71], especially the adsorption of H_2, which can be employed in developing efficient hydrogen storage systems[25,72]. A clear energetic preference for atoms or molecules, such as K, methane and C_{60}, binding to the concave face of sumanene as an efficient host-guest complex was reported[72,73]. The curved binding surfaces of sumanene can also improve the intermolecular π-π coupling, hence improve the intermolecular electron transport. Indeed, in the crystal of sumanene, it assembles a one-dimensional (1D) bowl-stack column through a concave-convex interaction, where every column is presented in the same direction[26]. The minimum estimate of the intra-columnar electron mobility of sumanene single crystal along the bowl-stacking direction was calculated to be 0.75 $cm^2V^{-1}s^{-1}$[27], which is comparable to a C_{60} single crystal (0.5 $cm^2V^{-1}s^{-1}$)[28]. However, a much smaller electron mobility with the value of 4.9×10^{-3} $cm^2V^{-1}s^{-1}$ was exhibited along the perpendicular direction to the bowl-stacking axis. Recently, unique thermal property of sumanene, where the heat transport is dominant along the perpendicular direction to the stacked column of sumanene crystal, was investigated[29]. Therefore, these excellent properties of sumanene make it an attractive and promising candidate for the application in organic electronics

The surface-adsorbed sumanene on Ag(111) with bowl-up and bowl-down conformations have been observed so far[73]. In 2016, Fujii and coworkers have demonstrated that the bowl inversion of sumanene monolayer on Au(111) surface can be actively driven by external force[74]. Their results strongly suggest the

possibility of application in the molecular-scale memory devices if the bowl-up and bowl-down state in interpreted as different signals. Since the control of the molecular arrangement at the interface between aromatic organic molecules and surfaces affects the electronic, optical and thermoelectric properties of sumanene thin films, it is necessary to have reasonable design of the molecular packing and to explore the electronic structures obtained from the interface of sumanene and substrates.

In this chapter, sumanene monolayer with one-dimensional bowl-stacking arrangement, which may have the enhanced and stabilized convex-concave intermolecular coupling, was realized on Cu(111) surface. We clarified the electronic structure of both the bowl-stacking arrangement of sumanene monolayer on Cu(111) and bowl-up and bowl-down alternate arrangement of sumanene monolayer on Ag(111)/Au(111) by UPS, XPS and ARPES. The results suggest that enhanced carrier mobility along the bowl-stacking molecular direction of sumanene monolayer on Cu(111) can be expected. Furthermore, sumanene thin films based on these two kinds of peculiar monolayers were fabricated. The superior growth of sumanene thin film with tilted molecular arrangement on Cu(111) may due to the stronger intermolecular interaction along the bowl-stacking direction in monolayer, which can stabilized the further molecules.

5.2 Experiment

5.2.1 Experimental Method

Noble single crystalline Au(111), Cu(111) and Ag(111) were used as substrates in this works. All the substrates were cleaned by several cycles of Ar^+ ion sputtering followed by annealing. The cleanliness of the substrates was examined by low-energy electron diffraction (LEED) and scanning tunneling microscopy (STM) with constant current mode. All the fabrication progress of monolayers and thin films was operated in an ultra-high vacuum (UHV) environment. Morphology of the thin film was observed by atomic force microscopy (AFM) and optical microscope (OM). Crystallographic phase and molecular orientation in the films were characterized by XRD measurement.

Electronic structure of monolayers was checked by synchrotron photoemission. UPS and ARPES were conducted at the BL-2B of UVSOR and XPS was done at BL-13B of Photon Factory.

5.2.2 Calculation Method

Density functional theory (DFT) calculations were performed with Gaussian code in this part. We first optimize molecular structure of sumanene molecule with the DFT/6-311+G basis set. Simple model with only a pair of molecules of the molecular configuration were used in this work. The configuration of each dimer was optimized with the corresponding experimental parameters. Dimerscan with respect to the separation of two molecules of the dimer was performed with the calculation of the intermolecular interaction energy every several Å with the PM6-D3 method in this work. In the separation process the orientation and structure of monomers keep fixed.

5.3 Morphology of Sumanene Monolayer on Metal Surfaces

5.3.1 Bowl-stacking Arrangement of Sumanene Monolayer on Cu(111)

In this work, the adsorption of bowl-stacking sumanene on the Cu(111) surface has been observed by means of scanning tunneling microscopy (STM). In the below wide-area STM image (Figure 5.1(a)), clear one-dimensional structure can be seen. The STM image shows two rotational domains distributed at different terrace, which can be distinguished by the difference in light and dark caused by step height difference. There are totally three rotational domains (not shown here), which show 120 degrees from each other, because of the three rotational symmetry of the Cu(111) substrate.

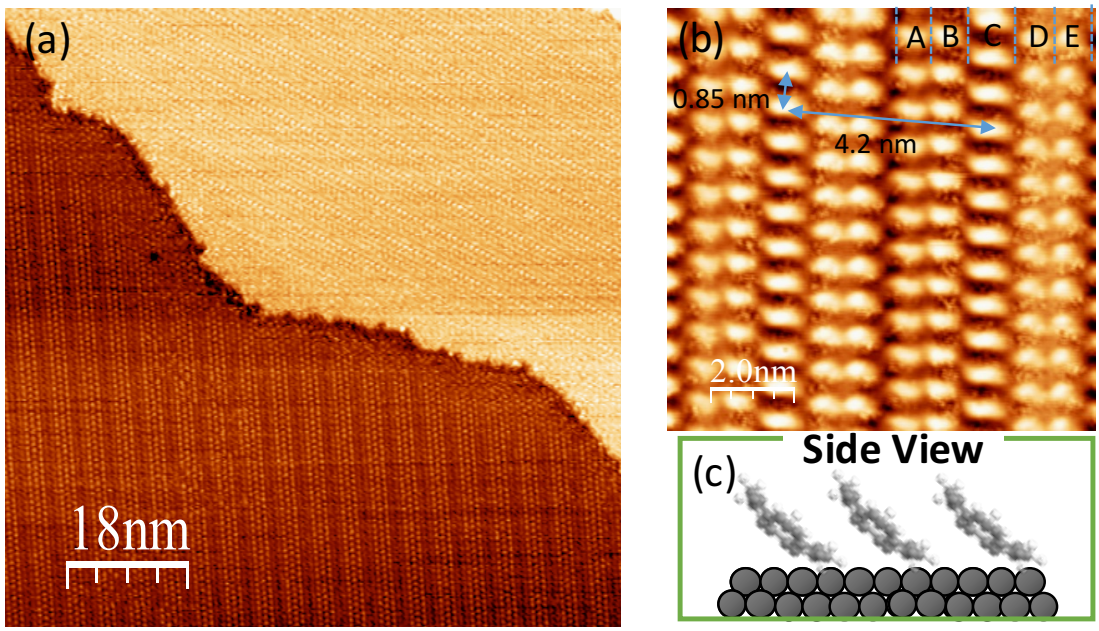

Figure 5.1 (a) STM image of wide-area five-rows periodic structure of sumanene monolayer on Cu(111); (b) Enlarged image of five-rows periodic structure; (c) One possible side view of single molecular row of monolayer.

The detail of molecular arrangement of sumanene monolayer on Cu(111) is shown in the enlarged STM image (Figure 5.1(b)). The formation of five-rows periodic structure marked from A to E was found. The size of each kind of complex ellipse spot of five-rows periodic structure in the STM image is about 1 nm, which is same as the diameter of sumanene molecule. Therefore, it is believed that one ellipse spot corresponds to one sumanene molecule. The elongated shape of sumanene molecule is not like the round shape of sumanene of monolayer on Ag(111) as shown in Figure 5.4. As shown in Figure 5.1(b), a depression of sumanene molecules, most of which were found not in the center of the molecules, can be observed in the STM image. This appearance indicates that the sumanene molecules did not adsorbed parallel to the substrate, hence, dominating

such a STM contrast of one single molecule. Whereas, sumanene molecules are tilted adsorbed on the surface with the rim on the top side, possibly forming a bowl-stacking arrangement with π- π binding as shown in the diagram of side view in Figure 5.1(c). According to the different bright and dark STM contrast of five-rows periodic structure in the STM image, it can be expected that the slope of molecules relative to the substrate is different. Slope angle of molecular rows D and E are similar with that of molecular row A. Slope angle of molecular rows B and C, which show brighter STM contrast, seems larger. Therefore, sumanene molecules of each molecular row of the five-rows periodic structure takes different adsorption angle and adsorption site as suggested in the diagram of Figure 5.2(b), where The C-H···π binding motif between the rim and the benzene ring of sumanene molecules of nearby molecular rows is also clearly indicated[75]. In spite of this, all the molecular rows assemble the bowl-stacking arrangement, which indicate more efficient π interaction between sumanene molecules than that of flat-lying arrangement on Au(111) and Ag(111). As a result, the unit cell of this one-dimensional bowl-stacking arrangement was very large, with the unit cell being approximately 0.85 nm along the column direction and 4.2 nm across the column direction as shown in Figure 5.1(b).

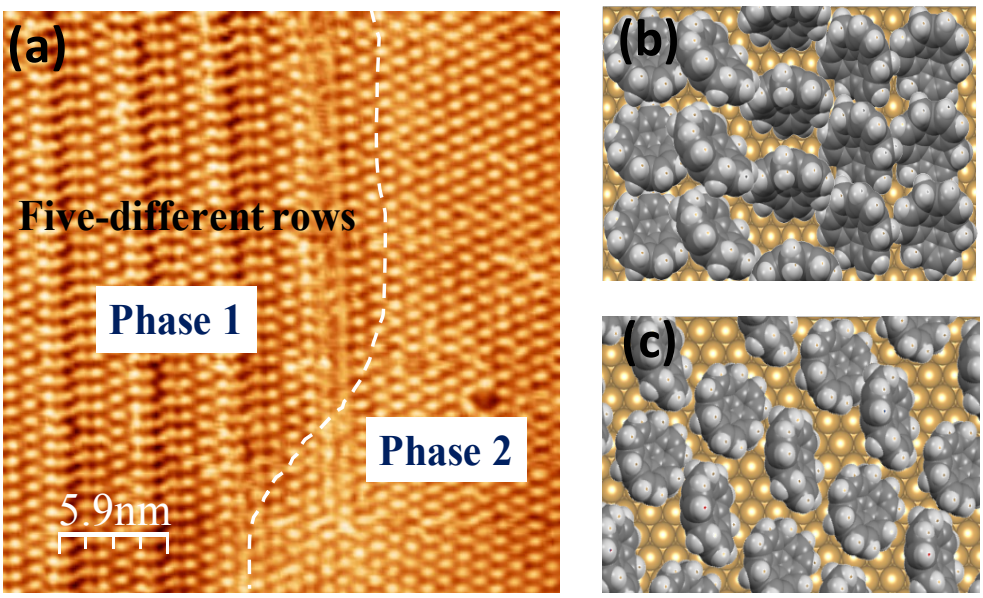

Figure 5.2 (a)STM image of sumanene monolayer on Cu(111)with both phase 1 and phase 2; (b)Diagram of molecular arrangement of phase1; (c) Diagram of molecular arrangement of phase 2.

At the terminal area of the five-rows periodic structure (phase 1) another phase (phase 2) with different molecular arrangement was also observed by STM measurement as shown in Figure 5.2 (a). Figure 5.3 (a) shows the enlarged STM image of phase 2 with the unit cell of 1.2×1.4 nm^2. Two kinds of elongated shape of the sumanene molecules of two adjacent molecular rows indicate that phase 2 consists of two kinds of different tilted sumanene molecules, which can be also shown by the height difference of the molecules with the average height of 7 Å in row A and average height of 8 Å in row B as shown in Figure 5.3(b). Therefore, phase 2 of sumanene monolayer on Cu(111) shows one-dimensional bowl-stacking sumanene with two-rows periodic arrangement, as shown in the diagram of Figure 5.2(c), was also identified.

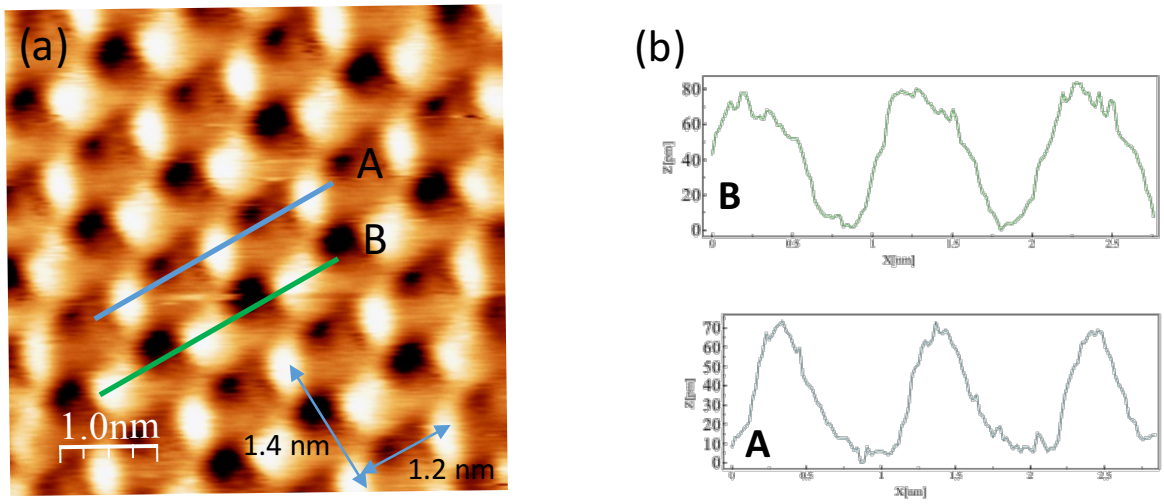

Figure 5.3 (a) Enlarged STM image of phase 2 with two-rows periodic arrangement of the sumanene monolayer on Cu(111) in Figure 5.2(a); (b)Height profiles corresponding to the scanning lines in the STM image.

We should note here, this one-dimensional bowl-stacking structure was stable during STM measurements at RT. The one-dimensional molecular arrangement domains are rather large as shown in Figure 5.1(a). These phenomenon can reflect the strong intermolecular interaction of bowl-stacking sumanene monolayer on Cu(111).

5.3.2 Bowl-up and Bowl-down Arrangement of Sumanene Monolayers on Au(111) and Ag(111)

STM images of sumanene monolayers on Ag(111) and Au(111) are shown in Figure 5.4(a) and (b). Periodic honeycomb and hexagonal patterns are apparent on sumanene monolayers both on Ag(111) and Au(111) as shown in the diagram of Figure 5.4(c). The round shape spots in the STM image with the diameter of about 1.0 nm are corresponds to one sumanene molecule. Height difference between bright and dark molecules is about 1Å as measured by the scanning line in the STM image (Figure 5.4(d)). The difference between bright and dark STM contrasts corresponding to the bowl-up and bowl-down conformation of sumanene molecules, which has been proved theoretically and experimentally[73]. The ratio of bow-up and bowl-down molecules is shown to be 2:1 in this kind of arrangement according to the STM result, arranged in hexagons at intervals of about 1.0 nm. In this structure, sumanene molecules are stabilized by π-π stacking of bowl-up and bowl-down molecules, which has been explained by an inversion during the adsorption process in order to orient the three six-membered rings at the rim of sumanene molecule parallel to the six- membered ring of nearby sumanene.

However, it is difficult to determine more details of adsorption morphology of molecules only by STM measurement at room temperature in our case, such as the different rotational states of sumanene molecules. A presence of three rotational states was expected on Ag(111) and Au(111) from earlier studies[74,76]. However, it shows a randomly rotational orientation at room temperature by STM detection.

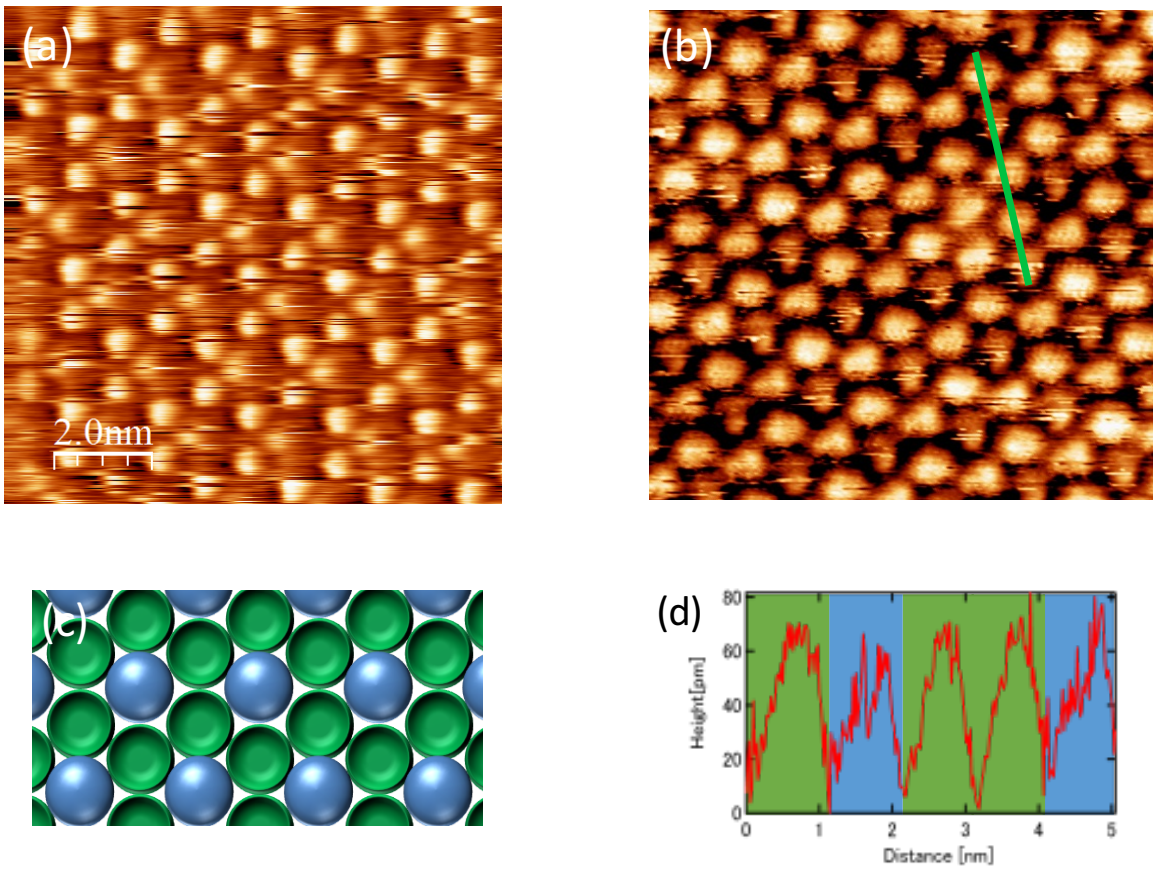

Figure 5.4 (a)(b) STM images of sumanene monolayers on Ag(111) and Au(111), respectively; (c) Diagram of the molecular arrangement; (d) Height profile corresponding to the scanning line in (b). The background color corresponds to the sumanene molecule of the corresponding color in figure (c).

Since we determined the sumanene monolayers on Ag(111) and Au(111) at room temperature. The dynamic inversion was observed during the STM measurement. Most of the molecules exhibit the sudden changes in the molecular height during the scanning, which is shown as the scratches on the molecules as shown in Figure 5.5. Sumanene molecule with bowl-down conformation is characterized by a brighter protrusion at the molecular center[74] (Figure 5.5(b)), and the bowl-up conformation is characterized by a brighter protrusion around the molecular edge(Figure 5.5(a)). At room temperature, the STM-induced bowl inversion lead to bright and dark STM contrast within single molecule as shown in Figure 5.5 both in the case of bowl-up and bowl-down molecules. The initial bowl-up state switches to bowl-down state, and then back to the bowl-up states. Thus, the high frequency flipping between bowl-up and bowl-down cause the bright and dark, which reflect up and down within one single molecule. These scratches should not be caused by noise from external environment, because the noise induced scratches can appear everywhere without the switch between bright and dark STM contrast on a molecule.

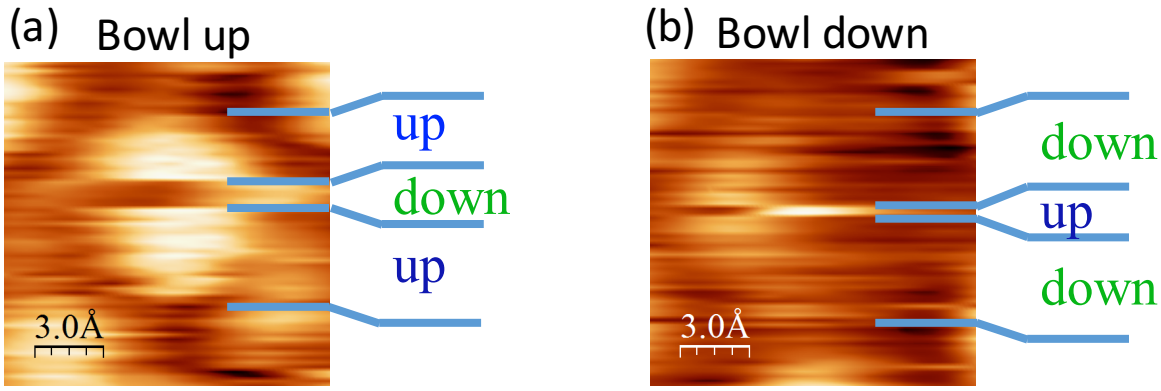

Figure 5.5 (a) STM image of bowl-up molecule; (b) STM image of bowl-down molecule.

The bowl-inversion phenomenon of sumanene molecules has not been reported in low temperature STM measurement. Meanwhile, sumanene molecules in solution also did not show bowl-inversion at room temperature. The activation barrier of bowl inversion has been revealed to be 0.7 eV at interface[74]. However, the room temperature can be regard as only 0.026 eV. Therefore, the bowl-inversion of sumanene molecules on Au(111) and Ag(111) in our case can be considered to be caused by the influences of a combination of temperature, STM probe and interaction between molecules and the substrate.

The effects of such bowl-inversion must be considered in the fabrication of organic semiconductor devices using sumanene, and it is also important to utilize this specific effect actively.

5.4 Electronic Characterization of Sumanene Monolayers

The electronic properties and chemical reactivity of materials are closely related to the behavior of valence electrons near the Fermi level and core level electrons at core level. Thereby, the degree of the overlap of the frontier orbitals of organic molecules plays an important role in determining the film's quality. In order to reveal the electronic structure of both bowl-stacking arrangement and bowl-up-down arrangement of sumanene monolayers, information concerning the occupied states of these two systems were analyzed by means of synchrotron photoemission spectroscopy.

5.4.1 Valence Electronic Structure of Sumanene Monolayer on Cu(111)

- **UPS spectra of sumanene monolayer on Cu(111)**

To reveal the valence electronic structure of the monolayer, we performed UPS measurement. Figure 5.6 represents the density of states near Fermi level of sumanene monolayer on Cu(111) substrate. The x-axis of the spectra represents the binding energy, where the origin of the energy scale is set to the Fermi level. The y-axis of the spectra shows the density of photoelectrons. As shown by the black spectrum, the clean Cu surface has a large state density at binding energy of 2.0 eV due to the strong copper d-band photoemission. The onset can be seen at the left edge of the spectrum. After the deposition of sumanene molecules, a slightly wide small

peak appeared at the binding energy of about 1.4 eV. It can be considered to be the HOMO band position of sumanene monolayer. There is no obvious change of the HOMO peak position with increasing of the molecular amount as shown in the UPS spectra. We should note that the broad peak of HOMO band may be caused by the sumanene molecules at five different stacking rows.

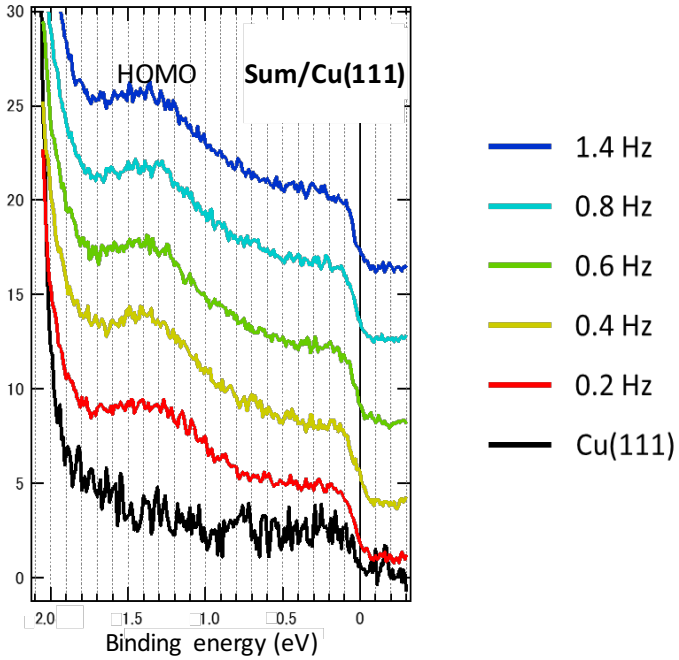

Figure 5.6 UPS spectra of sumanene monolayers with different coverage on Cu(111).

- **Work function of sumanene monolayer on Cu(111)**

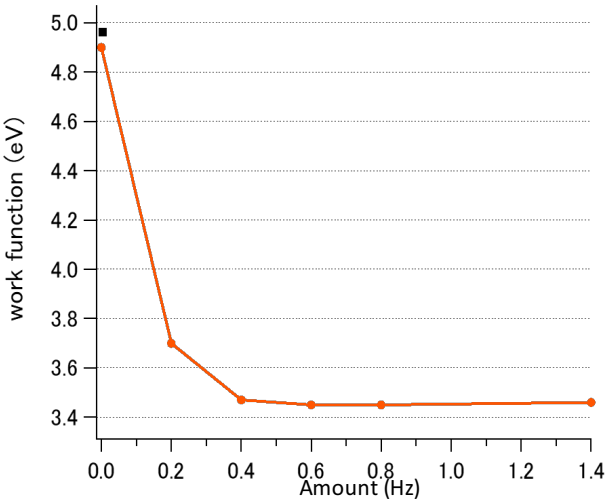

Figure 5.7 Work function of sumanene monolayer on Cu(111) with increasing the molecular coverage.

The functional changes of sumanene adsorption on Cu(111) are shown in Figure 5.7. The value of the work function is derived from the cutoff value of the UPS measurement. The x-axis is the change value of resonant frequency of QCM during evaporation and corresponds to the molecular deposition amount. The

work function of cleaning Cu(111) surface was determined to be 4.90 eV, which was roughly consistent with the literature value. After sumanene molecules approached to the clean surface of Cu(111), the work function is sharply reduced by about 1.4 eV, becomes 3.46 eV. The change of this working function can be explained like this: after the molecule approaches the surface, the molecule compressed the "leaking out" electron cloud of clean metal surfaces back into the metal. This may reduce its intrinsic dipole. Therefore, the effective work function that the molecule experiences is lowered[77].

- **ARPES spectra of sumanene monolayer on Cu(111)**

The band dispersions of the occupied and unoccupied states of organic semiconductors are indispensable information towards understanding the charge transport mechanism of holes and electrons, respectively. Angle-resolved photoelectron spectroscopy (ARPES) is frequently used as a standard technique for occupied states. In this work, we measured the distribution of bands in the molecular direction of sumanene monolayers by ARPES measurement.

As described above, the sumanene monolayer on Cu(111) shows a peculiar structure consisting of a one-dimensional bowl-stacking sumanene molecules which may be more tightly packed together by π-stacking. Therefore, it is expected that the superposition of the intermolecular wave functions of sumanene in this column direction will be significant, and the band dispersion can be realized in this direction. Therefore, we measured ARUPS along the molecular column direction, i.e. [11$\bar{2}$] direction, indicated by the blue line in the Figure 5.8. However, it should be noted that the sumanene monomolecular layer on Cu(111) has three rotational domains. Therefore, there are also contributions from different domains in different directions.

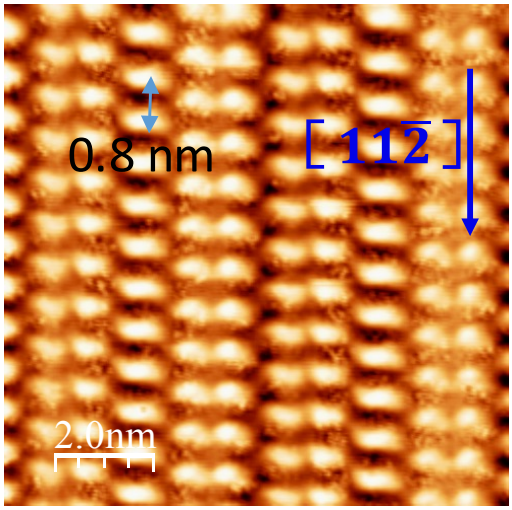

Figure 5.8 Scanning direction of ARPES for sumanene monolayer on Cu(111).

Figure 5.9 represents the measurement results of clean Cu(111) substrate and sumanene monolayer on Cu(111) obtained along the <112> direction, i.e. bowl-stacking direction. The vertical axis is the binding energy that assumes the Fermi energy to be the 0 eV, the horizontal axis represents the wavenumbers, and set the $\bar{\Gamma}$ point as 0 point. In order to make molecular orbitals clearer, the frequency band diagram shows second derivatives in the direction of binding energy. The corresponding relationship between signal strength and graph color is shown next to the diagram.

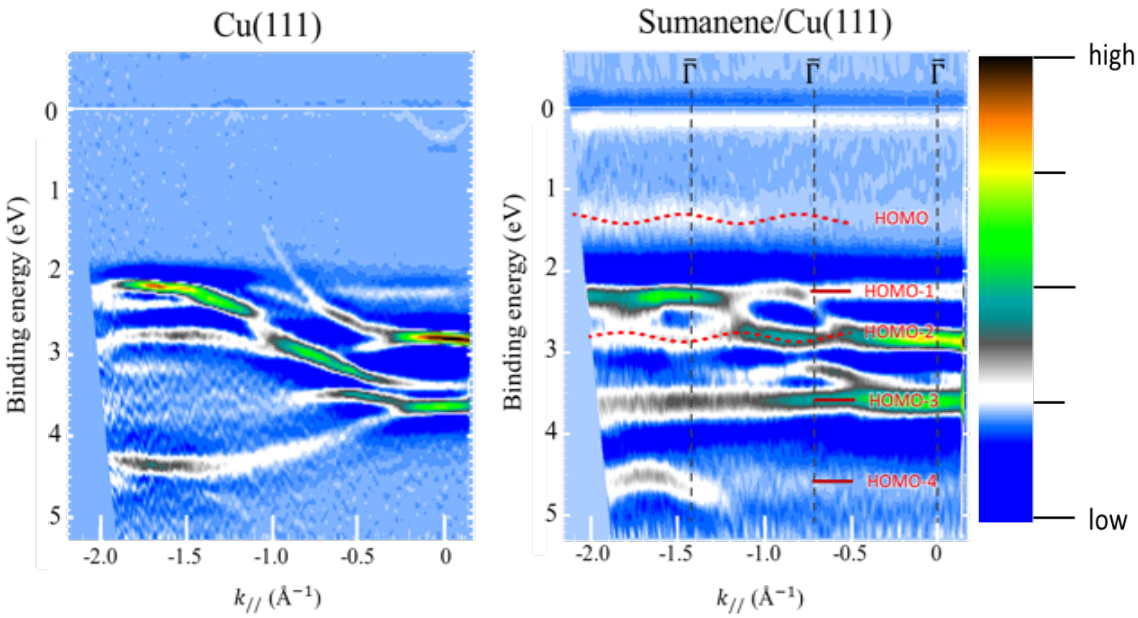

Figure 5.9 ARUPS spectra along [112̄] direction of the monolayers and substrates.

In the ARPES spectrum of the Cu(111) substrate, floating surface alignments can be clearly observed near the Fermi energy, indicating a clean Cu(111) surface with sufficiently wide terraces. The d-band of Cu(111) surface above the binding energy 2 eV can be observed from the image. In addition, there is a dispersion from Γ point to 1.2 Å^{-1}, which shows the sp band exist for Cu(111).

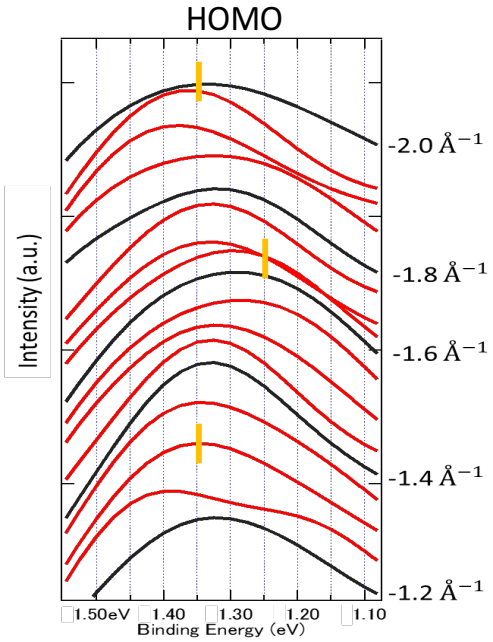

Figure 5.10 ARPES of sumanene on Cu(111) plotted at every 0.05 Å^{-1}.

For the ARPES spectrum of sumanene monolayer on Cu(111), small scattered new orbitals appear at binding energy of 1.4 eV, which is considered to be the HOMO of sumanene, as discussed above. Similar

distribution density of HOMO-1, HOMO-2, HOMO-3 and HOMO-4 are shown at the binding energy of 2.3 eV, 2.8 eV, 3.8 eV and 4.5 eV, respectively. Even though it is a little difficult to be distinguished from the d band of Cu(111) substrate.

Since the lattice distance in the direction of <112> of sumanene monolayer on Cu(111) is 0.8 nm as shown in the Figure 5.8. Therefore, the Brillouin zone width of this system is corresponding to 0.7 $Å^{-1}$ (Brillouin zone period of $2\pi / a$, where a is the lattice distance), and the black dashed lines in the Figure 5.9 indicate the Brillouin zone boundaries. The energy distribution of HOMO band shows a sinusoidal like changes during the Brillouin zone as indicted by the red dashed line in the spectrum. This may reflect the energy dispersion of the molecular orbitals of HOMO. To confirm the energy dispersion in more detail, ARUPS spectrum was plotted every 0.05 $Å^{-1}$ at the position of HOMO as shown in Figure 5.10. The vertical axis shows wavenumbers in the range of 1.2 $Å^{-1}$ ~ 2.0 $Å^{-1}$, and the horizontal axis represents the binding energy around HOMO band from 1.08 eV to 1.55 eV. Form the peak position of $k_{//}$ = -1.3 $Å^{-1}$, which shows the binding energy of 1.35 eV, to the peak position of $k_{//}$ = -1.65 $Å^{-1}$, which shows the binding energy of 1.25 eV, the binding energy shows the difference of 100 meV. And the peak position of $k_{//}$ = -2.0 $Å^{-1}$, which shows the binding energy of 1.35 eV, also shows a difference of 100 meV of the binding energy from the position of $k_{//}$ = -1.65 $Å^{-1}$. Therefore, there is an energy dispersion with a dispersion width of about 100 meV. This dispersion cycle is roughly the same as the width of the Brillouin zone of the sumanene monolayer alone the direction of <112>, which corresponding to the molecular stacking direction. Therefore, the dispersion of the HOMO band is surely come from sumanene monolayer orbitals. However, such a weak band dispersion it's not enough for the organic devices. In order to apply sumanene films with bowl-stacking arrangement to organic devices, higher densely structure is required.

5.4.2 Core Level Electronic Structure of Sumanene Monolayer on Cu(111)

To assess the consequences of these adsorption induced molecular distortions on the chemical structure of two kinds of sumanene monolayers, we performed X-ray photoelectron spectroscopy (XPS) and DFT calculation. The evolution of the shape of C 1s peak depending on the sumanene film thickness is discussed. The photon energy we used in this detection is $h\nu$=460 eV. We should note here that the kinetic energy of photoelectron from C1s is about 150 eV with the inelastic mean free path of about 3 nm[78]. Therefore, the XPS measurement can detect the photoelectrons from the top several molecular layers of the sample. The under layers of thin film sample may have no contributions to the C 1s spectrum. The C 1s spectrum of thin film can represent the information of sumanene molecules with no interaction with substrate.

Figure 5.11(a) shows the C 1s spectra of sumanene monolayer and sumanene thin film on Cu(111) represented by red and blue line, respectively. In the spectrum of sumanene monolayer, the shape of the peak presents an asymmetrical form with a low left side and a high right side. Whereas, the theoretically simulated spectrum of single sumanene molecule shows the opposite asymmetry with a high left side and low right side (as shown in Figure 5.11 (b)), which is in consistent with the spectrum of suamene thin film (as shown in Figure 5.11(a)). The different C 1s peak of sumanene monolayer and thin film indicates that the C atoms of

sumanene in the monolayer have a strong interaction with the metal substrate. Therefore, the modified sumanene monolayer on Cu(111) shows a significantly different molecular arrangement with that of bulk phase, which may influence the further thin film growth. The C 1s peak of sumanene thin film shows another single feature with different symmetry with that of monolayer at the binding energy of about 284 eV. The small feature at the binding energy of about 287.5 eV, which shows the same binding energy as C=O band, may be caused by the oxidized sumanene molecules after taking the sample out of the UHV chamber to the atmosphere before the XPS measurement.

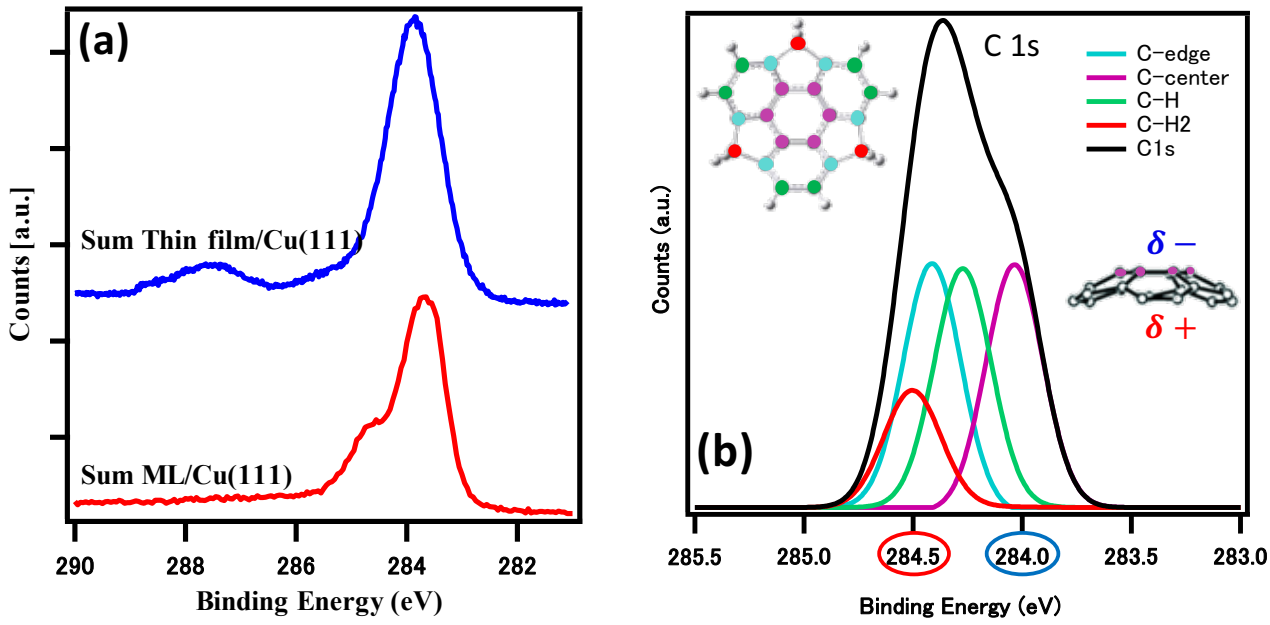

Figure 5.11 (a) XPS spectra of sumanene monolayer and thin film on Cu(111); (b) DFT calculation of C 1s spectrum of sumanene in gas phase.

To clarify the details of the core level shift, the calculated C 1s core-level line shape of single molecule was deconvoluted into four features attributed to aromatic carbon atoms in the central benzene ring, carbon atoms at edge position, carbon atoms linked to hydrogen and carbon atoms linked to two hydrogens, which was indicated by different colors as shown in Figure 5.11(b). The right shoulder of the peak with lower binding energy of 284.0 eV is mainly contributed by the carbon atoms in the central benzene ring, the left shoulder with higher binding energy is contributed by the other carbon atoms. This result meets the dipole moment of sumanene molecule well, indicating the credible of the calculation result. Figure 5.12 shows the C 1s peak sumanene monolayer on Cu(111) fitted mainly with two peak components sited at 284.72eV and 283.69 eV with a Gaussian-Lorentzian function. It suggest that both higher binding energy shift and lower binding energy shift occurred for sumanene monolayer on Cu(111) compared with sumanene molecule in gas phase. Even though we also want to have a thorough deconvolusion for the experimental XPS spectrum, however, the complicated molecular arrangement of five different molecular adsorptions of sumanene monolayer on Cu(111) results in a broader peak shape and convoluted core level shift[63]. Hence, the possibility contribution from these tilted molecules cannot be discriminated solely on the basis of the XPS peak's width and skewness.

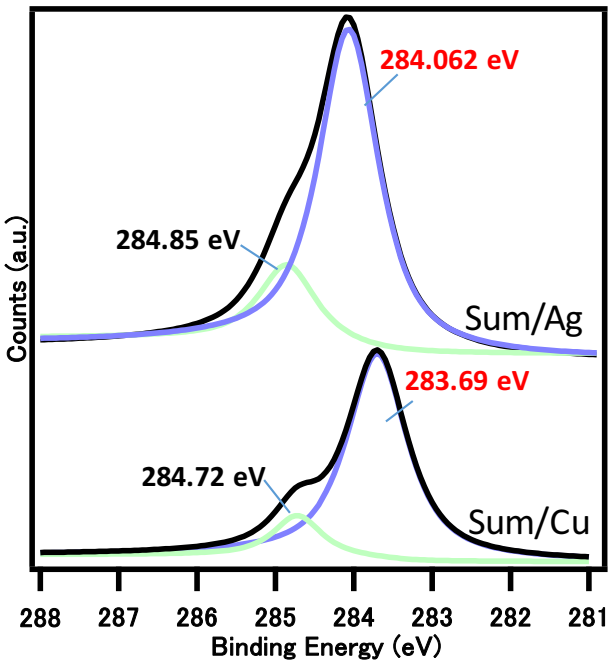

Figure 5.12 C1s spectra of sumanene monolayers on Ag(111) and Cu(111) fitted by two peaks.

5.4.3 Valence Electronic Structure of Sumanene Monolayer on Ag(111)

- **UPS spectra of sumanene monolayer on Ag(111)**

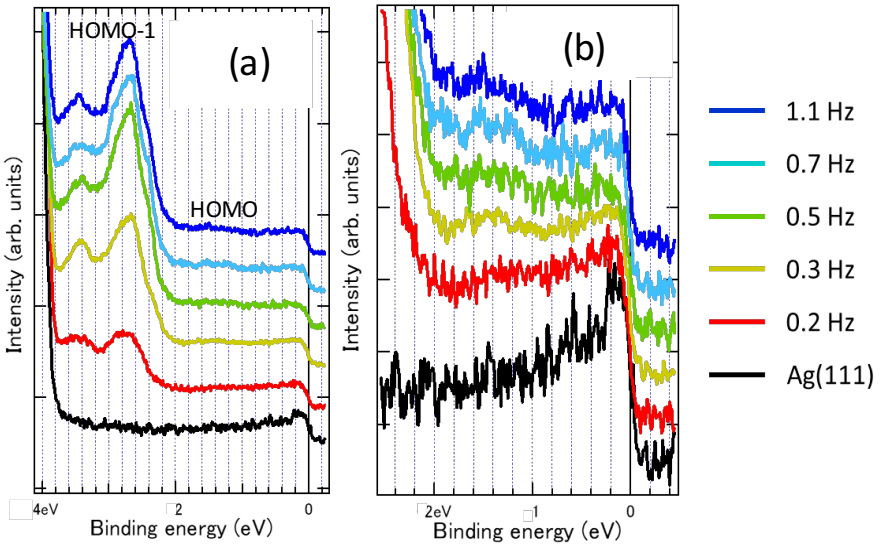

Figure 5.13 (a) UPS spectra of sumanene monolayers on Ag(111); (b) Zoom at HOMO peak.

Figure 5.13 shows the UPS spectra of sumanene monolayer on Ag(111). The horizontal axis represents the binding energy where the Fermi energy was marked as 0 eV. Clear surface state of Ag(111) surface can be observed around Fermi level in the UPS spectrum, indicating a clean surface was obtained. Since the d-band photoemission of clean Ag(111) surface appears at 4 eV, we can observe not only the HOMO band but also

deeper HOMO levels of sumanene monolayer on Ag(111) as shown in Figure 5.13(a). Figure 5.14 (b) clearly shows the HOMO band at about 1.4 eV. There is no obvious change of HOMOs with increasing the molecular amount, which is same as the result of sumanene monolayer on Cu(111). Since the molecular arrangement of sumanene on Ag(111) shows two different kind of sumanene molecules (bowl-up and bowl-down), and bowl-inversion can be occurred during the UPS measurement. Therefore, it's possible that the HOMOs of the average information from the photoelectron spectrum has been diffused.

- **Work function of sumanene monolayer on Ag(111)**

Figure 5.14 shows the evolution of work function with increasing the sumanene molecules. The work function of clean Ag(111) substrate is observed to be 4.57 eV, which is consistent with the literature value. With the full coverage of sumanene monolayer, the work function decreased by about 1.0 eV, finally comes to 3.58 eV. The decrease reaction of the work function is the same as that of sumanene monolayer on Cu(111).

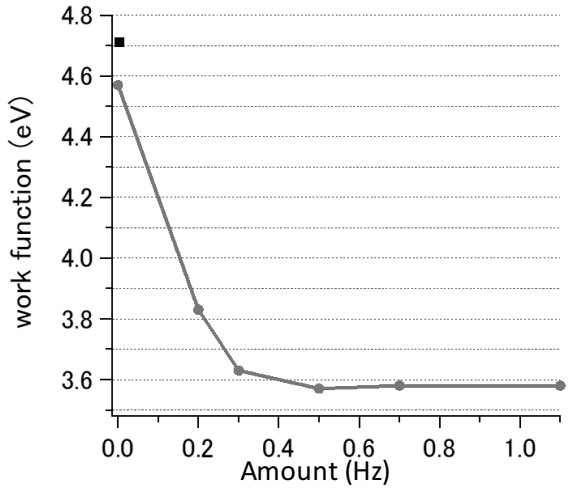

Figure 5.14 Work function of sumanene monolayer on Ag(111) with increasing the coverage.

- **ARPES spectra of sumanene monolayer on Ag(111)**

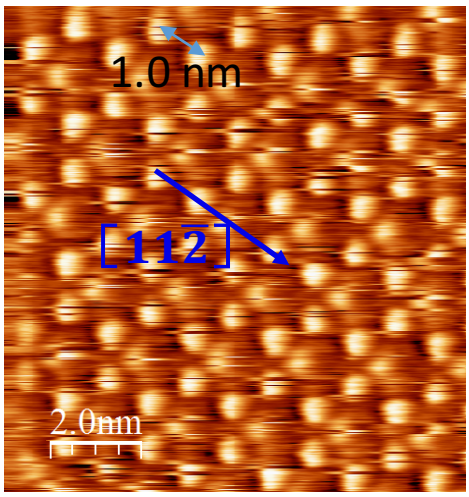

Figure 5.15 Scanning direction of ARPES measurement.

Figure 5.16(a) and (b) show the ARPES spectra of the clean Ag(111) substrate and sumanene monolayer on Ag(111) obtained along the [112] direction as indicated in Figure 5.15. The d-band of Ag(111) substrate at above the binding energy of 4 eV was observed in the Figure 5.16(a), where we can also observed a dispersed sp band from Γ point to 1.2 $Å^{-1}$. By comparison with the ARPES spectra, we can easily mark the band positon of HOMO, HOMO-1, HOMO-2, HOMO-3 and HOMO-4 at range of the binding energy of 1.3 eV~3.7 eV. Since the molecular distance of sumanene monolayer on Ag(111) is 1.0 nm as shown in Figure 5.15, the Brillouin zone width is estimated to be 0.629 $Å^{-1}$. The Brillouin zone boundary is marked as red dashed line as shown in Figure 5.16(b). There are almost no dispersed orbitals.

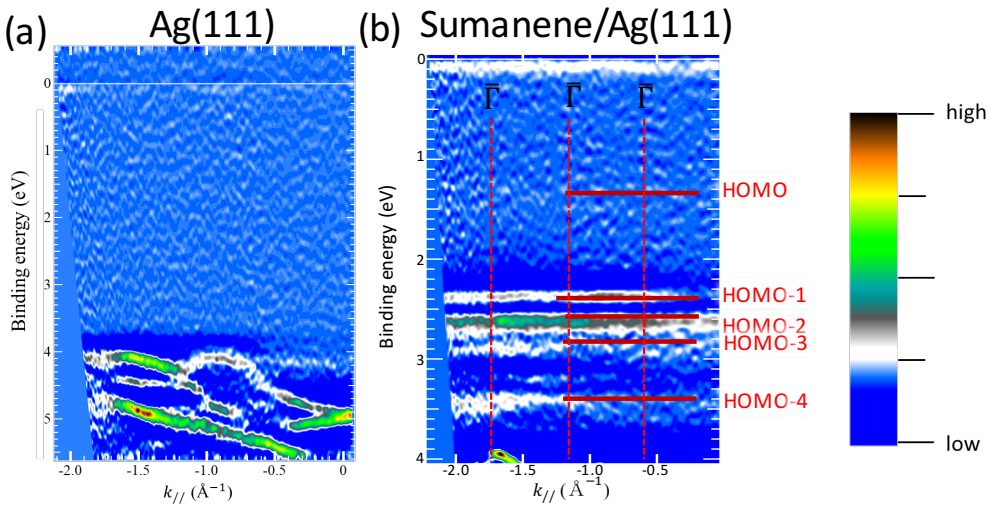

Figure 5.16 (a)ARUPS spectra along [112̄] direction of Ag(111) substrate and the monolayers.

Therefore, the HOMO band of sumanene monolayers shows a better dispersion on Cu(111) than on Ag(111). Thus, we can speculate that the degree of non-locality is greater for bowl-stacking arrangement of sumanene, which indicates a better charge-transport ability. Higher electron mobility along bowl stacked direction, because the overlap between the electron orbitals is maximized.

5.4.4 Core Level Electronic Structure of Sumanene Monolayer on Ag(111)

As shown in Figure 5.12, the C 1s core level peak of XPS spectrum of sumanene monolayer on Ag(111) shows the asymmetrical shape with a low left side and a high right side, which is opposite to the shape of C 1s peak of sumanene in the gas phase (Figure 5.11(b)). The different C 1s peak of sumanene monolayer and thin film indicates that the C atoms of sumanene in the monolayer have a strong interaction with Ag(111) substrate. Therefore, the modified sumanene monolayer on Ag(111) also shows a peculiar molecular arrangement with bowl-up and bowl-down comformation, which may influence the further sumanene thin film growth.

The C 1s peak of sumanene monolayer on Ag(111) was fitted with two peak components as shown in Figure 5.12, which were sited at 284.85 eV and 284.062 eV, respectively, with a Gaussian-Lorentzian function.

Since the molecular arrangement of sumanene monolayer on Ag(111) shows a complicated bowl-up and bowl-down arrangement as introduced above, and the core level shift of individual atoms of different position in the molecule is identified to be different[63], the experimental XPS spectrum does not allow for a clear explanation of the core level shift after the molecule approaching the surface. By comparing the C 1s peak position of sumanene monolayer on Cu(111) and Ag(111), the left component of each peak sited at the position with similar binding energy (284.85 eV for sumanene on Ag(111), 284.72 eV for sumanene on Cu(111)). Whereas, the right component of C 1a peak of sumanene on Cu(111) shows lower binding energy than that of on Ag(111). The difference value is about 0.37 eV. Therefore, the core level shift value of sumanene on Cu(111) is 0.37 eV larger than that of sumanene on Ag(111), which may be caused by the more complicated molecular adsorption morphology of adsorbed sumanene on Cu(111).

5.4.5 Energy Level Alignment of Sumanene Monolayers

As described above, the work function of the Cu(111) substrate was determined to be $\Phi_{Cu} = 4.9$ eV. The work function for the sumanene full coverage monolayer was measured to be Φ_{ML} =3.46 eV. This gives a total work function shift of

$$\Delta\Phi = \Phi_{Cu} - \Phi_{ML} = 1.44\ eV \quad (5.1)$$

The ionization energy describes the energy to remove electrons from the neutral molecule to create a cation. The ionization potential (E_{ion}) of suamnene monolayer on Cu(111) was determined by adding work function of the monolayer Φ_{ML} to the HOMO, yielding

$$E_{ion} = \Phi_{ML} + HOMO = 4.86\ eV \quad (5.2)$$

Therefore, the energy level alignment of the sumanene monolayer on Cu(111) resulting from all of the measurements above is shown in the band diagram of Figure 5.17(a).

The work function of the Ag(111) substrate was determined to be $\Phi_{Ag} = 4.7$ eV. The work function for the sumanene full coverage monolayer was measured to be Φ_{ML} =3.58 eV. The total work function shift is

$$\Delta\Phi = \Phi_{Ag} - \Phi_{ML} = 1.12\ eV \quad (5.3)$$

The ionization potential (E_{ion}) was estimated to be

$$E_{ion} = \Phi_{ML} + HOMO = 4.98\ eV \quad (5.4)$$

The energy level alignment of the sumanene monolayer on Ag(111) is shown in the band diagram of Figure 5.17(b).

The ionization potential energy of sumanene in gas phase is calculated to be 5.2 eV, which is a little different from the experimental results of that of sumanene monolayers on both Cu(111) and Ag(111) substrates. The change of ionization potential energy of sumanene in the monolayers may be caused by intermolecular interactions within the monolayer and molecule-substrate interaction.

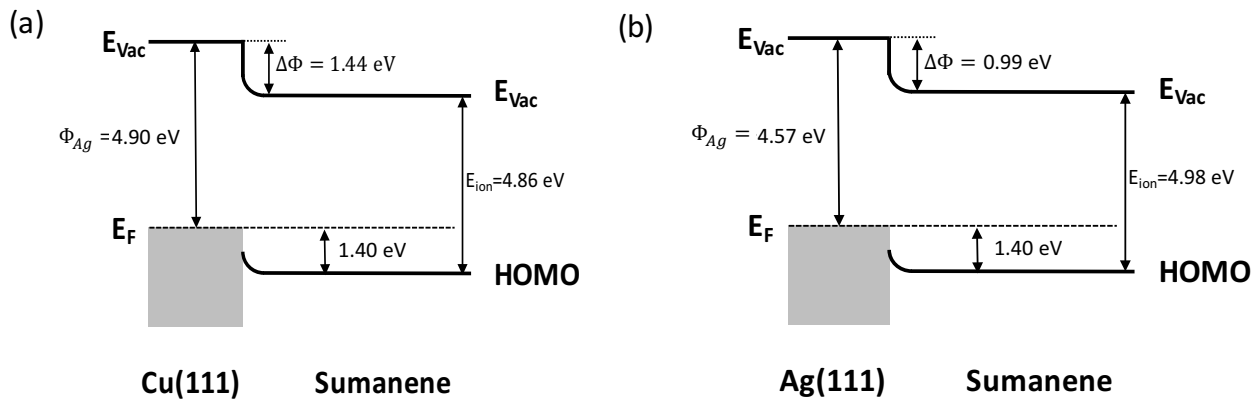

Figure 5.17 (a)Band diagram of sumanene monolayer on Cu(111) interface; (b)Band diagram of sumanene monolayer on Ag(111) interface.

5.5 Calculation of Force Constant of Intermolecular Van der Waals force

Although the bowl-up and bowl-down arrangement is more reported for sumanene monolayer on metal surface, the one-dimensional bowl-stacking sumanene monolayer that we observed on Cu(111) has shown the better charge-transport potential. Thus, we speculate that bowl-stacking arrangement have stronger intermolecular interaction than bowl-up-down arrangement. Then, a DFT calculation was deduced to confirm this speculation. One-dimensional potential energy curves were constructed by calculating the interaction energies as a function of intermolecular distance. Figure 5.19 shows the potential energy curves for all the sumanene dimers of their interaction energies versus the center to center distance between the the molecules of the sumanene dimer. The configuration of the sumanene dimer models are shown in the inset of corresponding figures. The x-axis of the chart shows the relative distance between two sumanene molecules in the dimer to the position with minimum binding energy of the dimer. The y-axis shows the potential energy of the dimer system. As a model of the molecular configuration, we simply use two pairs of molecules with the bowl-up-down arrangement (inset of Figure 5.19(a)) and bowl-up-up arrangement (inset of Figure 5.19(b)), that were observed from the STM image, for sumanene monolayer on Ag(111)/Au(111). For sumanene monolayer on Cu(111), the one-dimensional molecular arrangement with five different rows, which consist of both $\pi - H$ and $\pi - \pi$ bonding, is complicated. STM image cannot give a detailed molecular configuration. Therefore, in this work, simply using a sumanene dimer with the bowl-stacking configuration of sumanene single crystal, as shown by the inset of Figure 5.19(c).

It should be noted that, the intermolecular distance of bowl-up-down and bowl-up-up sumanene dimers at the equilibrium position is 1 nm, which is same with the intermolecular distance in the real sumanene monolayer on Au(111)/Ag(111). The intermolecular distance of sumanene single crystal dimer at the equilibrium position is 3.84 Å, which is smaller than the intermolecular distance with 3.853 Å in the real

single crystal. That's because the distance between two molecules in a crystal is affected by all the surrounding molecules, which is absent for the calculated single crystal dimer in this work. What's more, the real intermolecular distances along the one-dimensional molecule rows is 0.85 nm in phase 1 and 1.2 nm in phase 2 of sumanene monolayer on Cu(111), which is significantly different from the intermolecular distance of the single crystal. The potential energy of the bowl-stacking dimer with the intermolecular distance of 0.85 nm is 0.01 eV according to the potential energy curve of Figure 5.19(c), which is smaller than the potential energy of bowl-up-down and bowl-up-up sumanene dimers with the value of 0.12 eV and 0.06 eV, respectively, as shown in Table 5.1, which can indicate the order of the stability of these dimers. Therefore, sumanene molecules with bowl-up and bowl-down arrangement is more stable than the bowl-stacking arrangement with the intermolecular distance of 0.85 nm. However, the sumanene monolayer on Cu(111) with one-dimensional structure is more stable than the sumanene monolayer on Au(111)/Ag(111) with the bowl-up and bowl-down arrangement during the STM measurements. And the molecular arrangement of sumanene monolayer on Cu(111) with different kinds of tilted bowl-stacking molecular rows is more complicated than the calculated case. Therefore, a stronger interaction between sumanene molecules and Cu(111) substrate and stronger intermolecular interactions between the tilted bowl-stacking sumanene molecules can be speculated.

Table 5.1 Calculated results for sumanene dimers.

	Single crystal 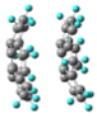	Bowl-up-down 	Bowl-up-up 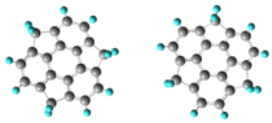
Minimum potential energy (eV)	0.6	0.12	0.06
Force constant (kg/s^2)	34	9.1	5.9

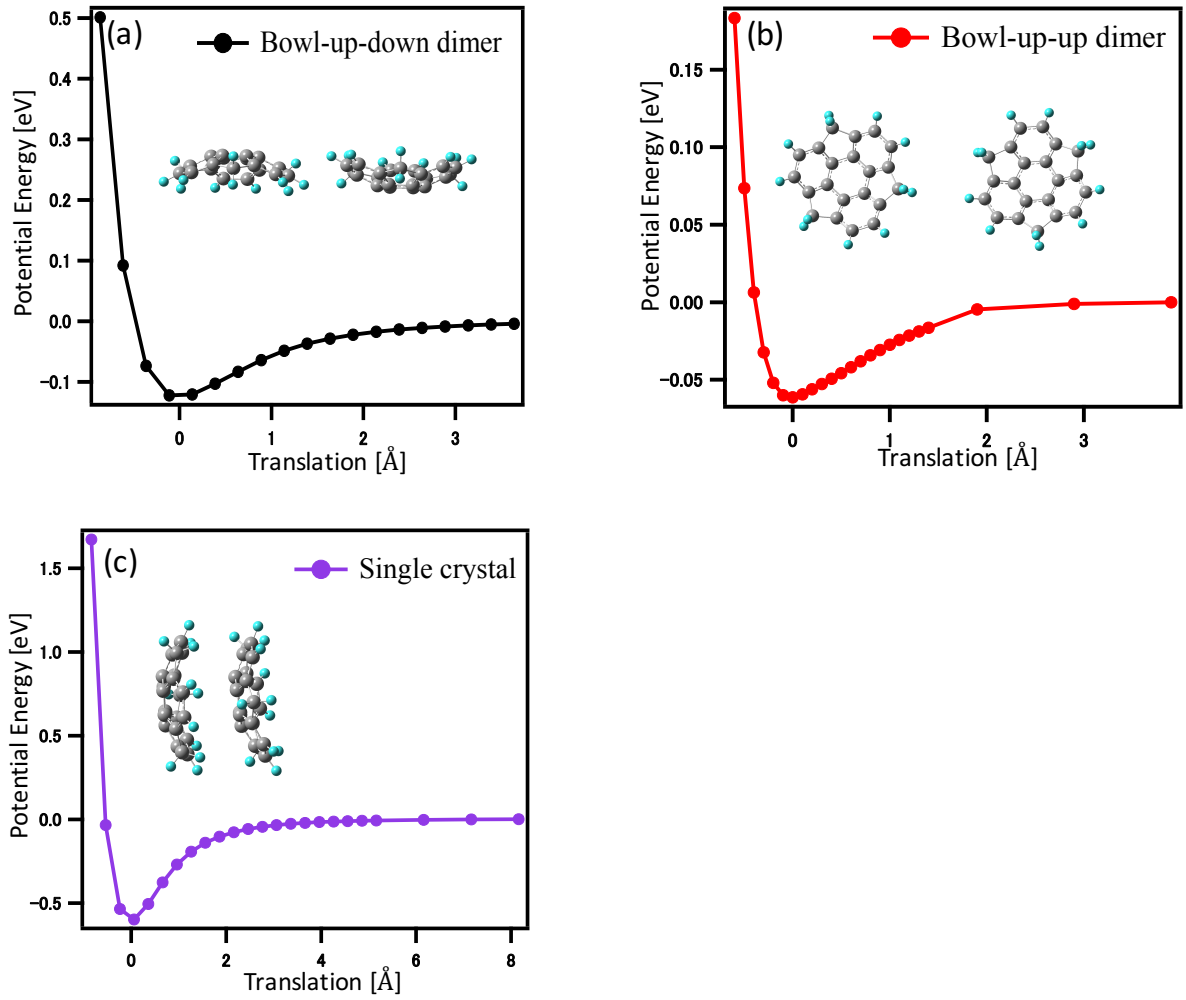

Figure 5.19 Potential energy curves for sumanene dimers versus the center to center distance between the the monomers of the sumanene dimer. The configuration of each dimer is shown in the inset of each corresponding figures. Potential energies and translation distance relative to the equilibrium position are also shown.

The force constant of the intermolecular van der Waals bonding were estimated for all the dimer systems, simply assuming the simple harmonic oscillation at the position with minimum binding energy. Then, we made a rearrangement of the potential curves. Set the position with minimum binding energy as equilibrium and change the y-axis to be the relative energy to the equilibrium position, as shown in Figure 5.20. Fitting equation near the equilibrium are $y=0.9685x^2$, $y=0.2602x^2$, and $y=0.1679x^2$ for the potential curves of single crystal dimer, bowl-up-down dimer, and bowl-up-up dimer, respectively. Considering the potential energy for elastic formula

$$U=\frac{1}{2}kx^2 \quad (5.9)$$

where U is potential energy of a spring at a certain position; k is the spring constant; x is distance from the equilibrium when the spring is stretched or compressed. We can simply deduce the force constant of the

intermolecular van der Waals bonding for all the sumanene dimers, as listed in Table 5.1. Sumanene dimer with bowl-up-down configuration shows the larger force constant with the value of 9.1 kg/s^2 than that of sumanene dimer with bowl-up-up configuration with the value of 5.9 kg/s^2. What's more, the order of minimum potential energy values at the equilibrium position of the sumanene dimers with bowl-up-down dimer and bowl-up-up dimer are 0.12 eV and 0.06 eV, respectively, as shown in Table 5.1. Considering the phenomenon that the sumanene submonolayer on Ag(111) substrate was reported to shown the bowl-up molecular arrangement in the beginning, because of the interaction between the molecules and the substrate. After reaching the full monolayer coverage, the molecular arrangement changes to bowl-up-down configuration. This phenomenon can be explained as the intermolecular interaction between sumanene molecules also plays a certain role at this time, therefore, the molecular arrangement of the system changes to an energetically favorable configuration. Sumanene monolayer on Cu(111) was revealed to show the one-dimensional structure with different bowl-stacking rows by STM measurement in this work. The force constant of van der Waals bonding of single crystal sumanene dimers is 34 kg/s^2, which is much larger than the value of bowl-up-down dimer and bowl-up-up dimer, indicating the relatively stronger intermolecular van der Waals bonding in sumanene monolayer on Cu(111) than on Ag(111)/Au(111).

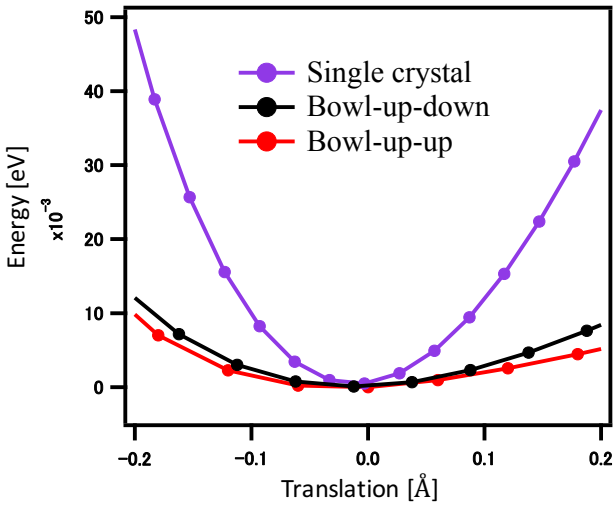

Figure 5.20 Zoom area of the equilibrium position with minimum binding energy of the potential energy curves for sumanene dimers.

5.6 Stability of morphology of sumanene monolayers with adsorption of K atoms

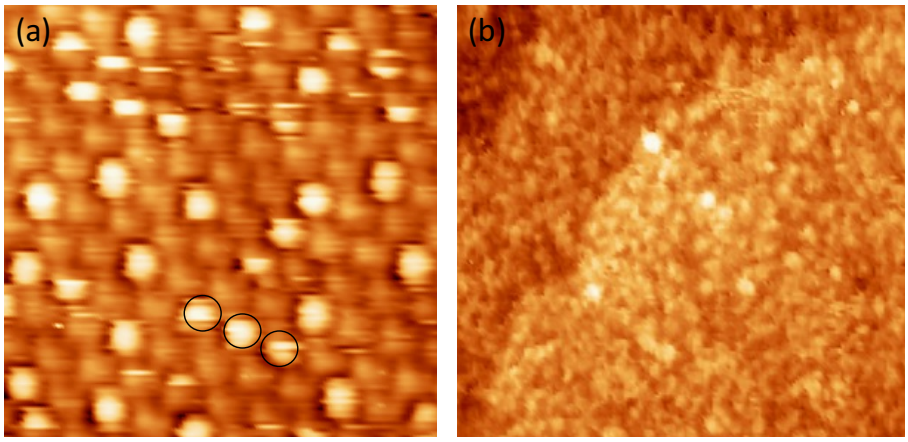

Figure 5.21 Potassium adsorption on sumanene monolayer on Ag(111) at room temperature. (a) STM image sumanene monolayer with the adsorption of K atoms with the amount of 0.3 ML. (b) STM image sumanene monolayer with randomly molecular arrangement after the adsorption of K atom with the amount of 1 ML.

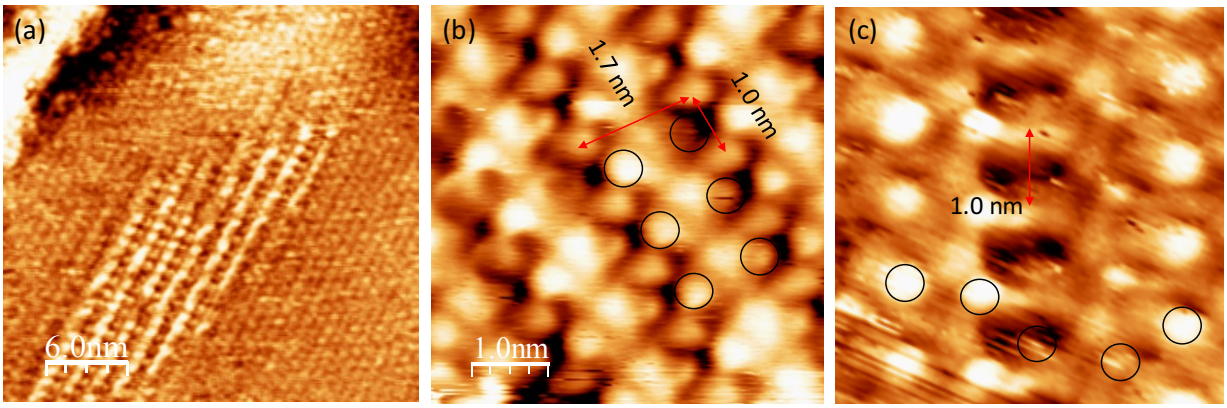

Figure 5.22 Potassium adsorption on sumanene monolayer on Cu(111) at room temperature. (a) STM image of sumanene monolayer with the adsorption of small amount of K atoms. (b) Small-scale STM image of phase 2 with two-rows structure of sumanene monolayer on Cu(111) with the adsorption of K atoms. (c) Small-scale STM image of phase 1 with five-rows structure of sumanene monolayer on Cu(111) with the adsorption of K atoms.

The concave face of sumanene are expected to be the ideal model for host-gust interaction by adsorption of gust molecules. In this work, we explored the adsorption of K atoms on the two kinds of sumanene monolayers with different molecular arrangement at room temperature. For the adsorption of K atom with the amount of 0.3 ML on sumanene monolayer on Ag(111), K atom guests are imaged as single bright spots as shown in the STM image in Figure 5.21(a). There is no preferable adsorption phenomenon at positions

corresponding to bowl-up hosts of sumanene monolayer[73], and there are even three adjacent bright spots as marked by the black cycles in the STM image. All the bright spot seems similar which can not be caused by the adsorption of K atoms on both bowl-up and bowl-down molecules[73]. Considering the bowl inversion phenomenon of sumanene monolayer as we discussed above, therefore, we speculate that adsorption of K atom may cause the bowl-down molecules invert, causing the K atoms adsorbed on any sumanene molecule in the monolayer. It clearly shows that K interact directly to the π orbital of sumanene. Therefore, the effectively adsorbed K atoms in the concave side of sumanene in this well-ordered system is expected to be a very simple model for research of alkali-metal doping of aromatic molecules, which has been known to emerge interesting properties such as superconductivity or metal-insulator transitions[79]. After increasing the adsorption of K atoms with the amount of 1 ML, the sumanene monolayer changed to randomly arrangement as shown in Figure 5.21(b).

We also explored the adsorption of K atoms on the sumanene monolayer with bowl-stacking molecular arrangement on Cu(111) at room temperature. Figure 5.22(a) shows the STM image of of sumanene monolayer with the adsorption of small amount of K atoms at room temperature. The morphology of the K-doped sumanene monolayer keeps the one-dimensional structure as the pure sumanene monolayer. Figure 5.22(b) shows the K-doped sumanene monolayer with two-rows structure on Cu(111) with the unit cell of 1.0×1.7 nm, which shows a little expansion than the unit cell of original two-rows molecular structure. The K-doped sumanene monolayer with five-rows structure also shows an expansion with the molecular distance with 1 nm along the row direction. By comparison with the molecular arrangement of sumanene monolayer before (as shown in Figure 5.1(b) and Figure 5.3(a)) and after the K adsorption, the possible positions of potassium atoms are marked by black circles in Figure 5.22(b) and (c). After the deposition of more K atoms, the one-dimensional structure can still be observed. Even though the domain size is shown to be shrunk, which may have caused by the expansion of the unit cell after the adsorption of K atoms. The randomly molecular arrangement of K-doped sumanene monolayer on Ag(111) and well-ordered one-dimensional molecular arrangement of K-doped sumanene monolayer on Cu(111) can well illustrate the stronger intermolecular interactions of bowl-stacking sumanene arrangement than the bowl-up-down sumanene arrangement.

5.7 Sumanene Thin Film

5.7.1 Morphology of Sumanene Thin Films

For thicker films, we further deposited sumanene molecules with the deposition rate of 1 ML/100s on their monolayers on Cu(111) and Au(111), respectively. Figure 5.21(a) show the optical microscope images at several different areas of sumanene thin films on Cu(111) with the molecular coverage of 70 ML. No obvious island structure was observed, which is different from the morphology of picene and DNTT thin films with the extremely large crystal island structure as discussed in Chapter 4.

Figure 5.22(a) shows the AFM image of the sumanene thin film morphology on Cu(111) with a stair-step structure. The uneven surface can be observed, indicating some molecules indeed adsorbed on the Cu(111)

surface. Because the AFM measurement was performed after taking the sample out from the UHV chamber, the topography structure of sumanene thin film may be breakdown during this procedure. Figure 5.22(c) is the height line profile corresponding to the scanning line in the AFM image, shows the terraces structure with a step height range of about 0.2-0.4 nm. For comparison, we checked the same Cu(111) surface without sumanene by AFM. The topography of the clean Cu(111) surface is shown in Figure 5.22(b), and Figure 5.22(d) shows the height profile corresponding to the scanning line in the AFM image. Similar stair-step topography and height distance of the terraces with sumanene thin film on Cu(111) were observed, indicating only a ultra-thin film exists.

For the morphology of sumanene thin film on Au(111), Figure 5.21(b) shows the optical microscope images at several different areas of sumanene thin films on Ag(111) with the molecular coverage of 70 ML, which shows the similar inconspicuous structure morphology with sumanene thin film on Cu(111). The AFM image of sumanene thin film on Au(111) also shows a stair-step morphology with the height range of about 0.3-0.5 nm as shown in Figure 5.23. Since we deposited the same large amount of molecules, i.e. 70 ML, as picene and DNTT thin films as discussed in Chapter 4. These results of sumanene thin films observed from optical microscope and AFM measurements may indicate an amorphous structure or the uniform crystallinity structure of sumanene thin films on Cu(111) and Au(111). Therefore, more preciously measurement is required.

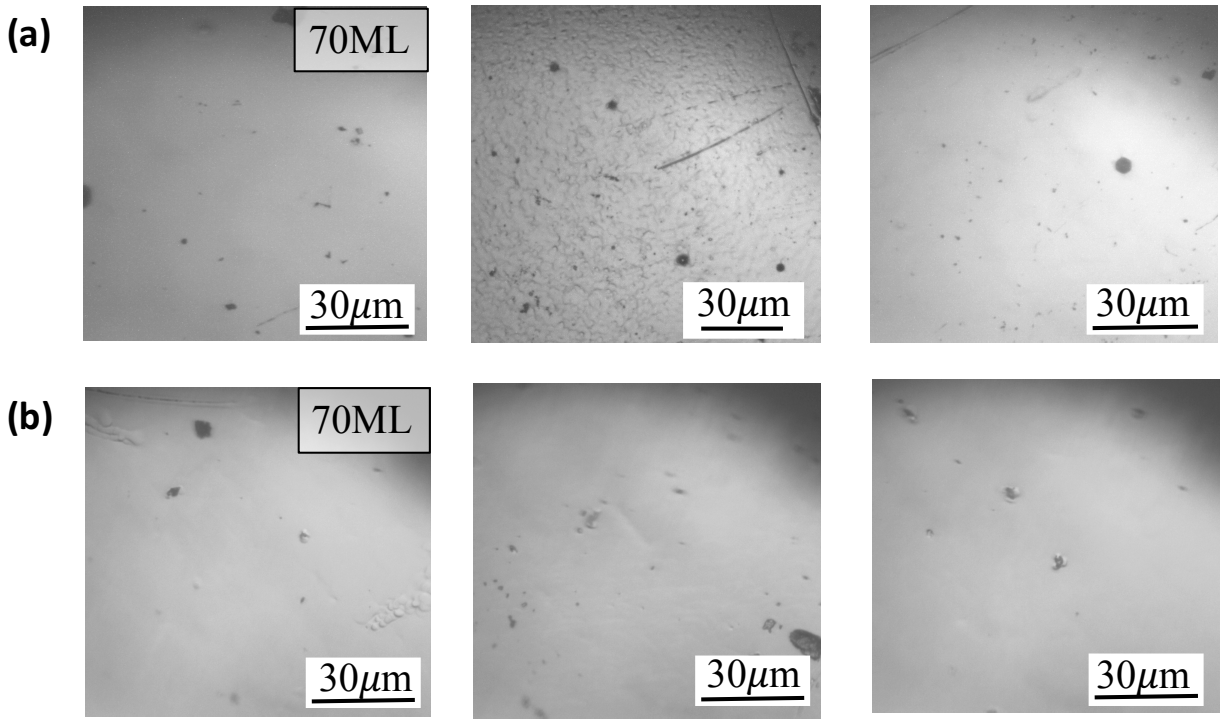

Figure 5.21 (a) Optical microscope images at three different areas of sumanene multilayer film on Cu(111); (b) Optical microscope images at three different areas of sumanene multilayer film on Au(111).

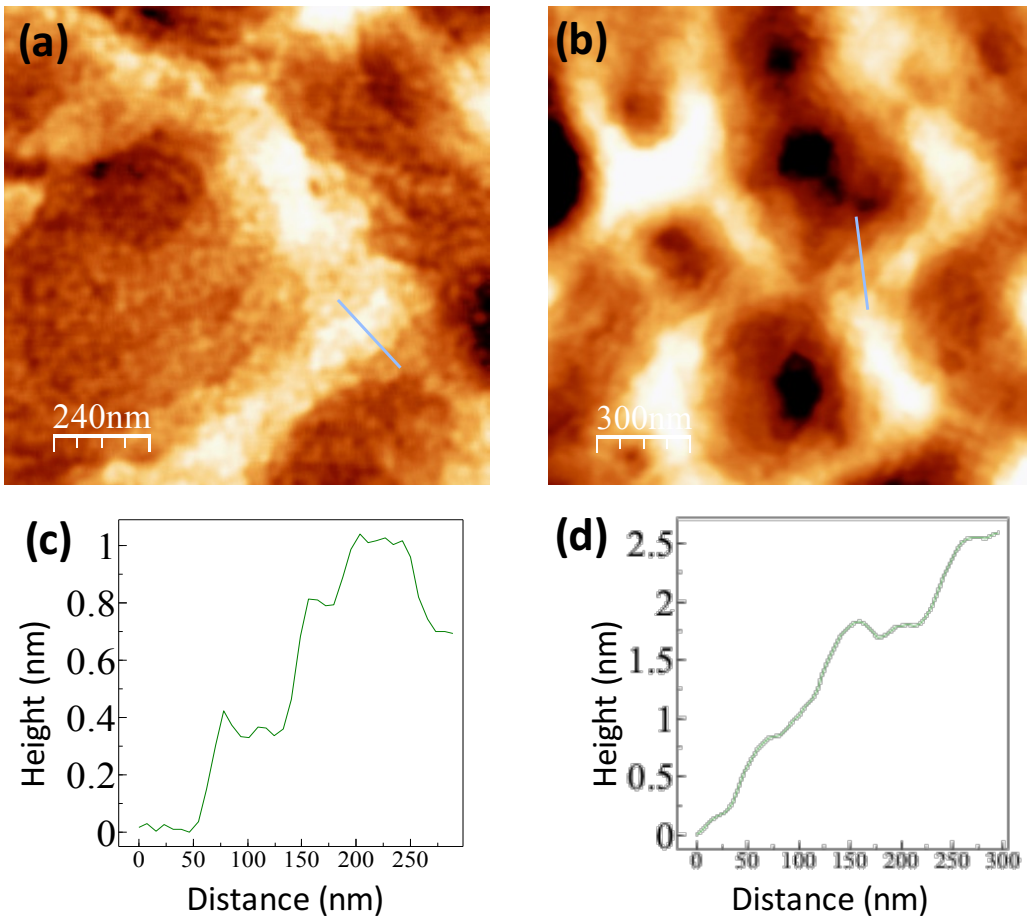

Figure 5.22 (a)AFM image of sumanene thin film on Cu(111) with its corresponding (c) height profile; (b) AFM image of clean Cu(111) sureface with its corresponding (d) height profile.

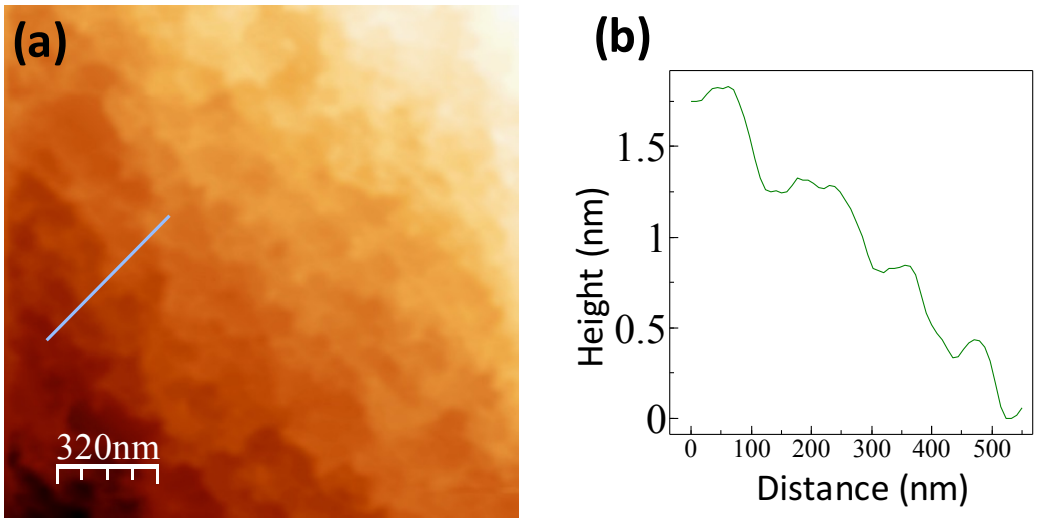

Figure 5.23 a)AFM image of sumanene thin film on Au(111) with its (b) height profile.

5.7.2 Molecular Arrangement of Sumanene Thin Films

To illustrate the detailed molecular arrangement of sumanene thin films, we did the XRD measurements. XRD spectra of the two sumanene thin films on Cu(111) and Au(111), respectively, were shown in Figure 5.24(a), where the horizontal axis of the spectra represents the diffraction angle 2θ, vertical axis shows the density of the diffraction pattern. The spectrum of Au(111) sample (black line in Figure 5.24(b)) only have an diffraction peak of Au(111) substrate, indicating an amorphous molecular arrangement of sumanene thin film on Au(111). As shown in the XRD spectrum of sumanene thin film on Cu(111) (red line in Figure 5.24(a)), there is a diffraction peak appearing at the diffraction angle of 2θ=39.0°, which corresponding to the (502) plane of sumanene single crystal by comparing with the analyzed diffraction pattern of sumanene powder as shown in Figure 5.24(c). Another diffraction peak at 2θ=43.4° of the the spectrum in Figure 5.24(a), shows only the onset and tail end here because of its high intensity, belongs to Cu(111) substrate.

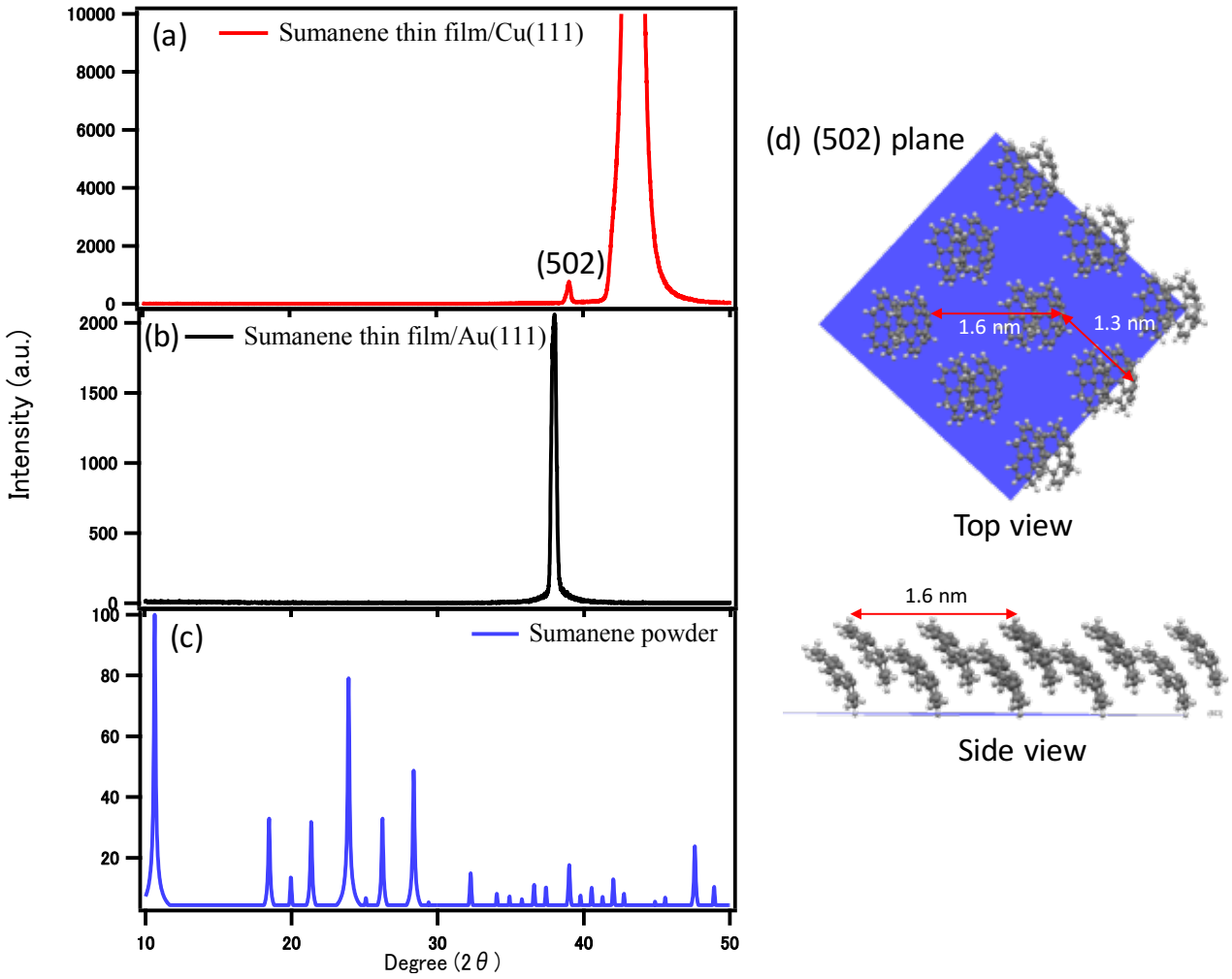

Figure 5.24 (a,b) XRD spectra of sumanene thin film on Cu(111) and Au(111), respectively; (c) Calculated diffraction pattern of sumanene powder; (c) Molecular arrangement of (502) plane.

Figure 5.24(d) illustrates the diagram of molecular arrangement of the (502) plane of sumanene single crystal. The top view and side view of the diagram reveals a characteristic orientation of tilted adsorbed sumanene molecules respect to the substrate, which is similar to the tilted bowl-stacking molecular arrangement of sumanene monolayer on Cu(111). Even though the unit cell of (502) plane (1.6×1.3 nm) is very distinct from the value of sumanene monolayer on Cu(111) (0.85×4.2 nm).

Therefore, considering all the results above, we can speculate that the weak intermolecular interaction of bowl-up and bowl-down sumanene monolayer on Au(111) or Ag(111) is not stable enough to establish a well-ordered thin film. However, the bowl-stacking sumanene monolayer on Cu(111) with a stronger intermolecular interaction can facilitating the stacking of the further sumanene molecules and forming an well-ordered thin film structure. It should be noted here, sumanene thin film with rod like structure has been obtained on HMDS-treated glass substrates, which can reduce the interaction between molecules and substrate. Thus, it can be speculated that the strong interaction between sumanene molecules and substrates in this work make the monolayer template effect obvious.

5.8 Summary

In this Chapter we have demonstrated the thin film growth of sumanene from the prestage monolayer to multilayer and revealed the intermolecular interactions of two different intermolecular arrangements of sumanene molecules, both experimentally and theoretically.

STM measurements revealed that sumanene monolayers show two kinds of distinct molecular arrangements with one-dimensional bowl-stacking molecular arrangement on Cu(111) and bowl-up and bowl-down molecular arrangement on Ag(111)/Au(111), respectively. The electronic structure of these two kinds of peculiar sumanene monolayers were characterized by UPS, XPS and ARPES. We have observed a slight dispersion of HOMO band with 100 meV, indicating a strong intermolecular interaction, along the bowl-stacking direction of sumanene monolayer on Cu(111). What's more, after doping of alkali metals on the sumanene monolayers, the one-dimensional bowl-stacking molecular arrangement on Cu(111) shows more stable ability than that of bowl-up and bowl-down molecular arrangement on Ag(111)/Au(111). Therefore, the stronger intermolecular interaction of sumanene on Cu(111) can be expected. We have proposed the detailed theoretical model with DFT calculation method to describe the intermolecular interaction of bowl-stacking sumanene dimer and bowl-up and bowl-down sumanene dimer. Within our calculation, stronger intermolecular interaction along the bowl-stacking direction in monolayer is indicated by the larger force constant of van der Walls force.

In addition, the superior growth of sumanene thin film on Cu(111) than Au(111) and Ag(111)was found. The morphology of sumanene thin films was characterized by optical microscope and AFM. The XRD measurement revealed that the well-ordered molecular arrangement in the sumanene thin film on Cu(111) shows the same molecular arrangement of (502) plane of sumanene single crystal. Whereas, the sumanene thin film on Au(111) shows the disordered molecular arrangement according to the XRD measurement result.

Therefore, we speculate that superior growth of sumanene thin film on Cu(111) may caused by the stronger intermolecular interaction along the bowl-stacking direction in monolayer, which can stabilize the further molecules.

Chapter 6
General Conclusion

In this thesis, we have studied the thin film growth from the initial monolayers to multilayer films of three organic semiconductor molecules, picene, DNTT, and sumanene, where intermolecular interaction is enhanced. The general conclusions of this work are as follows.

6.1 Structure and Evaluation of Multilayer Films of Picene and DNTT on Their Bulklike Monolayers

Highly oriented multilayer molecular films of picene and DNTT molecules with the long axis parallel to the substrate were fabricated on their characteristic bulklike monolayer as shown in the diagram of Figure 6.1. These molecules form a dense monolayer with a bulklike molecular arrangement on metal surfaces such as Au(111), which allows further stacking of parallel molecules. Indeed, upon adsorption of picene and DNTT on these dense monolayers, growth of straight islands of multilayer without the dendritic layer was observed. Particularly, in the case of picene, one-dimensional islands with the lengths over 100 μm were formed and aligned in 3-fold symmetric directions of the substrate, which was not observed in the case of DNTT. X-ray diffraction measurements revealed the presence of [20$\bar{1}$] and [21$\bar{1}$] planes and the absence of the [001] diffractions, indicating that the one-dimensional islands of picene indeed consist of molecules in parallel configuration. The growth of the parallel molecules, which is particularly efficient for small molecules with enhanced intermolecular interaction such as phenacenes, will be beneficial not only for the applications in organic electronics devices but also in the basic research of the structure−function relationship of organic semiconductors.

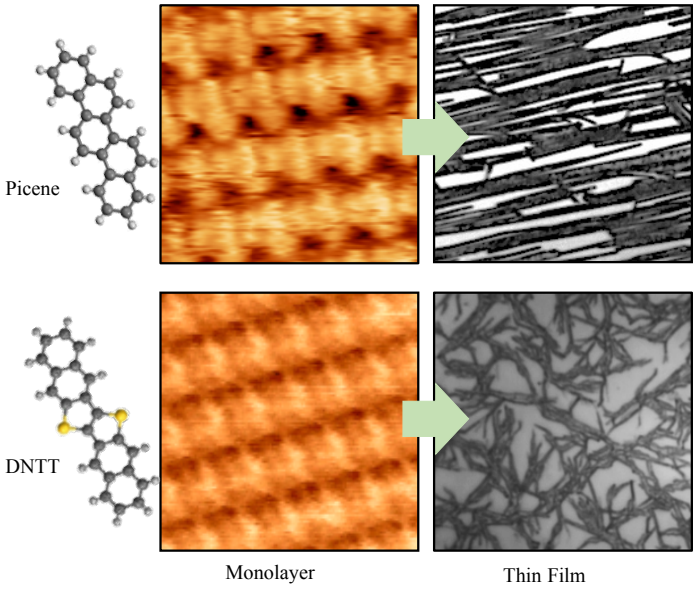

Figure 6.1 Diagram of thin film growth of picene and DNTT on their bulklike monolayer.

6.2 Structure and Evaluation of Sumanene Monolayers and Multilayer Films

In this study, we controlled the sumanene monolayer structure by changing the type of the substrate as shown in the STM images of Figure 6.2. The peculiar one-dimensional bowl-stacking sumanene monolayer was realized on the Cu(111) substrate. On Ag(111) and Au(111), sumanene monolayer shows a bowl-up and bowl-down arrangement, which form a periodic honeycomb structure. In this bowl-up and bowl-down configuration, the intermolecular interaction is weak, because the bowl inversion can easily occur during the STM measurement at room temperature. We also revealed the electronic structure of these two kinds of peculiar sumanene monolayers. Especially, the dispersion of HOMO band with a width of about 100 meV in the bowl-stacking direction of sumanene monolayer on Cu(111) was confirmed by ARPES measurement, indicating a stronger intermolecular interaction. Although sumanene multilayer films were tried to grow on these two peculiar monolayers in this work, no obvious island structure was observed by optical microscopy and AFM, which is different from the case of picene and DNTT thin films. Further X-ray diffraction measurements revealed the presence of (502) plane on the thin film on Cu(111), indicating the adsorption of tilted stacked sumanene molecules with respect to the surface which is similar with molecular arrangement in the monolayer. Whereas, XRD spectrum without any diffraction peak of sumanene thin film on Au(111) indicate an amorphous structure of sumanene thin film based on the monolayer with bowl-up and bowl-down molecular arrangement.

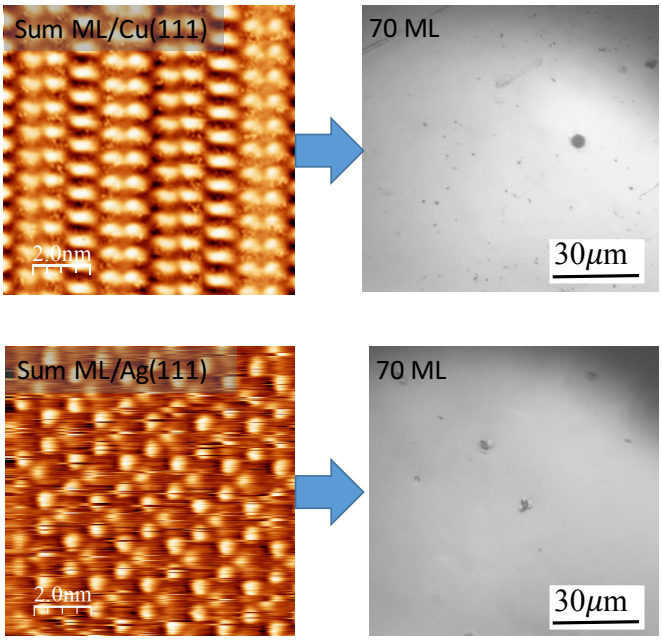

Figure 6.2 Diagram of thin films growth of sumanene on their monolayer on Cu(111) with bowl-stacking molecular arrangement and sumanene monolayer on Ag(111) with a mixture of bowl-up and bowl-down molecular arrangement.

6.3 Relationship Between Intermolecular Interaction and Morphology of Thin Film

The formation of huge crystalline islands in the case of picene, in contrast to the case of DNTT and sumanene, is possibly induced by the stronger intermolecular force. We estimated the force constant of the intermolecular van der Waals force of picene, DNTT, and sumanene along the stacking direction of two adjacent molecules using the potential energy curve, by simply assuming a harmonic oscillation at equilibrium. The results are listed in Table 6.1. Large force constant for both picene and DNTT bulk dimers show strong intermolecular interaction. Therefore, the bulk like monolayer of picene and DNTT are very promising for stacking the further moleculaes, causing the large crystalline islands structure of their thin films. Extremely large crystalline islands of picene thin film may be due to the relatively larger force constant, i.e. stronger intermolecular interactions between picene molecules. A large force constant for the sumanene dimer with the bowl-stacking structure of single crystal with the value of 34 kg/s^2, even larger than that of picene dimer, was observed. The large force constant of sumanene suggests that well-defined sumanene thin flim can be expected. Indeed, sumanene thin film with rod like structure on HMDS-treated glass substrates, which have a weak interaction with the mleuceles, has been reported. However, sumanene thin films show ultra thin thickness on Cu(111) and disordered structure on Au(111) even with large amount of deposition in this work. This phenomenon may be caused by the weak intermolecular interaction within the sumanene monolayers especially the monolayer with the bowl-up-down molecular arrangement, which can not stack the further molecules strongly. What's more, the bowl inversion of sumanene molecules during the deposition procedure is also speculated to influence the thin film growth. Since there are still many unknown factors, which can influence the thin film growth. To achieve a high quality sumanene thin film as indicated in this work, further research is surely required.

Table 6.1 Calculated results for picene, DNTT and sumanene dimers

	Picene	DNTT	Sumanene	
	Bulk dimer 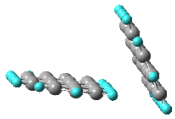	Bulk dimer 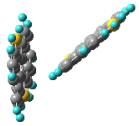	Single crystal dimer 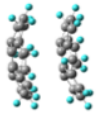	Bowl-up-down dimer 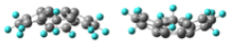
Force constant (kg/s^2)	26.27	21.64	34	9.1

In conclusion, this work further reinforces the understanding that the growth of organic thin films can be determined by the intermolecular interaction, which is critically important for fundamental research as well as technologically relevant applications.

References

(1) Muccini, M. A Bright Future for Organic Field-Effect Transistors. *Nat. Mater.* **2006**, *5* (8), 605–613. https://doi.org/10.1038/nmat1699.

(2) Forrest, S. R. The Path to Ubiquitous and Low-Cost Organic Electronic Appliances on Plastic. *Nature* **2004**, *428* (6986), 911–918. https://doi.org/10.1038/nature02498.

(3) Yang, X.; Li, Q.; Shuai, Z. Theoretical Modelling of Carrier Transports in Molecular Semiconductors: Molecular Design of Triphenylamine Dimer Systems. *Nanotechnology* **2007**, *18* (42), 424029. https://doi.org/10.1088/0957-4484/18/42/424029.

(4) Shen, Y.; Hosseini, A. R.; Wong, M. H.; Malliaras, G. G. How To Make Ohmic Contacts to Organic Semiconductors. *ChemPhysChem* **2004**, *5* (1), 16–25. https://doi.org/10.1002/cphc.200300942.

(5) Kim, S. H.; Jang, M.; Yang, H.; Park, C. E. Effect of Pentacene–dielectric Affinity on Pentacene Thin Film Growth Morphology in Organic Field-Effect Transistors. *J. Mater. Chem.* **2010**, *20* (27), 5612. https://doi.org/10.1039/b921371f.

(6) Käfer, D.; Ruppel, L.; Witte, G. Growth of Pentacene on Clean and Modified Gold Surfaces. *Phys. Rev. B* **2007**, *75* (8). https://doi.org/10.1103/PhysRevB.75.085309.

(7) Kankate, L.; Balzer, F.; Niehus, H.; Rubahn, H.-G. Organic Nanofibers from Thiophene Oligomers. *Thin Solid Films* **2009**, *518* (1), 130–137. https://doi.org/10.1016/j.tsf.2009.06.003.

(8) Simbrunner, C. Epitaxial Growth of Sexi-Thiophene and Para-Hexaphenyl and Its Implications for the Fabrication of Self-Assembled Lasing Nano-Fibres. *Semicond. Sci. Technol.* **2013**, *28* (5), 053001. https://doi.org/10.1088/0268-1242/28/5/053001.

(9) Simbrunner, C.; Nabok, D.; Hernandez-Sosa, G.; Oehzelt, M.; Djuric, T.; Resel, R.; Romaner, L.; Puschnig, P.; Ambrosch-Draxl, C.; Salzmann, I.; et al. Epitaxy of Rodlike Organic Molecules on Sheet Silicates—A Growth Model Based on Experiments and Simulations. *J. Am. Chem. Soc.* **2011**, *133* (9), 3056–3062. https://doi.org/10.1021/ja109729e.

(10) Jurchescu, O. D.; Baas, J.; Palstra, T. T. M. Effect of Impurities on the Mobility of Single Crystal Pentacene. *Appl. Phys. Lett.* **2004**, *84* (16), 3061–3063. https://doi.org/10.1063/1.1704874.

(11) Kalb, W. L.; Mattenberger, K.; Batlogg, B. Oxygen-Related Traps in Pentacene Thin Films: Energetic Position and Implications for Transistor Performance. *Phys. Rev. B* **2008**, *78* (3). https://doi.org/10.1103/PhysRevB.78.035334.

(12) Portella, G.; Poater, J.; Bofill, J. M.; Alemany, P.; Solà, M. Local Aromaticity of [*n*]Acenes, [*n*]Phenacenes, and [*n*]Helicenes (*n* = 1−9). *J. Org. Chem.* **2005**, *70* (7), 2509–2521. https://doi.org/10.1021/jo0480388.

(13) Okamoto, H.; Kawasaki, N.; Kaji, Y.; Kubozono, Y.; Fujiwara, A.; Yamaji, M. Air-Assisted High-Performance Field-Effect Transistor with Thin Films of Picene. *J. Am. Chem. Soc.* **2008**, *130* (32), 10470–10471. https://doi.org/10.1021/ja803291a.

(14) Sugawara, Y.; Ogawa, K.; Goto, H.; Oikawa, S.; Akaike, K.; Komura, N.; Eguchi, R.; Kaji, Y.; Gohda, S.; Kubozono, Y. O2-Exposure and Light-Irradiation Properties of Picene Thin Film Field-Effect Transistor: A New Way toward O2 Gas Sensor. *Sens. Actuators B Chem.* **2012**, *171–172*, 544–549. https://doi.org/10.1016/j.snb.2012.05.030.

(15) Yoshizawa, K.; Yahara, K.; Tanaka, K.; Yamabe, T. Bandgap Oscillation in Polyphenanthrenes. *J. Phys. Chem. B* **1998**, *102* (3), 498–506. https://doi.org/10.1021/jp972799f.

(16) Álvaro Galué, H.; Oomens, J.; Buma, W. J.; Redlich, B. Electron-Flux Infrared Response to Varying π-Bond Topology in Charged Aromatic Monomers. *Nat. Commun.* **2016**, *7* (1). https://doi.org/10.1038/ncomms12633.
(17) Mitsuhashi, R.; Suzuki, Y.; Yamanari, Y.; Mitamura, H.; Kambe, T.; Ikeda, N.; Okamoto, H.; Fujiwara, A.; Yamaji, M.; Kawasaki, N.; et al. Superconductivity in Alkali-Metal-Doped Picene. *Nature* **2010**, *464* (7285), 76–79. https://doi.org/10.1038/nature08859.
(18) Guijarro, A.; Vergés, J. A.; San-Fabián, E.; Chiappe, G.; Louis, E. Herringbone Pattern and CH-π Bonding in the Crystal Architecture of Linear Polycyclic Aromatic Hydrocarbons. *ChemPhysChem* **2016**, *17* (21), 3548–3557. https://doi.org/10.1002/cphc.201600586.
(19) Nguyen, T. P.; Shim, J. H.; Lee, J. Y. Density Functional Theory Studies of Hole Mobility in Picene and Pentacene Crystals. *J. Phys. Chem. C* **2015**, *119* (21), 11301–11310. https://doi.org/10.1021/jp511484d.
(20) Takimiya, K.; Shinamura, S.; Osaka, I.; Miyazaki, E. Thienoacene-Based Organic Semiconductors. *Adv. Mater.* **2011**, *23* (38), 4347–4370. https://doi.org/10.1002/adma.201102007.
(21) Haas, S.; Takahashi, Y.; Takimiya, K.; Hasegawa, T. High-Performance Dinaphtho-Thieno-Thiophene Single Crystal Field-Effect Transistors. *Appl. Phys. Lett.* **2009**, *95* (2), 022111. https://doi.org/10.1063/1.3183509.
(22) Uno, M.; Tominari, Y.; Yamagishi, M.; Doi, I.; Miyazaki, E.; Takimiya, K.; Takeya, J. Moderately Anisotropic Field-Effect Mobility in Dinaphtho[2,3-b:2′,3′-f]Thiopheno[3,2-b]Thiophenes Single-Crystal Transistors. *Appl. Phys. Lett.* **2009**, *94* (22), 223308. https://doi.org/10.1063/1.3153119.
(23) Sánchez-Carrera, R. S.; Atahan, S.; Schrier, J.; Aspuru-Guzik, A. Theoretical Characterization of the Air-Stable, High-Mobility Dinaphtho[2,3- *b* :2′3′- *f*]Thieno[3,2- *b*]-Thiophene Organic Semiconductor. *J. Phys. Chem. C* **2010**, *114* (5), 2334–2340. https://doi.org/10.1021/jp910102f.
(24) Amaya, T.; Hirao, T. A Molecular Bowl Sumanene. *Chem. Commun.* **2011**, *47* (38), 10524. https://doi.org/10.1039/c1cc12532j.
(25) Armaković, S.; Armaković, S. J.; Šetrajčić, J. P. Hydrogen Storage Properties of Sumanene. *Int. J. Hydrog. Energy* **2013**, *38* (27), 12190–12198. https://doi.org/10.1016/j.ijhydene.2013.05.091.
(26) Sakurai, H.; Daiko, T.; Sakane, H.; Amaya, T.; Hirao, T. Structural Elucidation of Sumanene and Generation of Its Benzylic Anions. *J. Am. Chem. Soc.* **2005**, *127* (33), 11580–11581. https://doi.org/10.1021/ja0518169.
(27) Amaya, T.; Seki, S.; Moriuchi, T.; Nakamoto, K.; Nakata, T.; Sakane, H.; Saeki, A.; Tagawa, S.; Hirao, T. Anisotropic Electron Transport Properties in Sumanene Crystal. *J. Am. Chem. Soc.* **2009**, *131* (2), 408–409. https://doi.org/10.1021/ja805997v.
(28) Frankevich, E.; Maruyama, Y.; Ogata, H. Mobility of Charge Carriers in Vapor-Phase Grown CeOsingle Crystal. *Chem. Phys. Lett.* **1993**, *214* (1), 6.
(29) Kojima, H.; Nakagawa, M.; Abe, R.; Fujiwara, F.; Yakiyama, Y.; Sakurai, H.; Nakamura, M. Thermoelectric and Thermal Transport Properties in Sumanene Crystals. *Chem. Lett.* **2018**, *47* (4), 524–527. https://doi.org/10.1246/cl.171210.
(30) Fisher, J. C.; Giaever, I. Tunneling Through Thin Insulating Layers. *J. Appl. Phys.* **1961**, *32* (2), 172–177. https://doi.org/10.1063/1.1735973.

(31) Schmidlin, F. W. Enhanced Tunneling through Dielectric Films Due to Ionic Defects. *J. Appl. Phys.* **1966**, *37* (7), 2823–2832. https://doi.org/10.1063/1.1782131.
(32) Simmons, J. G. Generalized Formula for the Electric Tunnel Effect between Similar Electrodes Separated by a Thin Insulating Film. *J. Appl. Phys.* **1963**, *34* (6), 1793–1803. https://doi.org/10.1063/1.1702682.
(33) Bardeen, J. Tunnelling from a Many-Particle Point of View. *Phys. Rev. Lett.* **1961**, *6* (2), 57–59. https://doi.org/10.1103/PhysRevLett.6.57.
(34) Tersoff, J.; Hamann, D. R. Theory and Application for the Scanning Tunneling Microscope. *Phys. Rev. Lett.* **1983**, *50* (25), 1998–2001. https://doi.org/10.1103/PhysRevLett.50.1998.
(35) Xin, Q.; Duhm, S.; Bussolotti, F.; Akaike, K.; Kubozono, Y.; Aoki, H.; Kosugi, T.; Kera, S.; Ueno, N. Accessing Surface Brillouin Zone and Band Structure of Picene Single Crystals. *Phys. Rev. Lett.* **2012**, *108* (22), 226401. https://doi.org/10.1103/PhysRevLett.108.226401.
(36) Yanagisawa, S.; Morikawa, Y.; Schindlmayr, A. Theoretical Investigation of the Band Structure of Picene Single Crystals within the GW Approximation. *Jpn. J. Appl. Phys.* **2014**, *53* (5S1), 05FY02. https://doi.org/10.7567/JJAP.53.05FY02.
(37) Kawai, N.; Eguchi, R.; Goto, H.; Akaike, K.; Kaji, Y.; Kambe, T.; Fujiwara, A.; Kubozono, Y. Characteristics of Single Crystal Field-Effect Transistors with a New Type of Aromatic Hydrocarbon, Picene. *J. Phys. Chem. C* **2012**, *116* (14), 7983–7988. https://doi.org/10.1021/jp300052p.
(38) Nguyen, T. P.; Shim, J. H.; Lee, J. Y. Density Functional Theory Studies of Hole Mobility in Picene and Pentacene Crystals. *J. Phys. Chem. C* **2015**, *119* (21), 11301–11310. https://doi.org/10.1021/jp511484d.
(39) Xie, W.; Willa, K.; Wu, Y.; Häusermann, R.; Takimiya, K.; Batlogg, B.; Frisbie, C. D. Temperature-Independent Transport in High-Mobility Dinaphtho-Thieno-Thiophene (DNTT) Single Crystal Transistors. *Adv. Mater.* **2013**, *25* (25), 3478–3484. https://doi.org/10.1002/adma.201300886.
(40) Diallo, A. K.; Kurihara, R.; Yoshimoto, N.; Videlot-Ackermann, C. Morphology and Microstructure of Picene Thin-Films for Air-Operating Transistors. *Appl. Surf. Sci.* **2014**, *314*, 704–710. https://doi.org/10.1016/j.apsusc.2014.07.085.
(41) Yamamoto, T.; Takimiya, K. Facile Synthesis of Highly π-Extended Heteroarenes, Dinaphtho[2,3- *b* :2‘,3‘- *f*]Chalcogenopheno[3,2- *b*]Chalcogenophenes, and Their Application to Field-Effect Transistors. *J. Am. Chem. Soc.* **2007**, *129* (8), 2224–2225. https://doi.org/10.1021/ja068429z.
(42) Ding, Z.; Abbas, G. A.; Assender, H. E.; Morrison, J. J.; Sanchez-Romaguera, V.; Yeates, S. G.; Taylor, D. M. Improving the Performance of Organic Thin Film Transistors Formed on a Vacuum Flash-Evaporated Acrylate Insulator. *Appl. Phys. Lett.* **2013**, *103* (23), 233301. https://doi.org/10.1063/1.4839275.
(43) Jariwala, D.; Howell, S. L.; Chen, K.-S.; Kang, J.; Sangwan, V. K.; Filippone, S. A.; Turrisi, R.; Marks, T. J.; Lauhon, L. J.; Hersam, M. C. Hybrid, Gate-Tunable, van Der Waals P–n Heterojunctions from Pentacene and MoS_2. *Nano Lett.* **2016**, *16* (1), 497–503. https://doi.org/10.1021/acs.nanolett.5b04141.
(44) Rockson, T. K.; Baek, S.; Jang, H.; Oh, S.; Choi, G.; Choi, H. H.; Lee, H. S. Macroscopic Interfacial Property as a Determining Parameter for Reliable Prediction of Charge Mobility in

Organic Transistors. *J. Phys. Chem. C* **2018**, *122* (31), 17695–17705. https://doi.org/10.1021/acs.jpcc.8b05959.
(45) Wang, Q.; Jiang, S.; Qiu, L.; Qian, J.; Ono, L. K.; Leyden, M. R.; Wang, X.; Shi, Y.; Zheng, Y.; Qi, Y.; et al. Interfacial Flat-Lying Molecular Monolayers for Performance Enhancement in Organic Field-Effect Transistors. *ACS Appl. Mater. Interfaces* **2018**, *10* (26), 22513–22519. https://doi.org/10.1021/acsami.8b07095.
(46) Gottardi, S.; Toccoli, T.; Iannotta, S.; Bettotti, P.; Cassinese, A.; Barra, M.; Ricciotti, L.; Kubozono, Y. Optimizing Picene Molecular Assembling by Supersonic Molecular Beam Deposition. *J. Phys. Chem. C* **2012**, *116* (46), 24503–24511. https://doi.org/10.1021/jp304561s.
(47) Hasegawa, Y.; Yamada, Y.; Hosokai, T.; Koswattage, K. R.; Yano, M.; Wakayama, Y.; Sasaki, M. Overlapping of Frontier Orbitals in Well-Defined Dinaphtho[2,3-b:2′,3′-f]Thieno[3,2- *b*]-Thiophene and Picene Monolayers. *J. Phys. Chem. C* **2016**, *120* (38), 21536–21542. https://doi.org/10.1021/acs.jpcc.6b06838.
(48) Chen, S.-W.; Sang, I.-C.; Okamoto, H.; Hoffmann, G. Adsorption of Phenacenes on a Metallic Substrate: Revisited. *J. Phys. Chem. C* **2017**, *121* (21), 11390–11398. https://doi.org/10.1021/acs.jpcc.7b01806.
(49) Hanke, F.; Björk, J. Structure and Local Reactivity of the Au(111) Surface Reconstruction. *Phys. Rev. B* **2013**, *87* (23). https://doi.org/10.1103/PhysRevB.87.235422.
(50) Barth, J. V.; Brune, H.; Ertl, G.; Behm, R. J. Scanning Tunneling Microscopy Observations on the Reconstructed Au(111) Surface: Atomic Structure, Long-Range Superstructure, Rotational Domains, and Surface Defects. *Phys. Rev. B* **1990**, *42* (15), 9307–9318. https://doi.org/10.1103/PhysRevB.42.9307.
(51) Hanke, F.; Björk, J. Structure and Local Reactivity of the Au(111) Surface Reconstruction. *Phys. Rev. B* **2013**, *87* (23). https://doi.org/10.1103/PhysRevB.87.235422.
(52) Halgren, T. A. Merck Molecular Force Field. I. Basis, Form, Scope, Parameterization, and Performance of MMFF94. *J. Comput. Chem.* **1996**, *17* (5–6), 490–519. https://doi.org/10.1002/(SICI)1096-987X(199604)17:5/6<490::AID-JCC1>3.0.CO;2-P.
(53) Kelly, S. J.; Sorescu, D. C.; Wang, J.; Archer, K. A.; Jordan, K. D.; Maksymovych, P. Structural and Electronic Properties of Ultrathin Picene Films on the Ag(100) Surface. *Surf. Sci.* **2016**, *652*, 67–75. https://doi.org/10.1016/j.susc.2016.02.007.
(54) Yoshida, Y.; Yang, H.-H.; Huang, H.-S.; Guan, S.-Y.; Yanagisawa, S.; Yokosuka, T.; Lin, M.-T.; Su, W.-B.; Chang, C.-S.; Hoffmann, G.; et al. Scanning Tunneling Microscopy/Spectroscopy of Picene Thin Films Formed on Ag(111). *J. Chem. Phys.* **2014**, *141* (11), 114701. https://doi.org/10.1063/1.4894439.
(55) Yano, M.; Okada, R.; Endo, M.; Shimizu, R.; Hasegawa, Y.; Yamada, Y.; Sasaki, M. Microscopic Structure of K-Doped Organic Monolayers. *E-J. Surf. Sci. Nanotechnol.* **2014**, *12* (0), 330–333. https://doi.org/10.1380/ejssnt.2014.330.
(56) Wang, Q.; Xin, Q.; Wang, R.-B.; Oehzelt, M.; Ueno, N.; Kera, S.; Duhm, S. Picene Thin Films on Metal Surfaces: Impact of Molecular Shape on Interfacial Coupling: Picene Thin Films on Metal Surfaces. *Phys. Status Solidi RRL - Rapid Res. Lett.* **2017**, *11* (5), 1700012. https://doi.org/10.1002/pssr.201700012.

(57) Chung, H.; Diao, Y. Polymorphism as an Emerging Design Strategy for High Performance Organic Electronics. *J. Mater. Chem. C* **2016**, *4* (18), 3915–3933. https://doi.org/10.1039/C5TC04390E.
(58) Dreher, M.; Bischof, D.; Widdascheck, F.; Huttner, A.; Breuer, T.; Witte, G. Interface Structure and Evolution of Dinaphthothienothiophene (DNTT) Films on Noble Metal Substrates. *Adv. Mater. Interfaces* **2018**, 1800920. https://doi.org/10.1002/admi.201800920.
(59) Müllegger, S.; Salzmann, I.; Resel, R.; Hlawacek, G.; Teichert, C.; Winkler, A. Growth Kinetics, Structure, and Morphology of Para-Quaterphenyl Thin Films on Gold(111). *J. Chem. Phys.* **2004**, *121* (5), 2272–2277. https://doi.org/10.1063/1.1767154.
(60) Wu, Y.-T.; Siegel, J. S. Aromatic Molecular-Bowl Hydrocarbons: Synthetic Derivatives, Their Structures, and Physical Properties. *Chem. Rev.* **2006**, *106* (12), 4843–4867. https://doi.org/10.1021/cr050554q.
(61) Bauert, T.; Baldridge, K. K.; Siegel, J. S.; Ernst, K.-H. Surface-Assisted Bowl-in-Bowl Stacking of Nonplanar Aromatic Hydrocarbons. *Chem. Commun.* **2011**, *47* (28), 7995. https://doi.org/10.1039/c1cc12540k.
(62) Xiao, W.; Passerone, D.; Ruffieux, P.; Aït−Mansour, K.; Gröning, O.; Tosatti, E.; Siegel, J. S.; Fasel, R. C_{60} /Corannulene on Cu(110): A Surface-Supported Bistable Buckybowl−Buckyball Host−Guest System. *J. Am. Chem. Soc.* **2008**, *130* (14), 4767–4771. https://doi.org/10.1021/ja077816l.
(63) Baby, A.; Lin, H.; Ravikumar, A.; Bittencourt, C.; Wegner, H. A.; Floreano, L.; Goldoni, A.; Fratesi, G. Lattice Mismatch Drives Spatial Modulation of Corannulene Tilt on Ag(111). *J. Phys. Chem. C* **2018**, *122* (19), 10365–10376. https://doi.org/10.1021/acs.jpcc.7b11581.
(64) Merz, L.; Parschau, M.; Zoppi, L.; Baldridge, K. K.; Siegel, J. S.; Ernst, K.-H. Reversible Phase Transitions in a Buckybowl Monolayer. *Angew. Chem. Int. Ed.* **2009**, *48* (11), 1966–1969. https://doi.org/10.1002/anie.200804563.
(65) Bauert, T.; Merz, L.; Bandera, D.; Parschau, M.; Siegel, J. S.; Ernst, K.-H. Building 2D Crystals from 5-Fold-Symmetric Molecules. *J. Am. Chem. Soc.* **2009**, *131* (10), 3460–3461. https://doi.org/10.1021/ja8101083.
(66) Parschau, M.; Fasel, R.; Ernst, K.-H.; Gröning, O.; Brandenberger, L.; Schillinger, R.; Greber, T.; Seitsonen, A. P.; Wu, Y.-T.; Siegel, J. S. Buckybowls on Metal Surfaces: Symmetry Mismatch and Enantiomorphism of Corannulene on Cu(110). *Angew. Chem. Int. Ed.* **2007**, *46* (43), 8258–8261. https://doi.org/10.1002/anie.200700610.
(67) Zoppi, L.; Bauert, T.; Siegel, J. S.; Baldridge, K. K.; Ernst, K.-H. Pentagonal Tiling with Buckybowls: Pentamethylcorannulene on Cu(111). *Phys. Chem. Chem. Phys.* **2012**, *14* (38), 13365. https://doi.org/10.1039/c2cp41732d.
(68) Sakurai, H.; Daiko, T.; Hirao, T. A Synthesis of Sumanene, a Fullerene Fragment. *Sci. New Ser.* **2003**, *301* (5641), 1878.
(69) Saito, M.; Shinokubo, H.; Sakurai, H. Figuration of Bowl-Shaped π-Conjugated Molecules: Properties and Functions. *Mater. Chem. Front.* **2018**, *2* (4), 635–661. https://doi.org/10.1039/C7QM00593H.
(70) Chen, X.; Wang, H.; Wang, B.; Wang, Y.; Jin, X.; Bai, F.-Q. Charge Transport Properties in Organic D-A Mixed-Stack Complexes Based on Corannulene and Sumanene Derivatives-a Theoretical Study. *Org. Electron.* **2019**, *68*, 35–44. https://doi.org/10.1016/j.orgel.2019.01.034.

(71) Armaković, S.; Armaković, S. J.; Šetrajčić, J. P.; Jaćimovski, S. K.; Holodkov, V. Sumanene and Its Adsorption Properties towards CO, CO2 and NH3 Molecules. *J. Mol. Model.* **2014**, *20* (4). https://doi.org/10.1007/s00894-014-2170-3.
(72) Della, T. D.; Suresh, C. H. Sumanene: An Efficient π-Bowl for Dihydrogen Storage. *Phys. Chem. Chem. Phys.* **2018**, *20* (9), 6227–6235. https://doi.org/10.1039/C7CP07000D.
(73) Jaafar, R.; Pignedoli, C. A.; Bussi, G.; Aït-Mansour, K.; Groening, O.; Amaya, T.; Hirao, T.; Fasel, R.; Ruffieux, P. Bowl Inversion of Surface-Adsorbed Sumanene. *J. Am. Chem. Soc.* **2014**, *136* (39), 13666–13671. https://doi.org/10.1021/ja504126z.
(74) Fujii, S.; Ziatdinov, M.; Higashibayashi, S.; Sakurai, H.; Kiguchi, M. Bowl Inversion and Electronic Switching of Buckybowls on Gold. *J. Am. Chem. Soc.* **2016**, *138* (37), 12142–12149. https://doi.org/10.1021/jacs.6b04741.
(75) Stöckl, Q. S.; Hsieh, Y.-C.; Mairena, A.; Wu, Y.-T.; Ernst, K.-H. Aggregation of C_{70} -Fragment Buckybowls on Surfaces: Π–H and Π–π Bonding in Bowl Up-Side-Down Ensembles. *J. Am. Chem. Soc.* **2016**, *138* (19), 6111–6114. https://doi.org/10.1021/jacs.6b02412.
(76) Ziatdinov, M.; Maksov, A.; Kalinin, S. V. Learning Surface Molecular Structures via Machine Vision. *Npj Comput. Mater.* **2017**, *3* (1). https://doi.org/10.1038/s41524-017-0038-7.
(77) Heimel, G.; Duhm, S.; Salzmann, I.; Gerlach, A.; Strozecka, A.; Niederhausen, J.; Bürker, C.; Hosokai, T.; Fernandez-Torrente, I.; Schulze, G.; et al. Charged and Metallic Molecular Monolayers through Surface-Induced Aromatic Stabilization. *Nat. Chem.* **2013**, *5* (3), 187–194. https://doi.org/10.1038/nchem.1572.
(78) Seah, M. P.; Dench, W. A. Quantitative Electron Spectroscopy of Surfaces: A Standard Data Base for Electron Inelastic Mean Free Paths in Solids. *Surf. Interface Anal.* **1979**, *1* (1), 2–11. https://doi.org/10.1002/sia.740010103.
(79) Yano, M.; Endo, M.; Hasegawa, Y.; Okada, R.; Yamada, Y.; Sasaki, M. Well-Ordered Monolayers of Alkali-Doped Coronene and Picene: Molecular Arrangements and Electronic Structures. *J. Chem. Phys.* **2014**, *141* (3), 034708. https://doi.org/10.1063/1.4887776.

List of Publications and Presentations

A) Publications

1. Chunyang Zhang, Hiromu Tsuboi, Yuri Hasegawa, Masato Iwasawa, Masahiro Sasaki, Yutaka Wakayama, Hiroyuki Ishii, Yoichi Yamada

Fabrication of Highly Oriented Multilayer Films of Flat-lying Picene and DNTT on Their Bulk-like Monolayer

ACS Omega, 2019,4, 8669-8673

2. Yoichi Yamada, Artem V. Kuklin, Sho Sato, Fumitaka Esaka, Naoto Sumi, Chunyang Zhang, Masahiro Sasaki, Eunsung Kwon, Yukihiko Kasama, Pavel V. Avramov, Seiji Sakai

Electronic structure of $Li^+@C_{60}$: Photoelectron spectroscopy of the $Li^+@C_{60}[PF_6^-]$ salt and STM of the single $Li^+@C_{60}$ molecules on Cu(111)

Carbon, 133 (2018) 23-30

3. K. Ohno, A. Manjanath, Y. Kawazoe, R. Hatakeyama, F. Misaizu, E. Kwon, H. Fukumura, H. Ogasawara, Y. Yamada, C. Zhang, N. Sumi, T. Kamigaki, K. Kawachi, K. Yokoo, S. Ono and Y. Kasamai

Extensive first-principles molecular dynamics study on Li encapsulation into C60 and its experimental confirmation

Nanoscale, 2018, 10, 1825–1836

2. Chunyang Zhang, Takuro Maeda, Yuri Hasegawa, Masahiro Sasaki, Yoichi Yamada

One-dimensional bowl-stacking surface-adsorbed sumanene on Cu(111)

In preparation

B) Presentations

1. Chunyang Zhang, Yuri Hasegawa, Yutaka Wakayama, Yoichi Yamada, Masahiro Sasaki

Fabrication of Highly Oriented Molecule Films Utilizing Well-ordered Monolayer as Template

The 8th International Symposium on Surface Science (ISSS-8), October 22-26, 2017, Tsukuba, Japan

2. C. Zhang, A. V. Kuklin, F. Esaka, N. Sumi, M. Sasaki, E. Kwon, Y. Kasama, P. V. Avramov, S. Sakai and Y. Yamada

Photoelectron spectroscopy of the $Li^+@C_{60}[PF_6^-]$ saltand STM of the single $Li^+@C_{60}$ molecules on Cu(111)

The 79th Autumn Meeting, 2018, The Japan Society of Applied Physics and Related Societies, Nagoya, Japan, September 2018

3. Chunyang Zhang, Naoya Sumi, Takuro Maeda, Masahiro Sasaki, Yoichi Yamada

π-stacking Sumanene Monolayer on Cu(111) and K-doping

The 79th Autumn Meeting, 2018, The Japan Society of Applied Physics and Related Societies, Nagoya, Japan, September 2018

4. C. Zhang, A. V. Kuklin, F. Esaka, N. Sumi, M. Sasaki, E. Kwon, Y. Kasama, P. V. Avramov, S. Sakai and Y. Yamada

Photoelectron spectroscopy of the $Li^+@C_{60}[PF_6^-]$ saltand STM of the single $Li^+@C_{60}$ molecules on Cu(111)

ACSIN-14 & ICSPM26, Sendai, Japan, October 21-25, 2018

5. Chunyang Zhang, Naoya Sumi, Masahiro Sasaki, Yoichi Yamada

Core levels and frontier orbitals of K-doped sumanene monolayer

The first international workshop on Momentum Microscopy & Spectroscopy for Materials Science, Okazaki Conference Center, Japan, 22nd-23rd February, 2019

6. Chunyang Zhang, Naoya Sumi, Masahiro Sasaki, Yoichi Yamada

Core levels and frontier orbitals of K-doped sumanene monolayer

The 66th Spring Meeting, 2018, The Japan Society of Applied Physics and Related Societies, Tokyo, Japan, March 2019

Acknowledgements

This research has been undertaken at the Sasaki-Yamada Laboratory, Institute of Applied Physics, University of Tsukuba (Tsukuba, Japan). I would like to acknowledge a lot of nice people I was lucky to work with during my Ph.D. studies.

I would like to thank my supervisors, Prof. Masahiro Sasaki and Prof. Yamada of Institute of Applied Physics, University of Tsukuba, for their continued support and encouragement over three years during my study in Japan. I learned not only surface science but also a more prudent approach for research from them. Prof. Masahiro Sasaki and Prof. Yamada are not only excellent researchers and very patient supervisors. Specially thanks to Prof. Yamada, because he provided many opportunities for discussion and experimental chance with other groups in other institute. I had a lot of great time and learned a lot in and outside the lab because of him.

I would also like to express my gratitude to Prof. Wakayama of NIMS and Prof. Kobayashi of University of Tsukuba for their kindness to be my degree committee.

I would like to thank all the past and current members of the Sasaki-Yamada Lab. All of you are so kindly and friendly. I am very happy to gain your friendship during my study. Especially thanks to Yuri Hasegawa, she is also a good senior for my research and life in Japan. Specially thanks to Naoya Sumi, my most important experiment partner, and Masato Iwasawa, my tutor in the first year I arrived in Japan. Thank you two very much for taking me to eat so many delicious foods in Tsukuba :). Also specially thanks to kindly Mrs. Matsui Akiko of Saslaki-Yamada lab. Thank you for giving me so many delicious food during the three years and special handmade cake for my gruaduation defense.

I am also very grateful to all my Chinese friends in Tsukuba, especially Ting Mei, Dejun Liu, Kailong Hu, Xiaolong Zhang, for their company during the three years in Japan. Thank you for sharing your great experiences with me all the time. And thank you for traveling with me so many times and enjoy the beautiful Japan together :).

Many great thanks to my family, my dear parents and my dear sister, for supporting me all the time and being patient with me. Very many great thanks to my boyfriend Mr. Liu for waiting for me and so many patients for me a lot of things, especially during the final stage of my graduation :).

Finally, I would like to acknowledge the financial support from the China Scholarship Council for the scholarship under the Chinese Government Graduate Student Overseas Study Scholarship Program.